

Doctoral Dissertation (Censored)

博士論文 (要約)

On-chip group IV photonic devices for vibrational spectroscopy

(振動分光のための第 IV 族オンチップ光学デバイス)

A Dissertation Submitted for the Degree of Doctor of Philosophy
July 2019

令和元年 7 月博士(理学)申請
Department of Chemistry, Graduate School of Science,
The University of Tokyo

東京大学大学院理学系研究科化学専攻

XIAO, Tinghui

肖 廷辉

On-chip group IV photonic devices for vibrational spectroscopy

by

XIAO, Tinghui

Submitted to the Department of Chemistry
in partial fulfillment of the requirements for the degree of
Doctor of Philosophy
at
The University of Tokyo

Abstract

Vibrational spectroscopy, including infrared spectroscopy and Raman spectroscopy, is a powerful optical technique to non-invasively probe vibrational signatures of molecules and, thereby, enables analysis of composite systems of physical, chemical, and biological interests due to its inherent selectivity. By virtue of its versatility for studying solid, liquid, and gas samples, vibrational spectroscopy has been used for a variety of intriguing applications, such as chemical detection, disease diagnosis, environmental monitoring, and industrial process control. Unfortunately, most of these applications still remain confined to the laboratory environment. This is partially due to the bulky and costly instrumentation of vibrational spectroscopy with moderate sensitivity.

Realization of on-chip photonic devices provides a promising solution to the above problem owing to its advantages of low cost, high compactness, and high reliability. Various integration platforms of on-chip photonic devices have been developed, involving a wide range of optical materials that include noble metals, two-dimensional materials, chalcogenide glasses, and group IV semiconductors (carbon, silicon and germanium). Among them, group IV semiconductors provide mature and low-loss material platforms for integration owing to their CMOS-compatible fabrication conditions and all-dielectric environment. However, due to the limited quality and structural designs of traditional photonic devices, realization of on-chip group IV photonic devices for vibrational spectroscopy still remains challenging.

In this doctoral work, I proposed and experimentally demonstrated several on-chip group IV photonic devices with controllable strong light-matter interaction for low-cost, highly sensitive vibrational spectroscopy. Specifically, I developed on-chip germanium photonic devices with high quality (Q) factors for infrared spectroscopy, on-chip silicon photonic devices with tailored resonant nanostructures for Raman spectroscopy, and an on-chip carbon photonic device with strong chemical enhancement for Raman spectroscopy. For the on-chip germanium photonic devices, I experimentally demonstrated a hexagonal-lattice zero-cell photonic crystal cavity, a photonic crystal nanobeam cavity, and a microring resonator. For the on-chip silicon photonic devices, I experimentally

demonstrated a spiral nanoflower and a nanodisk array. For the on-chip carbon photonic device, I experimentally demonstrated a porous carbon nanowire array (PCNA). The developed photonic devices enable low-cost and highly-sensitive vibrational spectroscopy, which is expected to find diverse applications in analytical chemistry, pharmaceutical science, environmental safety, and pathology.

Thesis Supervisor: Keisuke Goda

Title: Professor of Chemistry

Acknowledgements

Time flies! I can still clearly remember the first day when I came to Yasuda Auditorium to attend the entrance ceremony as a new Ph.D. student. Now I have stepped into the last period of my Ph.D. study. Reviewing these three years, I feel so lucky that I could meet so many excellent and nice people who always encouraged and supported me to accomplish my Ph.D. study. Here I want to take this opportunity to express my deepest gratitude and appreciation to all of them that make this thesis possible.

First and foremost, I want to thank my supervisor Prof. Keisuke Goda. I am grateful to him for accepting me as his Ph.D. student and providing an excellent environment for my research. He taught me not only how to make great research, but also how to become an excellent professor in the future. He provided a lot of challenging opportunities for me, which made my Ph.D. study stimulating and productive. His incisive understanding on science always expands my scientific vision and stimulates me to step forward in my research. I can never succeed in my Ph.D. research without his careful and attentive instruction and supervision. All I have learned from him in these years will be precious assets for my future academic career.

Second of all, I want to thank my team leader Prof. Zhenzhou Cheng. He was always trying to create the best experimental conditions for me and was always willing to help me when I met all kinds of problems. I can never forget the precious experience that we started our new research directions from nothing. We went to Takeda cleanroom together to accumulate fabrication experience and tune fabrication recipes. We applied for research grants and built up our experimental setups. We stayed up to write papers until midnights. His optimism and encouragement helped me pass through a lot of tough time in my Ph.D. pursuit. Without his strong support, I may never go so far. I feel so lucky that I can be his student and team member.

I also want to thank all other Goda Lab members for their various support. I would like to thank Prof. Hideharu Mikami, Prof. Kotaro Hiramatsu, and Prof. Cheng Lei for their practical and useful suggestions for my research. I would like to thank Prof. Akihiro Isozaki for his kindness to help me with my Japanese and treat me as a friend. I would like to thank Tadataka Ota for his help with the electric circuits in my optical setups. I would

like to thank Dr. Hirofumi Kobayashi, Zhenyi Luo, Kangrui Huang, Yunzhao Wu, Yuqi Zhou, Ruyue Zhang, Angelina Frank, and Matthew Lindley for assisting my experiments and organizing parties and activities to enrich my life in Japan.

I also want to express my appreciation to my great collaborators, Prof. Sze Yun Set, Prof. Mitsuru Takenaka, Prof. Hon Ki Tsang, Prof. Masahiro Nomura, Prof. Satoshi Iwamoto, Prof. Tamitake Itoh, Prof. Nan Chen, Dr. Yasutaka Kitahama, Dr. Wen Zhou, and Ziqiang Zhao, for providing knowledge, resources, and assistance for my research. Their contributions effectively accelerated my research.

I also want to thank my family for their love, encouragement, and support. I want to thank my parents for respecting and supporting my interest and pursuit in scientific research. Their unconditional support gave me the power and courage to face and conquer all the difficulties in my Ph.D. study. I want to appreciate my loving, considerate, and encouraging girlfriend Miss Yan Li for her understanding and faithful support all the time.

At last, I want to thank MEXT scholarship for financially supporting my Ph.D. study in Japan. My Ph.D. research was also funded by JSPS KAKENHI (JP18K13798), University of Tokyo GAP Fund, JSPS Core-to-Core Program, and White Rock Foundation.

Contents

Abstract	1
Acknowledgements	3
Contents	5
List of Figures	8
List of Tables	17
1 Introduction	18
1.1 Vibrational spectroscopy	18
1.2 On-chip photonic devices	20
1.3 Group IV optical materials	23
1.4 Scope and structure of this thesis	25
2 Principles of on-chip photonic devices for vibrational spectroscopy.....	27
2.1 Overview	27
2.2 Theory of highly sensitive vibrational spectroscopy	27
2.3 Design of on-chip photonic devices	31
2.4 Fabrication of on-chip photonic devices	32
2.5 Characterization of on-chip photonic devices	33
3 Demonstration of on-chip germanium photonic devices for infrared spectroscopy	36
3.1 Introduction	36
3.2 Suspended-membrane integration platform	37
3.2.1 Theoretical design	37
3.2.2 Experimental fabrication	38
3.3 Hexagonal-lattice zero-cell photonic crystal cavity	39
3.3.1 Overview	39
3.3.2 Theoretical design	40
3.3.3 Experimental fabrication	45
3.3.4 Experimental characterization	45

3.3.5	Summary.....	46
3.4	High-Q photonic crystal nanobeam cavity	47
3.4.1	Overview	47
3.4.2	Theoretical design	47
3.4.3	Experimental fabrication	49
3.4.4	Experimental characterization	51
3.4.5	Summary.....	52
3.5	High-Q microring resonator	53
3.5.1	Overview	53
3.5.2	Theoretical design	53
3.5.3	Experimental fabrication	55
3.5.4	Experimental characterization	57
3.5.5	Summary.....	58
3.6	Conclusion.....	58
4	Demonstration of on-chip silicon photonic devices for Raman spectroscopy....	60
4.1	Introduction	60
4.2	Spiral nanoflower with giant optical activity	60
4.2.1	Introduction	60
4.2.2	Theoretical design	62
4.2.3	Experimental fabrication	74
4.2.4	Experimental characterization	75
4.2.5	Summary.....	78
4.3	Nanodisk array for enhanced Raman optical activity.....	79
4.3.1	Introduction	79
4.3.2	Theoretical design	81
4.3.3	Experimental fabrication	88
4.3.4	Experimental characterization	89
4.3.5	Summary.....	98
4.4	Conclusion.....	99
5	Demonstration of on-chip carbon photonic devices for Raman spectroscopy.	100

5.1	Introduction	100
5.2	Porous carbon nanowire array for enhanced Raman spectroscopy	101
5.2.1	Experimental fabrication	101
5.2.2	Experimental characterization	103
5.2.3	Theoretical interpretation	111
5.3	Conclusion.....	113
6	Summary and outlook.....	114
	Table of Acronyms	118
	Publications	120
	Bibliography.....	121

List of Figures

Figure 1-1. Energy diagram of four types of light-molecule interaction, including infrared absorption, Rayleigh scattering, Stokes Raman scattering, and Anti-stokes Raman scattering.	19
Figure 1-2. Miniaturization of traditional vibrational spectroscopy instruments by utilizing on-chip photonic devices.	21
Figure 1-3. Working flow for realizing on-chip photonic devices for vibrational spectroscopic applications.	22
Figure 1-4. Transparency windows of CMOS-compatible group IV optical materials in integrated photonics.....	23
Figure 2-1. FEM simulations. (a) Meshes of an on-chip photonic device. (b) Electric field magnitude distribution of an on-chip photonic device.	32
Figure 2-2. Fabrication equipment. (a) Electron-beam writer: EB Advantest F7000S in Takeda Cleanroom at the University of Tokyo. (b) Inductively coupled plasma etcher: ICP-RIE Ulvac CE-300I in Takeda Cleanroom at the University of Tokyo.....	33
Figure 2-3. Fiber-coupled optical setup for the characterization of on-chip germanium photonic devices for infrared spectroscopy.	34
Figure 2-4. Objective lens-coupled optical setup for the characterization of on-chip silicon/carbon photonic devices for Raman spectroscopy.....	35
Figure 3-1. Schematic diagram of the germanium suspended-membrane integration platform.	37
Figure 3-2. Fabrication process of the GOI wafer and the infrared suspended-membrane germanium photonic device.	38
Figure 3-3. Cross-section of the germanium suspended-membrane integration platform.	39
Figure 3-4. Schematic of the monolithically integrated on-chip MIR germanium device that contains a photonic crystal cavity, two photonic crystal waveguides, two cantilever waveguides, two suspended membrane waveguides, and two focusing subwavelength grating couplers. (a) Three-dimensional view of the	

- device. (b) Top view of the photonic crystal cavity and waveguides. (c) Cross-sectional view of the suspended membrane waveguide. 40
- Figure 3-5. Design of the photonic crystal cavity. (a) Transmission spectrum and electric-field magnitude distributions in the cavity without a coupling of the two cavity modes. (b) Transmission spectrum and electric-field magnitude distributions in the cavity with a coupling of the two cavity modes (Fano resonance). ... 43
- Figure 3-6. SEM images of the monolithically integrated on-chip IR germanium device. (a) Top view of the device. Scale bar: 5 μm . (b) Top view of the photonic crystal cavity and waveguides. Scale bar: 1 μm 44
- Figure 3-7. Measured transmission spectrum of the monolithically integrated on-chip IR germanium device (blue) and measured coupling efficiency of the focusing subwavelength grating couplers and suspended waveguide (red). 46
- Figure 3-8. Schematic of the monolithically integrated on-chip mid-IR germanium device that contains a high-Q nanocavity, two suspended membrane waveguides, and two focusing subwavelength grating couplers. The bottom left inset shows the design of the high-Q nanocavity. The bottom right inset shows a cross-sectional view of the suspended membrane waveguide. 48
- Figure 3-9. SEM images of the mid-IR germanium device, including the high-Q nanocavity. (a) Top view of the device. Scale bar: 10 μm . (b) Top view of the high-Q nanocavity. Scale bar: 500 nm. 49
- Figure 3-10. Experimental characterization of the mid-IR germanium device, including the high-Q nanocavity. (a) Measured transmission spectrum of the device (blue) and measured coupling efficiency of the focusing subwavelength grating couplers (red). (b) Lorentzian fitting of the measured nanocavity resonant mode. The inset is the electric field magnitude distribution of the resonant mode. 50
- Figure 3-11. Schematic of the monolithically integrated on-chip mid-IR germanium device that contains a high-Q microring resonator, a suspended-membrane waveguide, and two focusing grating couplers. (a) Three-dimensional view of the device. (b) Coupling area between the microring resonator and waveguide. (c) Cross-sectional view of the suspended-membrane waveguide. 54

Figure 3-12. SEM images of the mid-IR germanium device, including the high-Q microring resonator. (a) Top view of the device. Scale bar: 20 μm . (b) Coupling area between the high-Q microring resonator and the waveguide. Scale bar: 1 μm . (c) Zoom-in view of the coupling area which indicates the sidewalls of the fabricated high-Q microring resonator and the waveguide are smooth. Scale bar: 200 nm. 55

Figure 3-13. Characterization of the MIR germanium device, including the high-Q microring resonator. (a) Measured free spectral range of the microring resonator. (b) Distribution of the electric field magnitude $|E|$ of the microring resonator's quasi-TE mode. (c) ER of the microring resonator. (b) Q factor of the microring resonator. 56

Figure 3-14. Comparison of recently reported germanium resonators. The mid-IR germanium resonator with the highest Q factor and the mid-IR germanium nanocavity with the highest Q factor were demonstrated in my doctoral work. 59

Figure 4-1. Concept of giant optical activity in an all-dielectric spiral nanoflower. A beam of left or right circularly polarized (LCP or RCP) light normally impinges on a nanoflower on a silica substrate. Scattered light, which reflects the interaction between the incident light and the nanoflower, is gleaned to quantify the optical activity of the nanoflower. The inset shows the geometric parameters of the nanoflower. $a = 425\text{ nm}$, $b = 125\text{ nm}$, $r = 187\text{ nm}$, $d = 250\text{ nm}$, and $h = 340\text{ nm}$ 63

Figure 4-2. Theoretical analysis of the optical activity of the nanoflower. (a) Scattering cross-section of the nanoflower. (b) Circular intensity difference (CID) of the nanoflower. (c) Normalized magnetic near-field strength of the incident LCP and RCP light at the wavelength where the CID is peaked. (d) Normalized electric near-field strength of the incident LCP and RCP light at the wavelength where the CID is peaked. 64

Figure 4-3. Three-dimensional field distributions of the nanoflower. (a) Normalized magnetic near-field strength. (b) Normalized electric near-field strength. .. 66

Figure 4-4. Theoretical analysis of the optical activity of the nanoflower. (a) Scattering cross-section of the nanoflower. (b) Circular intensity difference (CID) of the nanoflower. (c) Normalized magnetic near-field strength of the incident LCP and RCP light at the wavelength where the CID is peaked. (d) Normalized electric near-field strength of the incident LCP and RCP light at the wavelength where the CID is peaked.	68
Figure 4-5. Distributions of the magnetic field component H_z excited by the incident LCP and RCP light.....	69
Figure 4-6. Theoretical analysis of the absorption of the nanoflower. (a) Absorption cross-section of the nanoflower. (b) Normalized circular dichroism of the nanoflower.	70
Figure 4-7. Theoretical analysis of the non-diagonal elements the nanoflower's Jones Matrix. (a) Real and imaginary parts of rx_{xy} . (b) Real and imaginary parts of ryx	71
Figure 4-8. Theoretical analysis of the interference between the central nanocylinder and the surrounding nanocylinders. (a) Scattering spectra and CID of the nanoflower without the central nanocylinder. (b) Normalized scattering spectra of the nanoflowers with or without the central nanocylinder.....	72
Figure 4-9. Electric and magnetic quadrupole contributions to the scattering cross section of the nanoflower without the central nanocylinder for the incident LCP light.	72
Figure 4-10. Field distributions of the central nanocylinder and the nanoflower without the central nanocylinder. (a) Normalized magnetic near-field strength. (b) Normalized electric near-field strength.	73
Figure 4-11. Fabrication steps of the nanoflower.	74
Figure 4-12. Scanning electron microscope images of the fabricated all-dielectric spiral nanoflowers. (a) Array of the nanoflowers. Scale bar = 1 μm . (b) One of the nanoflowers. Scale bar = 100 nm.	75
Figure 4-13. Scanning electron microscope images of the fabricated all-dielectric spiral nanoflowers. (a) Array of the nanoflowers. Scale bar = 1 μm . (b) One of the nanoflowers. Scale bar = 100 nm.	75

- Figure 4-14. Schematic of the optical characterization setup. The red beam is the incident light while the purple beams are the scattered light. LP: linear polarizer. QWP: quarter-wave-plate. BS: beam splitter. 76
- Figure 4-15. Experimental demonstration and validation of giant optical activity. (a) Scattering spectra of the nanoflower excited by LCP and RCP light. (b) CID between the LCP and RCP light. (c) Scattering spectra and CID of the nanoflower without the central nanocylinder. (d) Stack plot of the normalized scattering spectra of the nanoflowers with and without the central nanocylinder. 77
- Figure 4-16. Schematic diagram of Raman optical activity. 80
- Figure 4-17. Principles of superchiral-field-enhanced ROA using the silicon nanodisk array. (a) Schematic of the silicon nanodisk array. (b) Reflection spectrum of the silicon nanodisk array as a function of period P . (c) Electric field magnitude distribution in a unit cell of the nanodisk array. The black arrows indicate the directions of the electric fields while the white arrows indicate the directions of the magnetic fields. (d) Optical chirality distribution in a unit cell of the nanodisk array. 81
- Figure 4-18. Principles of superchiral-field-enhanced ROA using the silicon nanodisk array. (a) Schematic of the silicon nanodisk array. (b) Reflection spectrum of the silicon nanodisk array as a function of period P . (c) Electric field magnitude distribution in a unit cell of the nanodisk array. The black arrows indicate the directions of the electric fields while the white arrows indicate the directions of the magnetic fields. (d) Optical chirality distribution in a unit cell of the nanodisk array. 84
- Figure 4-19. Tuning the excited mode of the silicon nanodisk array. (a) Average electric-field magnitude and (b) average optical activity in the near-field region on the silicon nanodisk array as a function of the radius r and the height h of the nanodisks. 87
- Figure 4-20. Fabrication steps of the silicon nanodisk array. 88
- Figure 4-21. SEM images of the fabricated silicon nanodisk array. The insets are the zoom-in SEM images. 89

- Figure 4-22. Schematic of the reflection spectroscopy setup. OL: Objective lens. QWP: Quarter-wave plate. BS: Beam splitter. LS: Light source. LP: Linear polarizer. CC: CMOS camera..... 89
- Figure 4-23. Reflection spectra of the silicon nanodisk array excited by LCP and RCP incident light, respectively..... 90
- Figure 4-24. Two-phase virtual-enantiomer ROA setup. LP: Linear polarizer. QWP: Quarter-wave plate. HMF: Half-wave plate in a motorized flipper. BS: Beam splitter. HL: Halogen lamp. OAPM: Off-axis parabolic mirror. RHWP: Rotating half-wave plate. NF: Notch filter. CC: CMOS camera..... 91
- Figure 4-25. Superchiral-field-enhanced Raman and ROA spectra of toluene (an achiral sample). 93
- Figure 4-26. Raman and ROA spectra of (\pm)-alpha-pinene without and with the superchiral-field enhancement by the silicon nanodisk array. (a) Raman spectra of (\pm)-alpha-pinene on the silica substrate. (b) Raman spectra of (\pm)-alpha-pinene on the silicon nanodisk array. (c) ROA spectra of (\pm)-alpha-pinene on the silica substrate. (d) ROA spectra of (\pm)-alpha-pinene on the silicon nanodisk array. 94
- Figure 4-27. Experimentally achieved Raman and ROA enhancement factors of (\pm)-alpha-pinene by the silicon nanodisk array. (a) Enhancement factors of Raman peaks of (\pm)-alpha-pinene. (b) Enhancement factors of ROA peaks of (\pm)-alpha-pinene. (c) Near-field enhancement factors of Raman peaks of (\pm)-alpha-pinene. (b) Near-field enhancement factors of ROA peaks of (\pm)-alpha-pinene. 95
- Figure 4-28. Dissymmetric factor distribution in a unit cell of the silicon nanodisk array. 98
- Figure 5-1. Synthesis and characterization of the porous carbon nanowire array (PCNA). (a) Steps for synthesizing the PCNA. The bottom right inset shows an SEM image of the PCNA and an enlarged SEM image of a single PCNA nanowire. (b) Raman spectra of the PPNA and PCNA. After the carbonization process, all the characteristic Raman peaks of the PPNA at 870, 930, 1050, and 1246 cm^{-1} disappeared as evident in the PCNA spectrum. (c) I - V curve

measurements of the PPNA and PCNA. In the measurements, the length and contact area of the porous PPy nanowires and porous carbon nanowires are about 15 μm and 0.5 mm^2 , respectively. The conductivity of the substrate was significantly increased after the carbonization process, indicating the semiconducting property of the PCNA. (d) EDS spectra of the PPNA and PCNA. The composition ratio of carbon was significantly increased after the carbonization process. 102

Figure 5-2. SERS of R6G on the PCNA substrate. (a) Measured Raman spectra of R6G molecules at a concentration of 10 μM on the silicon (red), PNA (blue), CNA (orange), and PCNA (green) substrates for an integration time of 30 s with an excitation power of 1 mW at 785 nm after cleaning the substrates. (b) Measured Raman spectra of R6G molecules at different concentrations adsorbed on the PCNA substrate for an integration time of 30 s with an excitation power of 1 mW at 785 nm. (c) Intensities of the Raman peaks at different concentrations at 1185, 1309, 1361, 1507, and 1650 cm^{-1} . The detection limit of the PCNA substrate for R6G molecules is about 10 nM. (d) SERS reproducibility measurements of R6G molecules on different PCNA substrates. The differences in the relative intensities of the Raman peaks at 1185, 1309, 1361, 1507, and 1650 cm^{-1} between 20 different substrates are within a standard deviation of 5.7%. 104

Figure 5-3. Raman spectra of the DMSO on the silicon and PCNA substrates. Measured Raman spectra of the DMSO solutions with different mass fractions on the silicon and PCN substrates. With the enhancement of the PCNA substrate, all the Raman peaks of the DMSO solutions were identifiable even at the very low mass fraction of $5.5 \times 10^{-8}\%$ 105

Figure 5-4. SERS of β -lactoglobulin on the PCNA substrate. (a) Measured Raman spectra of β -lactoglobulin molecules on the silicon, PCNA, and commercial metal substrates. The Raman signal intensity of β -lactoglobulin molecules on the PCNA substrate is 10 times higher than on the metal substrate. (b) SERS maps of β -lactoglobulin on the PCNA substrate, showing high surface homogeneity in enhancement factor at two characteristic Raman shifts of the molecule on

both large and small scales with a step size of 1 μm and 0.1 μm , respectively.

(c) Histograms of the enhancement factors on the large and small scales. 107

Figure 5-5. SERS of glucose on the PCNA substrate. (a) Measured Raman spectra of glucose molecules on the silicon and PCNA substrates. (b) Time-to-time consistency of the PCNA substrate in the Raman spectrum. There are small hour-to-hour fluctuations in the Raman spectrum, showing high reproducibility and biocompatibility. 108

Figure 5-6. Raman peak assignments of R6G, β -lactoglobulin, glucose, and DMSO. a, R6G. b, β -lactoglobulin. c, glucose. d, DMSO. 110

Figure 5-7. Theory and experimental verification of the CM as the dominant enhancement effect of the PCNA substrate. (a) Energy level diagram of the PCNA-molecule system to explain the CM. The HOMO and LUMO of the molecule are bridged by the assistance of the energy bands of the PCNA substrate, enabling two possible resonant charge-transfer pathways. One is from the conduction band of the PCNA to the LUMO of the molecule while the other is from the HOMO to the conduction band. (b) Comparison in electric field magnitude distribution between the single CNA nanowire and the single PCNA nanowire to explain the small contribution of the EM. The largest electric field enhancement localized at the lateral edges of each PCNA nanowire is about 2, which corresponds to a small enhancement factor of ~ 16 . Compared with the CNA nanowire without the nanopores, the PCNA nanowire has a larger electric field magnitude due to the sharp edges of its porous structure. Due to the absence of strong structural resonance, the difference between the electric field magnitude distributions at the excitation wavelengths of 532 nm and 785 nm is very small. (c) Absorption and reflection spectra of the PCNA substrate. (d) Raman spectrum of β -lactoglobulin up to the high Raman shift region, showing no appreciable peaks of overtones and combination bands. (e) Raman spectra of β -lactoglobulin at different excitation wavelengths of 532 nm and 785 nm. 112

Figure 6-1. On-chip infrared frequency comb based on the high-Q microring resonator. 115

Figure 6-2. Highly sensitive on-chip chiral biosensor.....	116
--	-----

List of Tables

Table 1-1. Refractive indices and nonlinear refractive indices of CMOS-compatible group IV optical materials in integrated photonics.....	24
Table 5-1. Assignment of major peaks in the Raman spectra of R6G, β -lactoglobulin, glucose, and DMSO.....	110
Table 6-1. Summary of the demonstrated on-chip group IV photonic devices.....	114

Chapter 1

Introduction

1.1 Vibrational spectroscopy

Vibrational spectroscopy is a powerful optical technique to non-invasively probe vibrational signatures of molecules and, thereby, enables analysis of composite systems of physical, chemical, and biological interests due to its inherent selectivity [1, 2]. By virtue of its versatility for studying solid, liquid, and gas samples, vibrational spectroscopy has been used for a variety of intriguing applications, such as chemical detection, disease diagnosis, environmental monitoring, and industrial process control. Vibrational spectroscopy includes infrared spectroscopy and Raman spectroscopy which originate from two types of energy exchange between light and molecules [1]. An energy diagram of four types of light-molecule interaction is shown in Figure 1-1. Three of them, including infrared absorption, Stokes Raman scattering, and anti-Stokes Raman scattering, probe the vibrational energy states of the molecule. The infrared absorption corresponds to the absorption of an infrared photon accompanied by a vibrational transition from one vibrational energy state to the other. The absorbed infrared photon energy equals the energy difference between the two vibrational energy states involved for the transition. By measuring all the infrared absorption, an infrared spectrum of the molecule is obtained, which can be used to identify and study the molecule by virtue of its specificity. The technique used to measure the infrared spectrum of the molecule is the infrared spectroscopy. In comparison, the Stokes/anti-Stokes Raman scattering corresponds to the inelastic scattering of a photon accompanied by a vibrational transition from one vibrational energy state to the other, which is mediated by a virtual energy state. The energy difference between the incident photon and the inelastically scattered photon equals the energy difference between the two vibrational energy states involved for the transition. By measuring all the inelastic scattering with a fixed incident photon energy, a Raman spectrum of the molecule that includes both Stokes and anti-Stokes Raman scattering is obtained, which can also be used to identify and study the molecule by its specificity.

Correspondingly, the technique used to measure the Raman spectrum is the Raman spectroscopy.

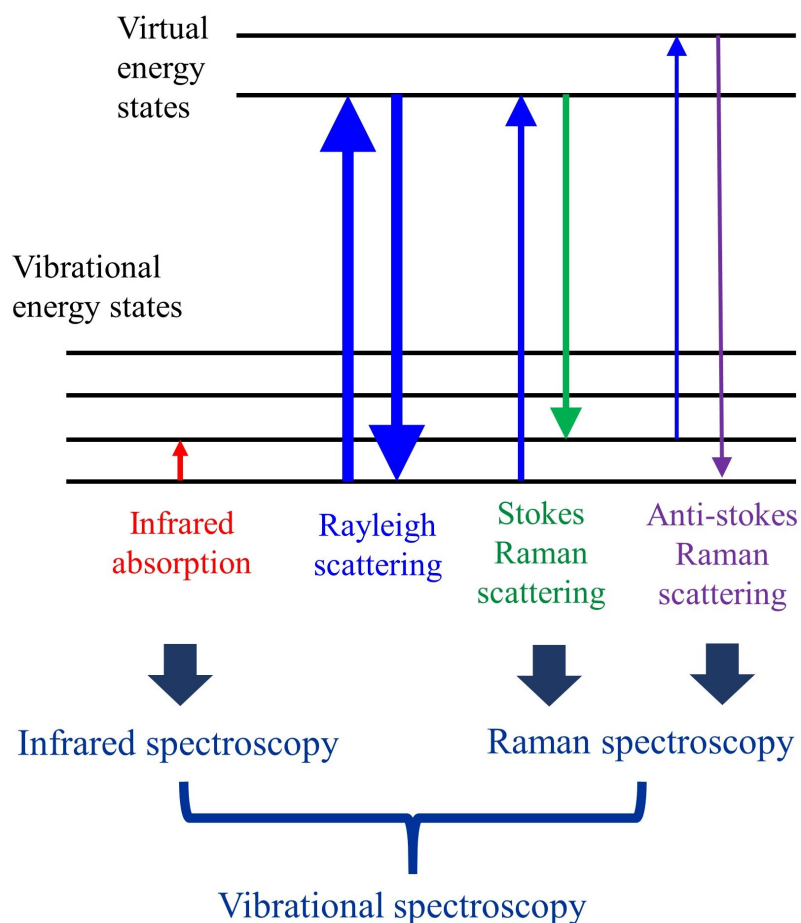


Figure 1-1. Energy diagram of four types of light-molecule interaction, including infrared absorption, Rayleigh scattering, Stokes Raman scattering, and Anti-stokes Raman scattering.

Nowadays, infrared spectroscopy has become one of the most widely used spectroscopic techniques for structural analysis of molecules by virtue of the continuous development of its experimental instrumentation [3-6]. The first batch of commercial infrared spectrometers became available since the 1940s. The infrared spectrometers at that time employed prisms as dispersive elements to distinguish infrared absorption peaks at different wavelengths. After several years' development, diffraction gratings were introduced to replace the prisms by merit of its flexible designability and excellent integratability. In the 1950s, Fourier-transform infrared (FTIR) spectrometers were experimentally realized, which dramatically boosted the development of infrared

spectroscopy. By exploitation of an interferometer and a well-established Fourier-transformation algorithm, the FTIR spectrometers significantly improved the quality of measured infrared spectra and effectively decreased the measurement time. Raman spectroscopy as another one of the most widely used spectroscopic techniques for structural analysis also relies on the development of its experimental instrumentation [7]. Although Raman scattering was discovered by C.V. Raman early in 1928 [8], due to its low sensitivity, the Raman spectroscopy was not rapidly advanced until the advent of lasers in the 1960s. However, the application of Raman spectroscopy for real molecular analysis still remained impeded by fundamental and technical problems, such as weak Raman signal intensity, high fluorescence background, low light collection efficiency, and low detection sensitivity. It was until 1986 that routine chemical analysis of molecules by using Raman spectroscopy became possible by the development of several important experimental instruments, including near-infrared lasers, charge-coupled devices (CCDs), and small computers [9, 10]. It can be seen from the above brief history that the development of experimental instrumentation played a critical role in the development of vibrational spectroscopy. This is still true for the modern vibrational spectroscopy until today. Nowadays, even though vibrational spectroscopy has enabled diverse interesting applications with its development in the past decades, most of these vibrational spectroscopic applications still remain confined to the laboratory environment [11]. This is partially due to the bulky and costly instrumentation of vibrational spectroscopy with moderate sensitivity.

1.2 On-chip photonic devices

Realization of on-chip photonic devices provides a promising solution to the above problem. By making use of photonic integrated circuits [12, 13], it is possible to integrate traditional vibrational spectroscopic instrumentation on a single photonic chip. All the essential photonic devices for vibrational spectroscopy, including light sources, optical waveguides, dispersive components, optical modulators, and optical detectors, can be functionally integrated on a single chip by utilizing the modern micro/nanofabrication technology. As shown in Figure 1-2, the miniaturization of vibrational spectroscopic instrumentation on a single chip will bring a lot of advantages to vibrational spectroscopic

applications, including portability, integratability, low cost, low power consumption, and high sensitivity. Among all the advantages, the high sensitivity as a performance advantage is beyond other intrinsic advantages of on-chip photonic devices, which plays a pivot role and requires delicate design. By utilizing strong electric field enhancement and high energy density in on-chip photonic devices, it is possible to significantly enhance the infrared absorption rate and Raman scattering rate of molecules on a chip. The enhancement can be achieved by developing optimized material platforms and feasible device design.

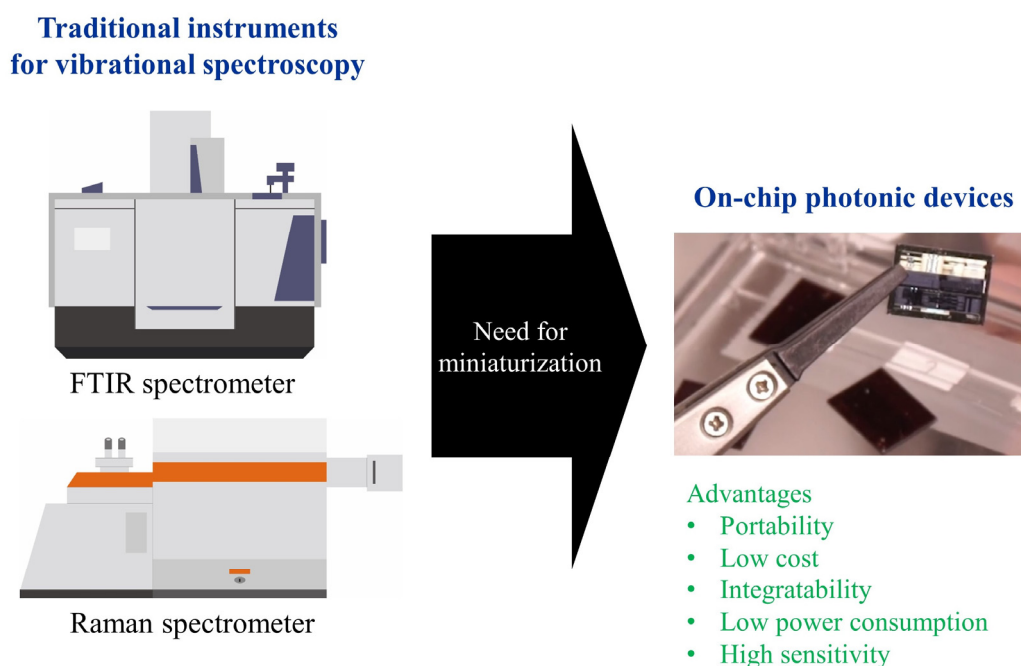


Figure 1-2. Miniaturization of traditional vibrational spectroscopy instruments by utilizing on-chip photonic devices.

The conventional working flow for realizing on-chip photonic devices is shown in Figure 1-3. First, a suitable integration platform is selected or developed based on requirement for specific applications. Several parameters of the integration platform, including the working wavelength, optical loss, refractive index and nonlinear optical coefficient, needs to be carefully considered. After selecting an integration platform, on-chip photonic devices are theoretically designed by combination of analytical methods and numerical simulations. Then, the specifically designed photonic devices are experimentally realized by using some nanofabrication techniques, such as electron-beam lithography (EBL), inductively coupled plasma (ICP) etching, and thermal evaporation.

Finally, the performances of the fabricated devices are characterized for the specific vibrational spectroscopic applications.

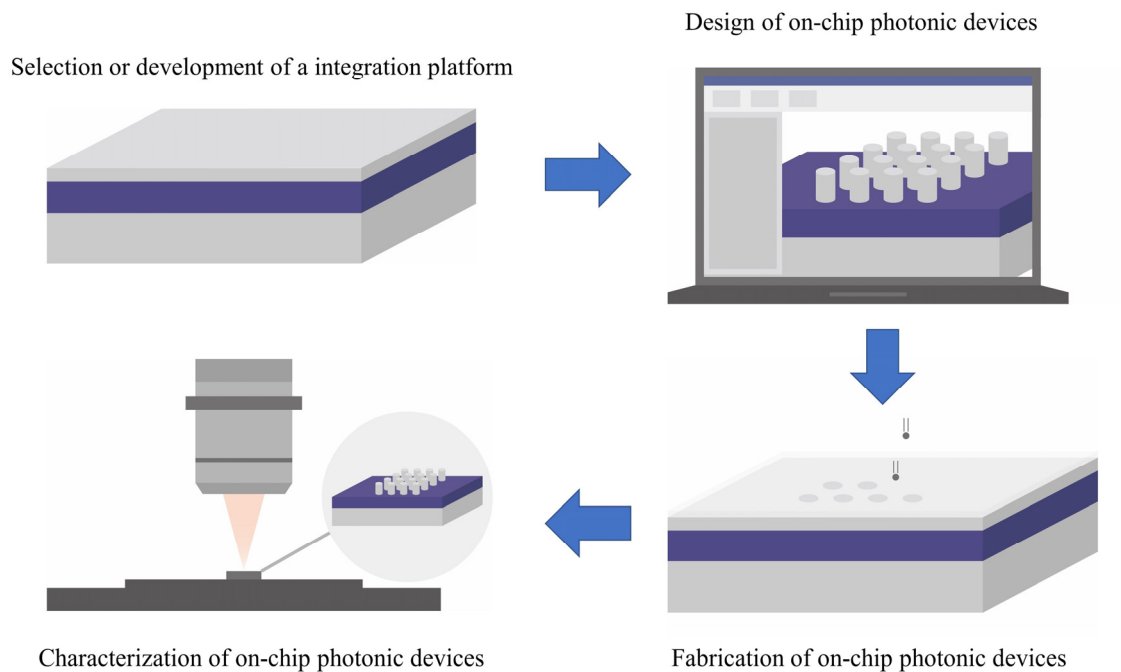


Figure 1-3. Working flow for realizing on-chip photonic devices for vibrational spectroscopic applications.

Selection or development of a suitable integration platform as the first step of the work flow for realizing on-chip photonic devices is significantly important as it fundamentally determines performances of potentially developed devices. Various integration platforms of on-chip photonic devices have been developed, involving a wide range of optical materials that include noble metals, two-dimensional materials, chalcogenide glasses, and group IV semiconductors (carbon, silicon, and germanium). Among them, group IV semiconductors provide mature and low-loss material platforms for integration owing to their CMOS-compatible fabrication conditions and all-dielectric environment, which are beneficial for high-volume production and low photothermal heat generation [14-16]. Therefore, I select group IV semiconductors (carbon, silicon, and germanium) as my integration platform materials for vibrational spectroscopy. The details of group IV optical materials as integration materials for on-chip photonic devices will be introduced in the next part.

1.3 Group IV optical materials

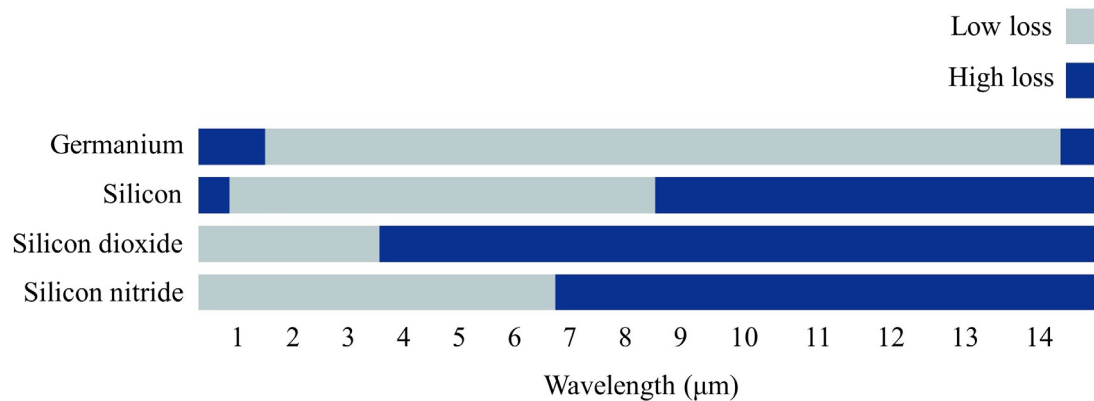


Figure 1-4. Transparency windows of CMOS-compatible group IV optical materials in integrated photonics.

Group IV optical materials, such as silicon, silicon dioxide, silicon nitride, germanium, germanium-tin alloy, and carbon, have been widely used in integrated photonics by virtue of their attractive optical properties for realization of compact and low-loss on-chip photonic devices [17-21]. Among them, silicon, silicon dioxide, silicon nitride, germanium, and carbon have the notable advantage of complementary metal oxide semiconductor (CMOS) compatibility, which is essential for practical applications with low-cost and high-volume production requirements. The transparency windows of some widely used group IV optical materials are shown in Figure 1-4. It can be observed that germanium possesses the broadest transparency window among all the materials. Its transparency window is up to around 15 μm , which is beneficial for infrared spectroscopic applications as it covers a broad fingerprint region. The refractive indices and nonlinear refractive indices of these materials are shown in Table 1-1. It can be seen that silicon and germanium have relatively larger refractive indices, which can be used to realize on-chip photonic devices with strong structural resonance. This enables strong electromagnetic field enhancement on a chip, which is applicable for highly sensitive vibrational spectroscopic applications. Moreover, silicon and germanium also have larger nonlinear refractive indices, which offers a new degree of freedom for manipulating light on a chip, potentially applicable for further optimization of on-chip vibrational spectroscopy.

	Silicon dioxide [22]	Silicon Nitride [22]	Silicon [22]	Germanium [23]
Refractive index	~1.47	~1.98	~3.4	~4.0
Nonlinear refractive index	$<10^{-20} \text{ m}^2/\text{W}$	$<10^{-19} \text{ m}^2/\text{W}$	$<10^{-18} \text{ m}^2/\text{W}$	$\sim 10^{-17} \text{ m}^2/\text{W}$

Table 1-1. Refractive indices and nonlinear refractive indices of CMOS-compatible group IV optical materials in integrated photonics.

Silicon as the most widely used group IV material is selected for Raman spectroscopy due to its high refractive index as well as low cost. By making use of its high refractive index, silicon photonic devices with strong optical confinement and resonance can be theoretically designed and experimentally fabricated. A large number of on-chip photonic devices with strong electromagnetic field enhancement have been experimentally demonstrated in silicon-based integration platforms, including silicon-on-sapphire waveguides [24, 25], silicon-on-LiNiO₃ waveguides [26, 27], silicon-on-Si₃N₄ waveguides [28], silicon microring resonators [29-32], and silicon photonic crystal cavities [33-35]. Compared with germanium, silicon is not only low-cost, but also has a relatively low loss in the visible and infrared spectral ranges, offering a better material platform for Raman spectroscopic applications. Germanium holds superior potential for infrared spectroscopic applications as it has the wide transparency window (2 - 15 μm), the higher refractive index (~ 4), and the high nonlinear refractive index ($\sim 10^{-17} \text{ m}^2/\text{W}$) [36]. Germanium photonic devices with strong structural resonance for highly sensitive infrared spectroscopy in the fingerprint region are experimentally realizable by its material properties. A number of preliminary mid-infrared (IR) germanium photonic devices have been demonstrated in recent years, including germanium-on-SOI waveguides [37, 38], germanium-on-Si₃N₄ waveguides [39], germanium-on-insulator (GOI) waveguides [40, 41], suspended germanium devices [16, 42], and silicon-germanium waveguides [43]. Additionally, carbon has also attracted a great deal of concern for realizing on-chip photonic devices in the last decade by virtue of their morphology-dependent material properties [44]. Carbon nanomaterials, including carbon nanotubes [45, 46], carbon nanowires [47, 48], and

graphene [49-51], have demonstrated their supreme material properties for development of photonic devices, such as tunable bandgaps, high carrier mobility, and high thermal stability. Moreover, carbon as the key element of life demonstrates excellent compatibility to biomolecules, which provides a biocompatible platform for achieving photonic sensors [44]. For example, graphene has been utilized to enhance Raman signals of biomolecules [52]. Despite these results, due to the limited quality and device designs of these traditional photonic devices, realization of on-chip group IV photonic devices for vibrational spectroscopy still remains challenging. To break through this bottleneck, on-chip group IV photonic devices with experimentally feasible theoretical design, optimized wafer development, and improved device fabrication processes are highly demanded.

1.4 Scope and structure of this thesis

The goal of this thesis is to propose and experimentally demonstrate several on-chip group IV photonic devices with controllable strong light-matter interaction for low-cost, highly sensitive vibrational spectroscopy. Specifically, my aim is to develop on-chip high-Q germanium photonic devices for infrared spectroscopy, on-chip silicon photonic devices with tailored structural resonance for Raman spectroscopy, and an on-chip carbon photonic device with strong chemical enhancement for Raman spectroscopy. The developed photonic devices are expected to involve a series of group IV elements and enable low-cost and highly-sensitive vibrational spectroscopy, providing a novel class of opportunities in analytical chemistry, pharmaceutical science, environmental safety, and pathology.

The structure of this thesis is as follows. In Chapter 2, basic principles of on-chip group IV photonic devices for vibrational spectroscopy are introduced. Specifically, the theory of highly sensitive vibrational spectroscopy enabled by the photonic devices is discussed. Moreover, the principles of theoretical design, experimental fabrication, and experimental characterization methods for realization of on-chip photonic devices are also introduced. In Chapter 3, on-chip germanium photonic devices for infrared spectroscopy are demonstrated. A novel suspended-membrane germanium integration platform that is developed in my doctoral work is introduced firstly. Based on this integration platform, three type of on-chip high-Q resonators, including a hexagonal-lattice zero-cell photonic crystal cavity, a photonic crystal nanobeam cavity, and a microring resonator, are

demonstrated one by one. In Chapter 4, on-chip silicon photonic devices for Raman spectroscopy are demonstrated. Two types of silicon devices, including a spiral nanoflower and a nanodisk array, are designed and experimentally demonstrated for highly sensitive Raman optical activity (ROA). In Chapter 5, an on-chip carbon photonic device, namely, a porous carbon nanowire array (PCNA) with strong chemical enhancement is experimentally realized for highly reproducible surface enhanced Raman spectroscopy. In Chapter 6, a brief summary of this thesis that includes the main work in my doctoral study is given. An outlook of the future research, including two practical scenarios based on my doctoral work, is also provided.

Chapter 2

Principles of on-chip photonic devices for vibrational spectroscopy

2.1 Overview

To realize on-chip photonic devices for vibrational spectroscopy, some theoretical design, experimental fabrication, and experimental characterization methods are required. It is essential to make clear their principles before implementation of them. In this Chapter, I will firstly introduce the theory of highly sensitive vibrational spectroscopy enabled by on-chip photonic devices. A theoretical analysis of light-molecule interaction on a chip is offered to instruct the design of on-chip photonic devices. Then, principles of the theoretical design methods, including the analytical method and finite element method (FEM), are introduced. This gives the detailed explanation of how these theoretical methods assist the device design. After that, principles of conventionally used fabrication methods, including electron beam lithography and inductively coupled plasma etching, is also introduced in this Chapter. This gives the detailed explanation of how these fabrication methods work to realize the designed devices. Finally, principles of two general optical setups used for the characterization are introduced.

2.2 Theory of highly sensitive vibrational spectroscopy

As mentioned in the introduction part, highly sensitive vibrational spectroscopy can be realized by electromagnetic field enhancement enabled by the on-chip photonic devices. This is because the electromagnetic field enhancement is able to increase the vibrational transition rate of molecules. To clarify this point, I used an analytical method to investigate the light-molecule interaction with electromagnetic enhancement. For simplicity but without loss of generality, I use the dipole approximation for the following deduction by assuming that the sizes of molecules are much smaller than the wavelength of light while high-order multipoles can be omitted. By applying Fermi's golden rule [53], the transition rate from one state to the other induced by the perturbation of light can be expressed as

$$W = \frac{2\pi}{\hbar^2} |p \cdot E|^2 g(\omega), \quad (2-1)$$

where \hbar is the reduced Planck constant, $p = \langle f | ex | i \rangle$ is the dipole moment of the transition from an initial state $|i\rangle$ to a final state $|f\rangle$, e is the elementary charge of an electron, x is the charge of the electron, E is the electric field amplitude that triggers the transition, and $g(\omega)$ is the mode density of a space for photons at angular frequency ω . The Fermi's golden rule above describes the transition rate induced by the electromagnetic perturbation of the light. It can be known from Eq. (2-1) that the transition rate is proportional to the electric field intensity $|E|^2$ as well as the mode density $g(\omega)$. Based on quantum optics, the zero-point energy $\frac{1}{2}\hbar\omega$ equals the electromagnetic field energy integrated through the space volume $\frac{1}{2} \int 2\varepsilon_0 E_{vac}^2 dV$, where E_{vac} is the amplitude of electric field of vacuum fluctuation while V is the volume of the space [54, 55]. Thus,

$$E_{vac} = \sqrt{\frac{\hbar\omega}{2\varepsilon_0 V}}. \quad (2-2)$$

The mode density of a free space can be expressed as

$$g(\omega) = \frac{\omega^2 V}{\pi c^3} \quad (2-3)$$

which is deduced from wave number space per unit volume $\frac{\omega^2}{\pi c^3}$ multiplied by the volume of the space V [56]. Therefore, the transition rate of a molecule in a free space can be obtained as

$$W_{free} = \frac{P^2 \omega^3}{\pi \varepsilon_0 \hbar c^3} \quad (2-4)$$

by substituting Eq. (2-1) and Eq. (2-2) into Eq. (2-3). Eq. (2-4) indicates that the transition rate of a molecule in a free space is determined by the dipole moment of the transition. For the on-chip photonic devices with strong structural resonance, they can be generally treated as optical resonators or cavities. According to cavity quantum optics, the mode density of an optical resonator or cavity with a resonant angular frequency of ω_{cav} , a spectral linewidth of $\Delta\omega_{cav}$, and a volume of V_c is

$$g(\omega) = \frac{2\Delta\omega_{cav}^2}{4\pi\Delta\omega_{cav}(\omega - \omega_{cav})^2 + \Delta\omega_{cav}^2}. \quad (2-5)$$

Thus, the transition rate of a molecule in the optical resonator or cavity can be expressed as

$$W_{\text{cav}} = \frac{2\pi p^2 \hbar \omega}{\hbar^2 2\varepsilon_0 V_c} \frac{2\Delta\omega_{\text{cav}}^2}{4\pi\Delta\omega_{\text{cav}}(\omega - \omega_{\text{cav}})^2 + \Delta\omega_{\text{cav}}^2}. \quad (2-6)$$

At the resonance condition of $\omega = \omega_{\text{cav}}$, it can be written as

$$W_{\text{cav}} = \frac{2p^2 \hbar Q}{\hbar \varepsilon_0 V_c}, \quad (2-7)$$

where $Q = \frac{\omega_{\text{cav}}}{\Delta\omega_{\text{cav}}}$ is the quality (Q) factor of the resonator or cavity. Based on Eq. (2-4) and Eq. (2-7), the enhancement factor of the transition rate, which is the so-called Purcell factor, can be acquired as

$$F = \frac{W_{\text{cav}}}{W_{\text{free}}} = \frac{Q(n\lambda)^3}{4\pi^2 V_c}. \quad (2-8)$$

where n and λ are the refractive index and the wavelength of the space, respectively. The Purcell factor is the enhancement factor of the number of photons emitted from the optical resonator or cavity, which equals the enhancement factor of the emitted light intensity. Therefore, it is obtained that

$$F = \left| \frac{E_{\text{cav}}}{E_{\text{free}}} \right|^2, \quad (2-9)$$

where E_{cav} and E_{free} are the electric field amplitudes in the optical cavity and the free space, respectively. By considering optical reciprocity theorem [57], the photons emitted from the optical resonator or cavity can be replaced by the excitation photons entering the optical resonator or cavity. In that case, F can also be considered as the enhancement factor of excitation. The above deduction omits the non-radiative loss in the optical cavity. If the non-radiative loss is also included, the enhancement factor of the transition rate can be modified as

$$F_R = \left| \frac{E_{\text{cavI}}}{E_{\text{free}}} \right|^2 = 1 + \frac{F\Delta\omega_{\text{cavR}}}{\Delta\omega_{\text{cavR}} + \Delta\omega_{\text{cavNR}}}, \quad (2-10)$$

where E_{cavI} is the electric-field amplitude in the cavity with non-radiative loss, $\Delta\omega_{\text{cavR}}$ is a spectral linewidth corresponding to radiative loss, $\Delta\omega_{\text{cavNR}}$ is the linewidth corresponding to non-radiative loss. From the above deduction, we can see that the on-chip photonic devices with strong structural resonance are capable of being utilized to enhance the transition rate of a molecule by its high-Q factors. From another perspective simply from Eq. (2-1), the enhanced electric field enabled by the on-chip devices can also lead to the enhanced transition rate of the molecule. Therefore, highly sensitive vibrational spectroscopy is realizable by employing on-chip photonic devices with high-

Q factors and high electric-field enhancement. The specific application of the above theory to infrared spectroscopy and Raman spectroscopy will be provided in the following two paragraphs.

In infrared spectroscopy, the infrared absorption cross-section of a molecule in the free space can be expressed as [58]

$$\sigma_{\text{abs}} = \frac{P_{\text{abs}}}{I_{\text{in}}}, \quad (2-11)$$

where I_{in} is the incident light intensity with a unit of $\text{W} \cdot \text{cm}^{-2}$, P_{abs} is the optical power absorbed by the molecule with a unit of W . The absorption cross-section σ_{abs} is proportional to the vibrational transition moment $\langle f_v | ex | i_v \rangle$ which reflects a vibrational transition from an initial vibrational state $|i_v\rangle$ to a final vibrational state $|f_v\rangle$ of the molecule. With the enhancement of the on-chip photonic devices, the enhanced infrared absorption cross-section can be written as

$$\sigma_{\text{Eabs}} = F_{\text{R}} \cdot \sigma_{\text{abs}}, \quad (2-12)$$

where F_{R} is the modified enhancement factor as expressed in Eq. (2-10), which is induced by the strong structural resonance of the devices. Therefore, highly sensitive infrared spectroscopy with a sensitivity enhancement factor of F_{R} can be expected by utilizing the on-chip photonic devices.

In Raman spectroscopy [59], the Raman cross-section of a molecule in the free space can be expressed by the relation of

$$\int_0^\infty P_{\text{Ra}}(\omega_{\text{Ra}}) d\omega_{\text{Ra}} = \int_0^\infty I_{\text{ex}}(\omega_{\text{ex}}) \sigma_{\text{Ra}}(\omega_{\text{ex}}, \omega_{\text{Ra}}) d\omega_{\text{Ra}}, \quad (2-13)$$

where I_{ex} is the incident light intensity with a unit of $\text{W} \cdot \text{cm}^{-2}$, P_{Ra} is the power of Raman scattering of the molecule with a unit of W , σ_{Ra} is the Raman scattering cross-section of the molecule, ω_{ex} is the angular frequency of the excitation light, and ω_{Ra} is the angular frequency of the Raman scattering. Similarly, the Raman scattering cross-section is proportional to the vibrational transition moment $\langle f_v | ex | m_v \rangle \langle m_v | ex | i_v \rangle$ which indicates a transition from an initial vibrational state $|i_v\rangle$ to an intermediate state $|m_v\rangle$ and a transition from the intermediate state $|m_v\rangle$ to a final vibrational state $|f_v\rangle$. Both transitions are enhanced by the on-chip photonic devices, which results in an enhanced Raman scattering cross-section σ_{ERa} with a relation of

$$\int_0^\infty \sigma_{\text{ERa}}(\omega_{\text{ex}}, \omega_{\text{Ra}}) d\omega_{\text{Ra}} = \int_0^\infty F_{\text{R}}(\omega_{\text{ex}}) \sigma_{\text{Ra}}(\omega_{\text{ex}}, \omega_{\text{Ra}}) F_{\text{R}}(\omega_{\text{Ra}}) d\omega_{\text{Ra}}, \quad (2-14)$$

where $F_R(\omega_{\text{ex}})$ and $F_R(\omega_{\text{Ra}})$ are the modified enhancement factors induced by the strong structural resonance of the device at the frequencies of the excitation light and Raman scattering. Correspondingly, highly sensitive Raman spectroscopy with a sensitivity enhancement relation of Eq. (2-14) can be expected by utilizing the on-chip photonic devices. Additionally, chemical enhancement induced by the charge-transfer resonance between the molecule and the on-chip photonic device is also able to enhance the Raman scattering cross-section of the molecule by increasing its vibrational transition rate.

2.3 Design of on-chip photonic devices

Based on the mechanism of highly sensitive vibrational spectroscopy in Part 2-2, on-chip photonic devices with strong structural resonance are designed by using two theoretical methods, including the analytical method and FEM method.

The analytical method is based on deduction of formulas to roughly determine the design of on-chip photonic devices. It usually requires a lot of reasonable simplification to get an analytical solution of the design. The analytical solution can help intuitively understand the underlying physics and significantly reduce the burden of precise simulations. For example, to design a silicon device with strong structural resonance by using a nanodisk configuration, Mie resonance which is analytically solvable for simple geometries can be employed. The radius of the silicon nanodisk R for a specific Mie resonance wavelength λ can be estimated by the simplified analytical equation of the Mie resonance condition $2R = \lambda/n$ [60], where n is the refractive index of the silicon at the wavelength of λ . For an excitation wavelength of 785 nm, the radius of the silicon nanodisk is calculated to be around 106 nm as the refractive index is around 3.7. A more precise value can be confirmed by a theoretical simulation with a parametric sweep of the radius just around 106 nm.

The FEM method is a numerical simulation method that enables precise design of on-chip photonic devices. As light in the on-chip photonic devices is governed by Maxwell equations, the FEM method for the device design is to solve the Maxwell equations in spatial domains of the device and its environment. The FEM method will firstly divide the domains into smaller, simpler parts which are called finite elements. The meshes shown in Figure 2-1(a) are the finite elements. The Maxwell equations which are originally partial

differential equations can be converted to algebraic equations correspondingly. The algebraic equations that govern these finite elements are then related and assembled into a large system of equations for the whole domain. By making use of boundary conditions of the whole domain, the FEM method uses variational methods to approximate a solution for the large system of equations by convergence of an associated error function [61]. Thus, the Maxwell equations of the photonic devices can be fully numerically solved. The electric field magnitude distribution as shown in Figure 2-1(b) is thus obtained by the simulation, which can be used to estimate the performances of on-chip photonic devices.

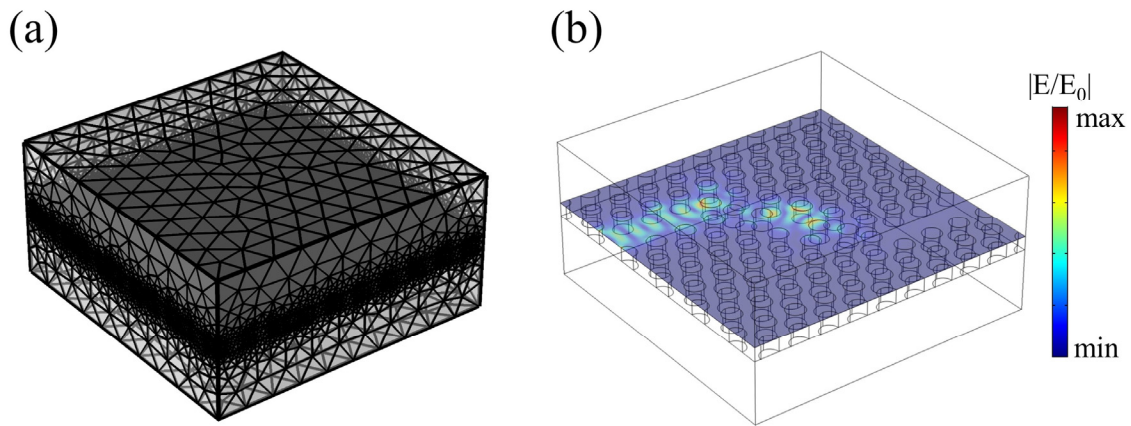


Figure 2-1. FEM simulations. (a) Meshes of an on-chip photonic device. (b) Electric field magnitude distribution of an on-chip photonic device.

2.4 Fabrication of on-chip photonic devices

Based on the theoretical design, the on-chip photonic devices are experimentally realized by utilizing nanofabrication methods. Electron-beam lithography and inductively coupled plasma etching are two main nanofabrication methods in my doctoral work. The principles of these two methods will be introduced in detail in this part.

Electron-beam lithography, which is also abbreviated as EBL, is a high-resolution electron-beam writing method to create patterns of designed photonic devices in an electron-sensitive resist [62]. The solubility of the resist is changed after being exposed by the electron beam. After a developing process, that is, immersing the exposed chip into a solvent, the exposed regions will be dissolved (positive resist) or left (negative resist) on the substrate as a mask for the etching or evaporation. The created patterns can be

subsequently transferred to the substrate by an etching or evaporation process. The electron-beam writer I used in my doctoral work is EB Advantest F7000S in Takeda Cleanroom at the University of Tokyo, which is shown in Figure 2-2(a). This electron-beam writer has an acceleration voltage of 50 kV, a spatial resolution of 20 nm, and an alignment precision of 10 nm.

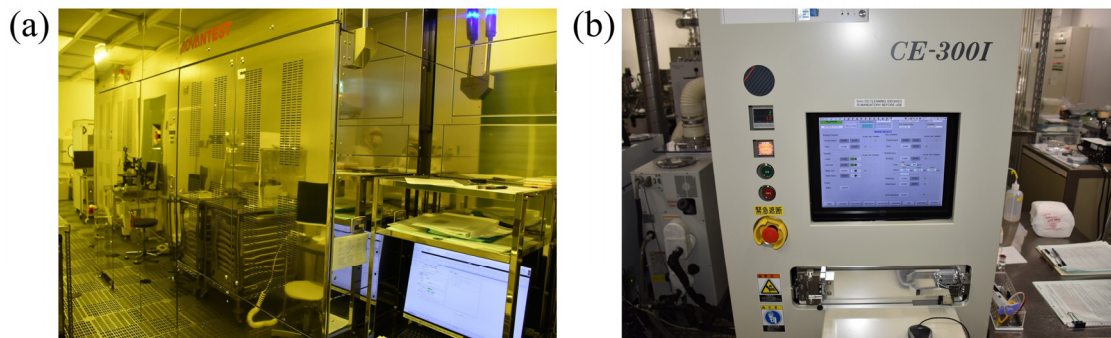


Figure 2-2. Fabrication equipment. (a) Electron-beam writer: EB Advantest F7000S in Takeda Cleanroom at the University of Tokyo. (b) Inductively coupled plasma etcher: ICP-RIE Ulvac CE-300I in Takeda Cleanroom at the University of Tokyo.

Inductively coupled plasma etching, which is abbreviated as ICP etching, is a semiconductor etching method based on the use of an inductively coupled plasma source [63]. The source is able to ionize gas molecules and atoms at a low pressure by creating an alternating radio-frequency magnetic field. The induced radio-frequency electric field can assist to generate the plasma by energizing electrons to interact with the gas molecules and atoms. After the generation of plasma, a direct-current bias is applied to make the plasma be attracted to the wafer such that the accelerated plasma can etch the target wafer by both chemical reaction and physical etching. One of the inductively coupled plasma etchers I used in my doctoral work is ICP-RIE Ulvac CE-300I in Takeda Cleanroom at the University of Tokyo. This etcher is equipped with CF_4 , CHF_3 , SF_6 and some other gases for etching group IV semiconductors, such as silicon and germanium.

2.5 Characterization of on-chip photonic devices

After the experimental fabrication of the designed photonic devices, two general optical setups are mainly used to characterize their performances for vibrational spectroscopy. One is a fiber-coupled measurement setup, which is mainly used for characterizing on-chip

germanium photonic devices for infrared spectroscopy. The other is an objective lens-coupled measurement setup, which is mainly used for characterizing on-chip silicon and carbon photonic devices for Raman spectroscopy.

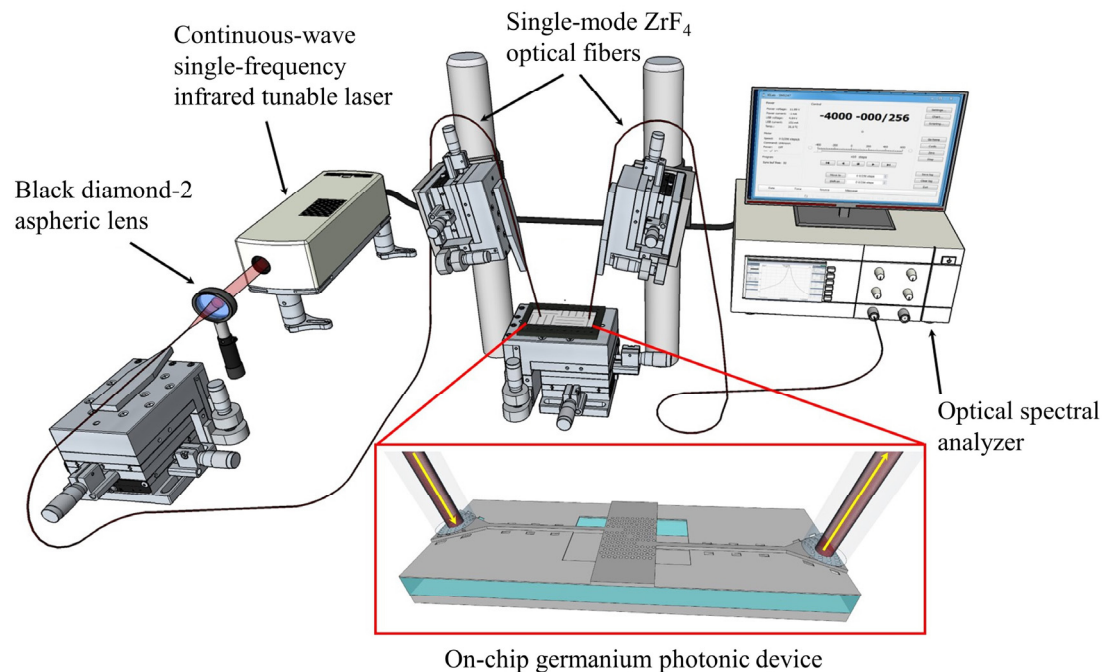


Figure 2-3. Fiber-coupled optical setup for the characterization of on-chip germanium photonic devices for infrared spectroscopy.

The fiber-coupled optical setup used for characterization of the on-chip germanium devices is schematically shown in Figure 2-3 [14-16]. The light source in the optical setup is a continuous-wave single-frequency infrared tunable laser which was controlled by using a software tool. The output light from the laser is firstly coupled into a single-mode ZrF₄ optical fiber by using a black diamond-2 aspheric lens. Then, the light from the end of the fiber is coupled into an on-chip germanium device via a grating coupler fabricated on the chip. In addition, another single-mode ZrF₄ optical fiber is employed to receive the output light coupled out from the device by the other grating coupler. The other end of the ZrF₄ fiber was connected to an optical spectral analyzer such that the transmission spectrum of the device was measured by continuously tuning the output wavelength of the laser. From the transmission spectrum measurement of the device, the Q factor of the

device is obtained, which can be used to estimate its performance in infrared spectroscopic applications as analyzed in the mechanism part above.

The objective lens-coupled optical used for characterization of the on-chip silicon and carbon photonic devices for Raman spectroscopy is schematically shown in Figure 2-4 [64]. The specific optical components, including the light source, polarization controllers, detectors, and so on, vary from characterization to characterization. The incident light, such as broadband white light and 532-nm green light, is coupled to a device on the photonic chip by light focusing through an objective lens. The reflected light from the device or Raman scattering light from the molecules on the device is collected by the same objective lens, which is then coupled to the corresponding spectrometer for experimental analysis. Thus, the performances of these on-chip photonic devices for Raman spectroscopic applications can be characterized

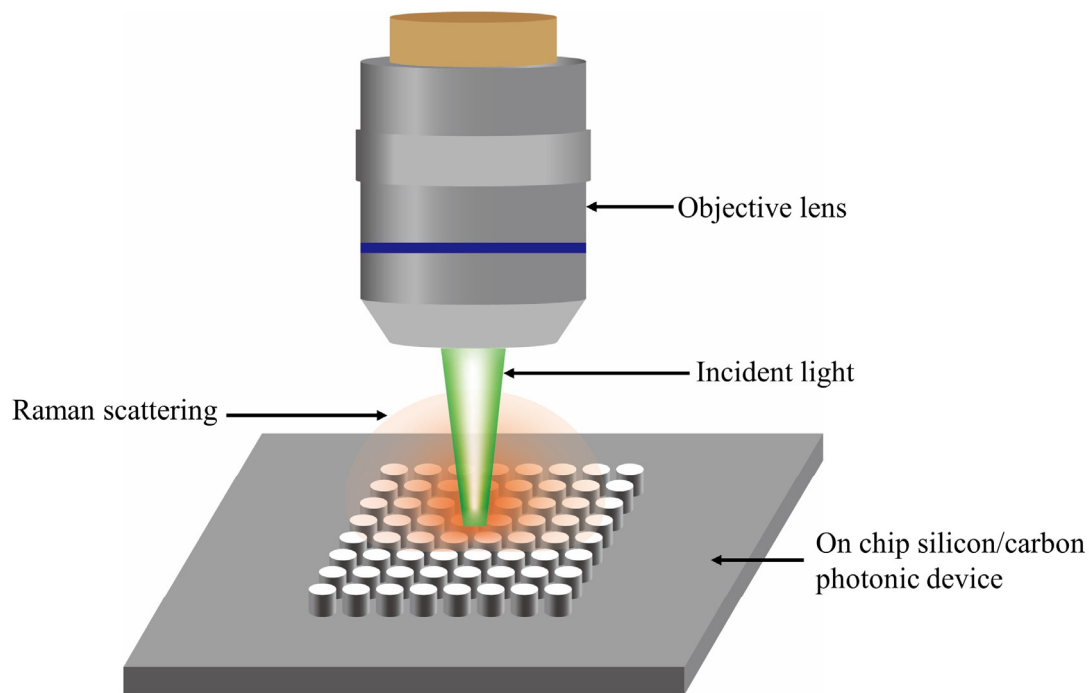


Figure 2-4. Objective lens-coupled optical setup for the characterization of on-chip silicon/carbon photonic devices for Raman spectroscopy.

Chapter 3

Demonstration of on-chip germanium photonic devices for infrared spectroscopy

3.1 Introduction

Germanium is selected as the integration material for developing on-chip photonic devices for infrared spectroscopy as it not only carries forward the CMOS compatibility as silicon, but also boasts several advantages over silicon, such as a wider spectral transparency window (2 - 15 μm) and a higher refractive index (~ 4) [65]. Especially, the wider spectral transparency window enables the developed photonic devices to work in the mid-infrared spectral range that encompasses the fingerprint region for infrared spectroscopic applications.

Due to these excellent properties of germanium, a number of fundamental devices based on germanium platforms have been developed in recent years, such as germanium-on-silicon waveguides [66-68], germanium-on-silicon-on-insulator (Ge-on-SOI) waveguides [37, 38], germanium-on-Si₃N₄ waveguides [39], and germanium-on-insulator (GOI) waveguides [40, 41]. However, what still remains challenging is germanium-based on-chip devices with strong light-matter interaction, which is essential for highly sensitive infrared spectroscopic applications.

To make full use of the wide spectral transparency window of germanium, I developed a germanium suspended-membrane integration platform in my doctoral work. The suspended integration platform was achieved by using hydrogen fluoride (HF) to permeate and etch out the buried oxide (BOX) and Al₂O₃ layers in a germanium-on-insulator wafer fabricated in our lab. Based on this platform, I experimentally demonstrated three types of infrared high-Q germanium devices with strong light-matter interaction, including a hexagonal-lattice zero-cell photonic crystal cavity, a photonic crystal nanobeam cavity, and a microring resonator. The details of theoretical design, experimental fabrication, and

experimental characterization of these high-Q germanium devices will be introduced in this Chapter.

3.2 Suspended-membrane integration platform

3.2.1 Theoretical design

The theoretical design of the germanium suspended-membrane integration platform is schematically shown in Figure 3-1. It is designed on a germanium-on-insulator (GOI) chip fabricated in our lab, which consists of a top germanium layer, buried oxide (BOX) and Al_2O_3 layers, and a silicon substrate. The suspended-membrane configuration is designed to be formed by etching out the parts of buried oxide (BOX) and Al_2O_3 layers below the photonic devices. This platform is advantageous over germanium-on-silicon, Ge-on-SOI, and GOI platforms in that it circumvents the large leakage of guided light into the silicon layers on the germanium-on-silicon and Ge-on-SOI platforms and the strong optical absorption of the oxide layer at wavelengths above $2.5\text{ }\mu\text{m}$ on the GOI platform. This platform enables full use of the transparency window of germanium ($2 - 15\text{ }\mu\text{m}$) that covers the fingerprint region, which possesses superior specificity for infrared spectroscopic applications.

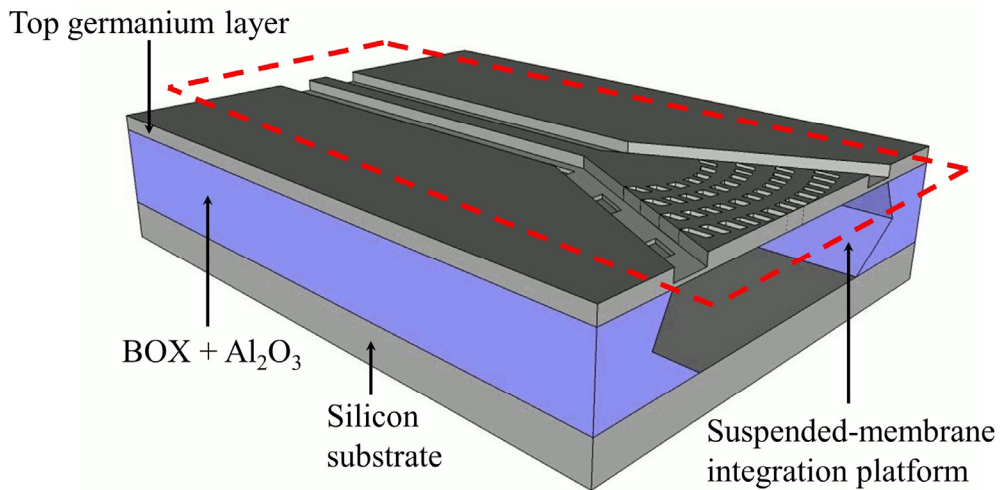


Figure 3-1. Schematic diagram of the germanium suspended-membrane integration platform.

3.2.2 Experimental fabrication

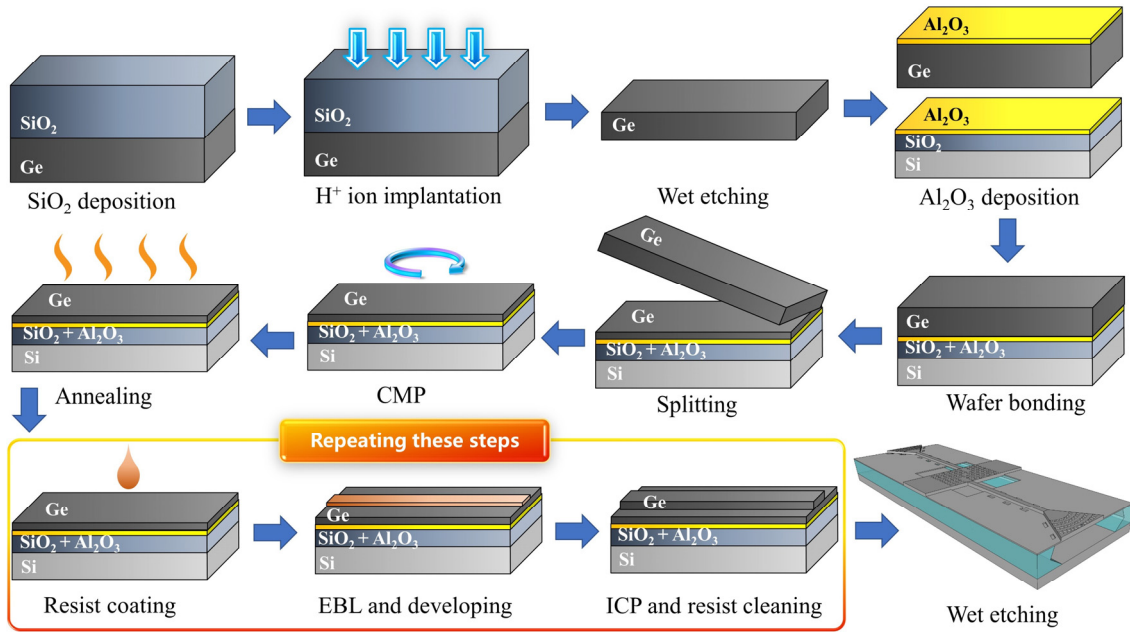


Figure 3-2. Fabrication process of the GOI wafer and the infrared suspended-membrane germanium photonic device.

Based on the above theoretical design, I experimentally fabricated the germanium suspended-membrane integration platform by using the fabrication flow as shown in Figure 3-2. A SiO_2 capping layer was firstly deposited on a Ge bulk via plasma enhanced chemical vapor deposition (PECVD), and then removed by wet etching after H^+ ion implantation. The H^+ ion implantation process created a layer of gaseous microbubbles in the Ge bulk. Next, 5-nm-thick Al_2O_3 layers were deposited as bonding interfaces on surfaces of the Ge bulk and a pre-prepared SiO_2 -covered Si wafer by using atomic layer deposition (ALD). After that, wafer splitting was conducted by heating. This is because the heating process creates a pressure effect in the microbubbles, which split the wafer. The above process is the so-called Smart-Cut method. Then the top Ge surface was polished by using chemical-mechanical planarization (CMP). At last, annealing is performed again for reducing defects and improving quality of the top germanium layer. By using the above GOI wafer, the on-chip photonic devices were fabricated by repeating the following three steps several times. The first two steps are to define patterns of the photonic devices, which includes resist coating followed by electron-beam lithography

(EBL). The third step is to transfer the patterns from the resist to the GOI wafer, which is realized via inductively coupled plasma (ICP) etching by using a mixed gas of CHF_3 and SF_6 . Finally, the fabricated photonic devices are soaked in the HF solution, which is also called wet etching, to remove the parts of BOX and Al_2O_3 layers below the photonic devices for realization of the suspended-membrane integration platform.

The scanning electron microscope (SEM) image of the fabricated platform is shown in Figure 3-3. Even though the top germanium layer is suspended between two air-cladding layers, no structural bending is observed, which indicates an excellent mechanical stability of the platform.

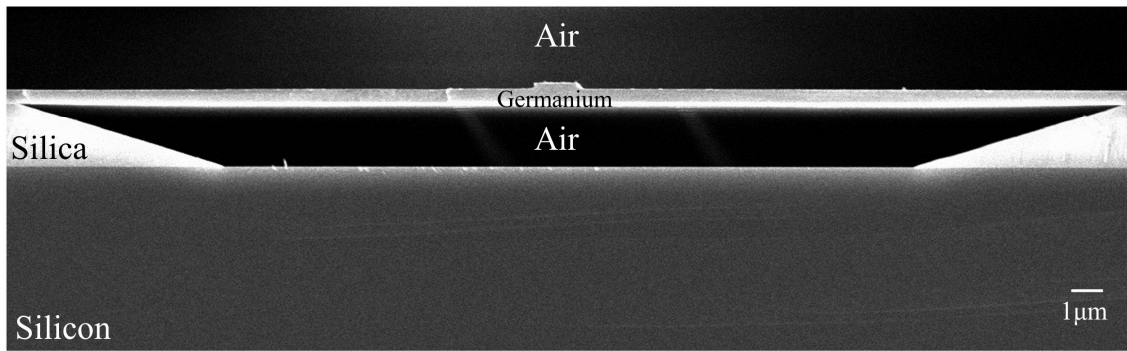


Figure 3-3. Cross-section of the germanium suspended-membrane integration platform.

3.3 Hexagonal-lattice zero-cell photonic crystal cavity

3.3.1 Overview

Photonic crystal is a periodic optical structure that affects the motion of photons in the same way that ionic lattices affect electrons in solid [69, 70]. By utilizing its photonic bandgap, photons with energy in the bandgap can be confined and oscillate in a defect of the photonic crystal. The defect surrounded by the photonic crystal forms the so-called photonic crystal cavity while the defect modes appeared in the bandgap of the photonic crystal correspond to the cavity modes. The formation of the cavity can significantly enhance the localized electromagnetic field of the input light, which can be employed for sensitivity enhancement of the infrared spectroscopic applications. A hexagonal-lattice zero-cell photonic crystal cavity is a defect in a hexagonal-lattice periodic optical structure. The defect that forms the zero-cell photonic crystal cavity is achieved by shifting positions of the surrounding “atoms” of the photonic crystal rather than eliminating some “atoms”.

For my on-chip germanium photonic crystal slabs, these “atoms” are air holes etched in the top germanium layer.

In this part, I proposed and experimentally demonstrated the first on-chip mid-IR germanium photonic crystal cavity that covers the entire fingerprint region [16]. This was enabled by harnessing the suspended-membrane germanium platform and monolithically integrating a photonic crystal cavity, two photonic crystal waveguides, two cantilever waveguides, two suspended membrane waveguides, and two focusing subwavelength grating couplers on a single chip.

3.3.2 Theoretical design

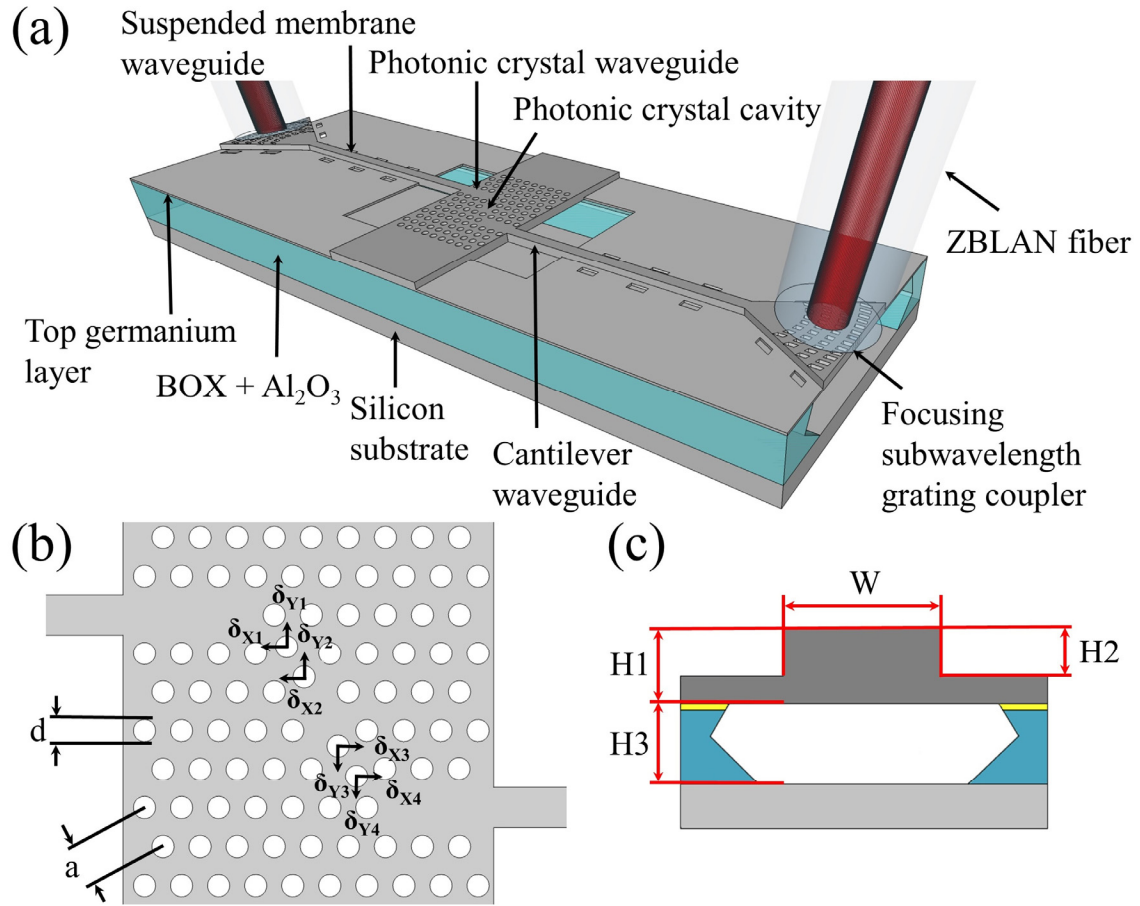


Figure 3-4. Schematic of the monolithically integrated on-chip MIR germanium device that contains a photonic crystal cavity, two photonic crystal waveguides, two cantilever waveguides, two suspended membrane waveguides, and two focusing subwavelength grating couplers. (a) Three-dimensional view of the device. (b) Top view of the photonic crystal cavity and waveguides. (c) Cross-sectional view of the suspended membrane waveguide.

The infrared germanium device, which is designed on a home-made GOI wafer, is schematically illustrated in Figure 3-4(a). The central part of the device is a hexagonal-lattice zero-cell (h_0) photonic crystal cavity and two photonic crystal waveguides connected by two cantilever waveguides. To couple light into the device and characterize its performance, two focusing subwavelength grating couplers were designed to realize optical coupling between the suspended membrane waveguides and IR single-mode ZrF₄ fibers. The angle of the tapered structures in the grating couplers is 37 degrees. With the intention to construct an air-cladding platform and to make full use of the germanium transparency window, two rows of periodic holes were designed along the ridge waveguides to allow hydrogen fluoride (HF) to permeate and etch out the buried oxide (BOX) and Al₂O₃ layers in the GOI wafer. The specific design of the photonic crystal cavity and waveguides is shown in Figure 3-4(b). A two-dimensional photonic crystal with triangular-lattice air holes was designed on the top germanium layer of the wafer. The period of the photonic crystal, a , and the diameter of the air holes, d , were determined based on the TE-like normalized photonic bands of the photonic crystal in the top germanium layer. Due to the scaling law of photonic crystals, our design can be applied in the whole fingerprint region as long as the material platform is transparent. Here, I set the central wavelength of the TE-like bandgap to be 2.35 μm , such that the period, a , and the diameter, d , were determined to be 673 nm and 404 nm, respectively. Two W1 photonic crystal waveguides, formed by eliminating two rows of air holes, are coupled with a photonic crystal cavity. The photonic crystal cavity is a h_0 cavity formed by shifting four air holes and optimized by eigenmode calculation. The horizontal shifts of the two internal air holes, δ_{x2} and δ_{x3} , are equal to 130 nm while the vertical shifts, δ_{y2} and δ_{y3} , are equal to 227 nm. For the two external air holes, the horizontal shifts, δ_{x1} and δ_{x4} , are equal to 50 nm while the vertical shifts, δ_{y1} and δ_{y4} , are equal to 87 nm. In order to realize a Fano-resonant lineshape, which is more sensitive to the variation of the surrounding environment in sensing applications, I achieved interference of the two cavity modes by further shifting the two external air holes along the horizontal axis to make them non-collinear with the other air holes. This made the horizontal shifts, δ_{x1} and δ_{x4} , equal to 151 nm. In addition, the cross-sectional dimensions of the suspended membrane waveguide used for the interconnection between the focusing subwavelength grating couplers and cantilever

waveguides are illustrated in Figure 3-4(c). The suspended membrane waveguide with a width W of 0.9 μm and an etch depth H_2 of 150 nm, which can only support the fundamental mode, was designed on the 300 nm-thick (H_1) top germanium layer. The BOX and Al_2O_3 layers (H_3) with a total thickness of 2 μm were designed to be removed to form the air-cladding platform. This configuration not only supplied a symmetric refractive index environment that resulted in excellent confinement of the propagating light, but also expanded the working wavelength to the whole fingerprint region.

Based on the above design, I investigated the performance of the photonic crystal cavity and waveguides by three-dimensional finite element method (FEM) simulation [61]. The simulation was conducted by using a commercial software tool (COMSOL Multiphysics). The thickness of the perfectly matched layer (PML) used in the simulation is 1 μm , which guarantees the complete absorption of the reflected and transmitted light at the boundaries. The total number of elements in the simulation is 458,509, ensuring the convergence and the high precision of our simulation. The transmission is defined as the ratio of the output electric-field magnitude to the input electric-field magnitude. Firstly, I calculated the transmission spectrum of the cavity without the further shifts of two external air holes for the coupling of two cavity modes. It was observed from Figure 3-5(a) that two transmission peaks appear in the spectrum at wavelengths of 2.30 μm and 2.335 μm , respectively, corresponding to the resonances of the two cavity modes. The effective mode volumes of these two cavity modes, defined as $\int \epsilon |E|^2 dV / (\epsilon |E|^2)_{\text{max}}$, are 0.079 μm^3 and 0.086 μm^3 . Here ϵ and $|E|$ are permittivity and electric-field magnitude at different positions of the cavity while V represents the whole volume of the cavity. The quality factors of these two resonances are equal to ~ 800 and ~ 2300 , reflecting the radiation losses of the cavity. It is worthwhile to note that the quality factors of the cavity modes in the waveguide-coupling configuration are smaller than those of identical isolated cavity modes because the waveguide-coupling configuration supplies a radiation-loss pathway for the cavity. Nevertheless, in order to realize a totally monolithic on-chip device with the in-plane excitation of photonic crystal cavity modes, it is inevitable to sacrifice a portion of the quality factor through the implementation of a waveguide-coupling configuration. Moreover, it can be observed from the figure that the transmission peak with the smaller quality factor has the higher transmission. This is because the higher transmission, which indicates a stronger coupling

between the cavity mode and the waveguide mode, results in a stronger radiation loss of the cavity by the pathway of the waveguide coupling, finally leading to decrease of the quality factor. The electric-field magnitude distributions of the coupling system at the wavelengths of two transmission peaks are displayed in the insets of Figure 3-5(a). Strong field enhancement attributed to the cavity resonances is indicated at these two wavelengths. The field distributions illustrate that the coupling between the waveguide and cavity is achieved by the evanescent field. As the overlap between the evanescent cavity field and the waveguide mode is larger at the wavelength of $2.30\ \mu\text{m}$, the coupling is stronger, such that the transmission is higher.

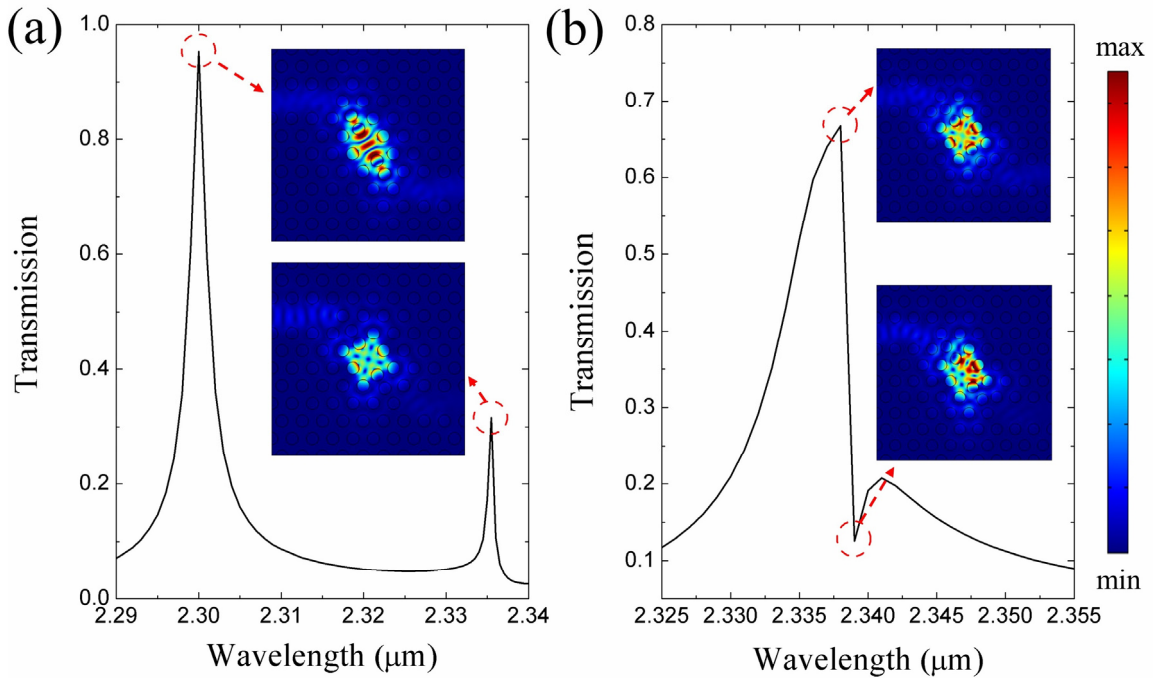


Figure 3-5. Design of the photonic crystal cavity. (a) Transmission spectrum and electric-field magnitude distributions in the cavity without a coupling of the two cavity modes. (b) Transmission spectrum and electric-field magnitude distributions in the cavity with a coupling of the two cavity modes (Fano resonance).

To achieve Fano resonance based on the two excited cavity modes, I further shifted the two external air holes along the horizontal axis to realize the coupling of these two modes. With the increase of the shifts, both of the transmission peaks redshifted. The peak at the wavelength of $2.30\ \mu\text{m}$ redshifted faster and finally caught up with the other

transmission peak, leading to the interference of the two cavity modes at the wavelength around $2.34\ \mu\text{m}$. The interference of the two cavity modes with different quality factors forms a steep Fano-resonant lineshape, as demonstrated in Figure 3-5 (b). The decrease of

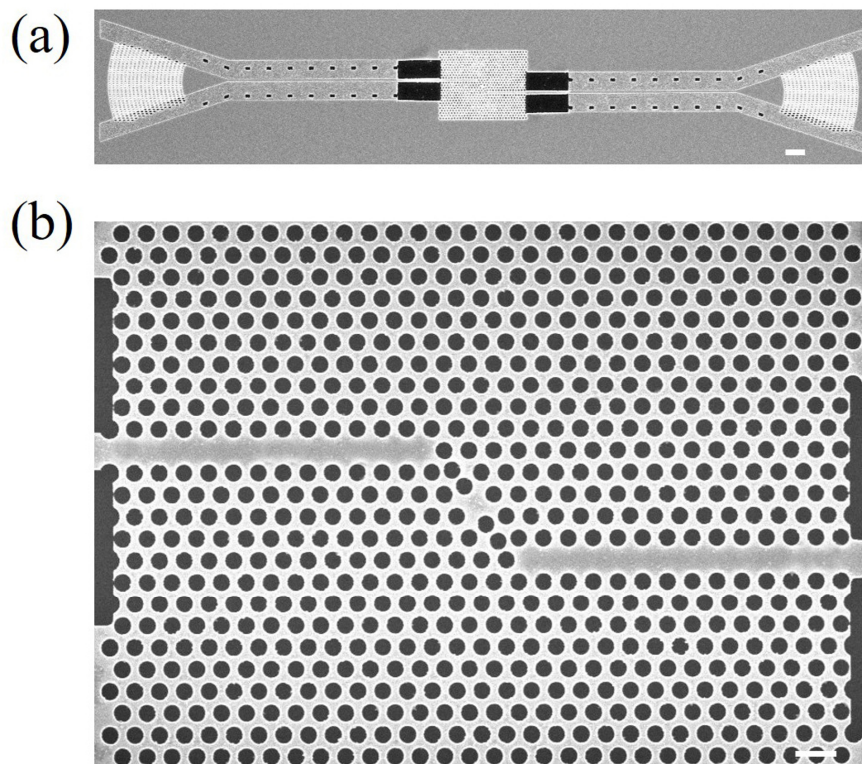


Figure 3-6. SEM images of the monolithically integrated on-chip IR germanium device. (a) Top view of the device. Scale bar: $5\ \mu\text{m}$. (b) Top view of the photonic crystal cavity and waveguides. Scale bar: $1\ \mu\text{m}$.

the transmission originates from the difference between the input and output waveguide-cavity coupling strengths that lead to the additional reflection of the input light. The insets display the field distributions at both the peak and the dip of the Fano-resonant transmission spectrum, indicating that the high and low transmission at these two wavelengths originated from the constructive and destructive interference of the two cavity modes. Additionally, the interference of the two cavity modes expanded the bandwidth of the field enhancement, which is beneficial for the measurement of molecular fingerprint absorption dips. In sensing applications based on infrared spectroscopy, the refractive index variation and the vibrational fingerprint absorption of molecules, which corresponds

to the lineshape shift and absorption dip in the spectrum, need to be measured simultaneously. Thus, a lineshape that is not only sensitive to the surrounding refractive index, but also has a relatively broad bandwidth capable of covering the target fingerprint absorption dip is required. The Fano resonance achieved by the interference of the two cavity modes optimized both the sensitivity and bandwidth of our device.

3.3.3 Experimental fabrication

In the light of the above numerical simulation, I experimentally fabricated our proposed IR germanium device. A scanning electron microscope (SEM) image of the monolithically integrated device is shown in Figure 3-6(a). The whole device was fabricated on a home-made GOI wafer whose dimensions are identical to the design shown in Figure 3-4(c). After carefully optimizing the length of the cantilever waveguides, the whole device shows high mechanical stability. The SEM image of the photonic crystal cavity and waveguides is shown in Figure 3-6(b), from which the intended shifts of the two external air holes, as designed in theory, are clearly observed. These shifts led to the interference of the two cavity modes and produced the Fano-resonant lineshape as designed.

3.3.4 Experimental characterization

After fabricating the device, I experimentally characterized its performance by measuring and evaluating its transmission spectrum. In order to eliminate the influence of background intensity, I firstly measured the coupling efficiency of the focusing subwavelength grating coupler used for coupling light into the device, which is shown in Figure 3-7. In the measurement, input and output focusing subwavelength grating couplers were connected with a short suspended-membrane germanium waveguide (200 μm) whose propagation loss is negligible. The focusing subwavelength grating couplers exhibited a broadband coupling efficiency. The highest coupling efficiency of the focusing subwavelength grating couplers in this spectral range was about -13 dB. The small Fabry–Perot ripples in the coupling profile indicate small back-reflection which reduces an undesirable effect of reflected light in the device. After being divided by the background intensity, that is, the product of the light source intensity and the grating coupling efficiency, the lineshape that reflects the real performance of the photonic crystal cavity was obtained as shown in Figure 3-7. A Fano-resonant dip was measured at the wavelength around 2.34 μm , which is in

agreement with our design. Calculated by the measured width of the high transmission peak in the Fano-resonant lineshape, the quality factor of this resonant peak is around 200, which is smaller than the quality factor of the simulation result (~ 400) in Figure 3-5(b). This is due to the fabrication imperfection that gave rise to an additional loss of the photonic crystal cavity. The expansion of the bandwidth resulting from the Fano resonance was also identified experimentally and is in agreement with the theoretical design.

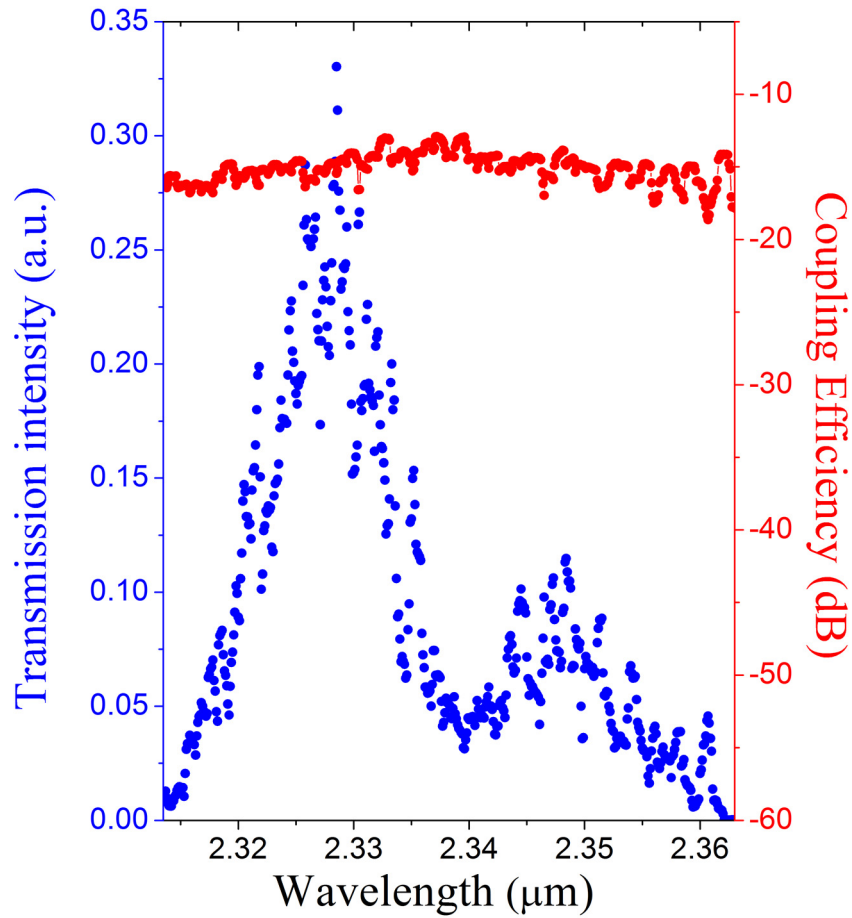


Figure 3-7. Measured transmission spectrum of the monolithically integrated on-chip IR germanium device (blue) and measured coupling efficiency of the focusing subwavelength grating couplers and suspended waveguide (red).

3.3.5 Summary

In summary, I proposed and experimentally demonstrated the first mid-IR germanium photonic crystal cavity that covers the fingerprint region. The performance of the cavity was predicted by the numerical simulation and verified by the experimental

characterization. By making use of the focusing subwavelength grating couplers, suspended membrane waveguides, cantilever waveguides, and photonic crystal waveguides, I achieved the monolithic integration of the entire device on a single chip. By exploiting the novel home-made air-cladding germanium platform, the device is capable of working in the IR spectral range that covers the entire fingerprint region. In addition, the transmission spectrum of the device was optimized by inducing the interference of two cavity modes to achieve the Fano resonance, which is beneficial for IR sensing applications. The demonstrated device paves a new way to realize strong on-chip light-matter interaction in the entire fingerprint region, which is applicable for integrated nonlinear optics and on-chip biochemical sensing.

3.4 High-Q photonic crystal nanobeam cavity

3.4.1 Overview

As Q factor is a crucial parameter that reflects the on-chip interaction strength between the light confined in cavities and target molecules, I managed to increase the Q factor of the photonic crystal cavity. In this part, I proposed and experimentally demonstrated a photonic crystal nanobeam cavity with a Q factor of $\sim 18,000$ and an effective mode volume of $0.18 \mu\text{m}^3$ [14]. It is worthwhile to mention that this Q factor is the highest of reported nanocavities across mid-IR germanium-based integration platforms. Such a high-Q nanocavity is achieved by a combination of experimentally feasible theoretical design, Smart-Cut methods for GOI wafer development, and optimized device fabrication processes. By virtue of its high Q value and ultrasmall mode volume, the nanocavity enables unprecedented strong light-matter interaction in the mid-IR spectral range.

3.4.2 Theoretical design

Our MIR germanium nanocavity is a photonic crystal nanobeam cavity connected to two focusing subwavelength grating couplers by suspended-membrane waveguides. The schematic diagram of the device is shown in Figure 3-8. All components are monolithically integrated on a GOI chip. The magnified central part of the device, that is, the photonic crystal nanobeam cavity, is shown in the left inset. The photonic crystal nanobeam consists of a 700-nm-wide waveguide (W) and eighteen air through-holes with varying diameters.

The sizes and spacing of the air through-holes are symmetrical across the midpoint of the nanobeam, between the ninth and tenth holes. From either end, the first four through-holes have equal diameters of 410 nm (d_1). From the fifth to the ninth through-holes, the diameters are parabolically tapered from 370 nm (d_2) to 240 nm (d_3). The distances between the first five through-holes are all 600 nm (a_1), while the distances between the fifth to tenth through-holes are parabolically tapered from 550 nm (a_2) to 480 nm (a_3). This

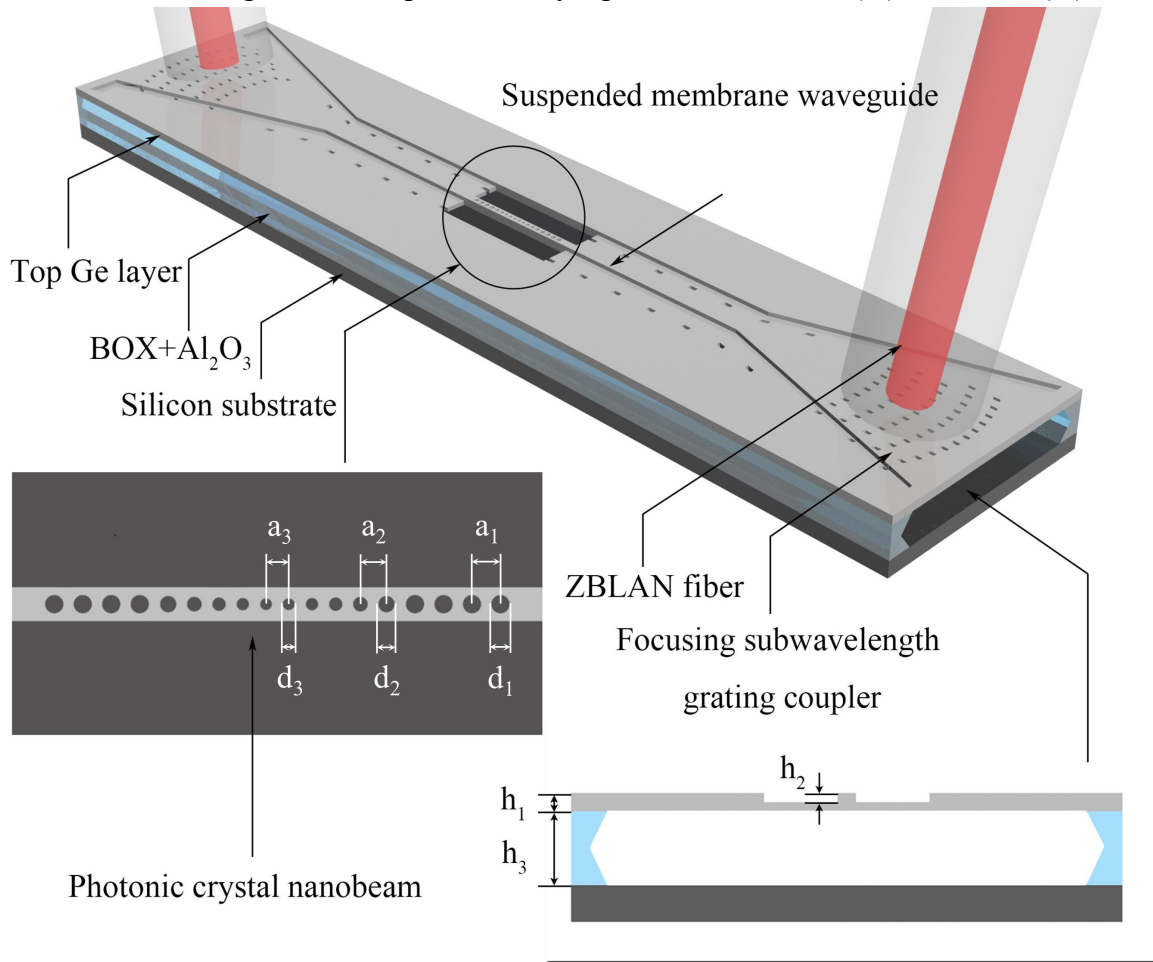


Figure 3-8. Schematic of the monolithically integrated on-chip mid-IR germanium device that contains a high-Q nanocavity, two suspended membrane waveguides, and two focusing subwavelength grating couplers. The bottom left inset shows the design of the high-Q nanocavity. The bottom right inset shows a cross-sectional view of the suspended membrane waveguide.

parabolic tapering configuration is designed to reduce radiation loss induced by impedance mismatch by providing a slowly-varying effective-refractive-index environment for the resonant mode of the nanobeam cavity. A schematic of the cross-section of the suspended

membrane waveguide is illustrated in the right inset of Figure 3-8. The waveguide, with an etching depth (h_2) of 150 nm, is fabricated in a top germanium layer (h_1) with a thickness of 300 nm. BOX and Al_2O_3 layers (h_3) with a combined thickness of 2 μm are designed to be removed by hydrofluoric acid (HF) to form an air-cladding structure. This structure provides a symmetric refractive index environment for excellent light confinement.

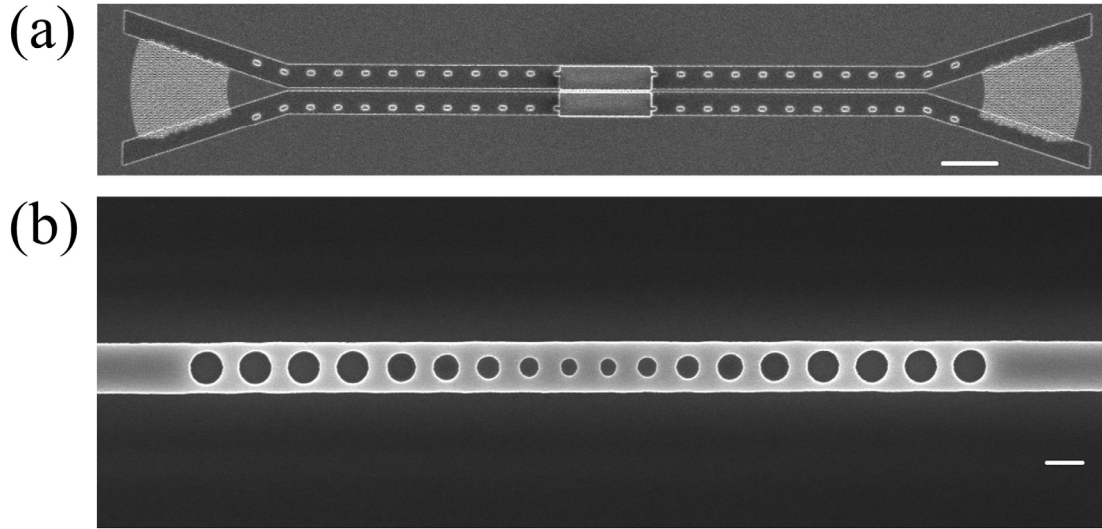


Figure 3-9. SEM images of the mid-IR germanium device, including the high-Q nanocavity. (a) Top view of the device. Scale bar: 10 μm . (b) Top view of the high-Q nanocavity. Scale bar: 500 nm.

3.4.3 Experimental fabrication

Based on the above design, we built a mid-IR high-Q germanium nanocavity. First, a high-quality GOI wafer was fabricated by using Smart-Cut methods [71]. An SiO_2 capping layer was deposited on bulk monocrystalline germanium via plasma enhanced chemical vapor deposition (PECVD), and then removed it by wet etching after H^+ ion implantation. Next, 5-nm-thick Al_2O_3 layers were deposited as bonding interfaces on the surfaces of the germanium and a pre-prepared SiO_2 -covered silicon wafer by using atomic layer deposition (ALD). After bonding the wafer, a wafer-splitting process was conducted by annealing, then polished the split germanium surface by chemical-mechanical planarization (CMP). Lastly, annealing was performed again to improve the surface quality of the GOI wafer. After the GOI wafer fabrication, I fabricated our device on the wafer by using optimized processes in two cycles. In the first cycle, I used standard electron-beam

lithography (EBL) to define the layouts of the nanocavity, grating couplers, and air holes along the suspended-membrane ridge waveguides, on a 400-nm-thick ZEP 520A resist layer pre-spincoated on the GOI chip. Then these layouts were fully etched and transferred

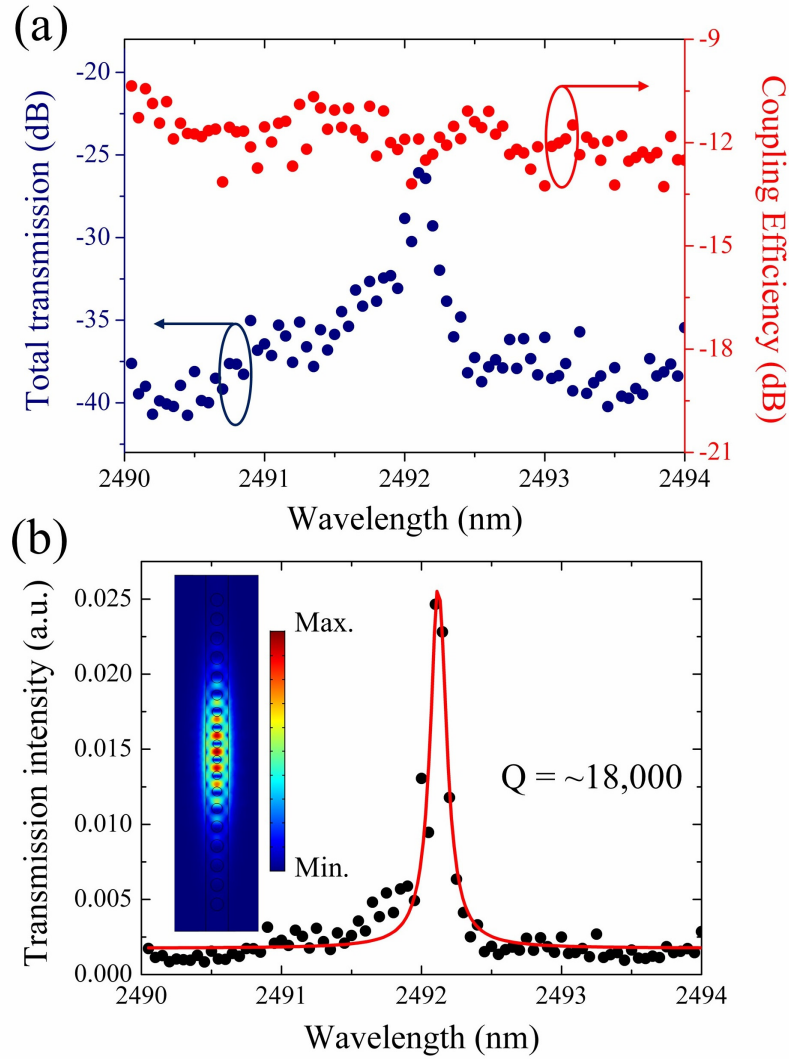


Figure 3-10. Experimental characterization of the mid-IR germanium device, including the high-Q nanocavity. (a) Measured transmission spectrum of the device (blue) and measured coupling efficiency of the focusing subwavelength grating couplers (red). (b) Lorentzian fitting of the measured nanocavity resonant mode. The inset is the electric field magnitude distribution of the resonant mode.

to the top germanium layer using a commercial inductively-coupled plasma (ICP) etcher, with a mix of CHF_3 and SF_6 gases. In the second cycle, the suspended-membrane waveguide was defined by EBL and half-etched with the ICP etcher, using CF_4 gas. Finally,

I eliminated the part of the BOX layer under the device by soaking the chip in a dilute solution of HF acid. The acid permeated through the pre-defined air holes and etched out the part of the BOX layer under the device to form the air-cladding structure. The scanning electron microscope (SEM) image of the fabricated device is shown in Figure 3-9(a) while the magnified SEM image of the central part of the device, that is, the photonic crystal nanobeam cavity, is shown in Figure 3-9(b). It is clear from the figure that the experimentally fabricated device matches well to the theoretical design.

3.4.4 Experimental characterization

After the fabrication, I measured the transmission spectrum of the nanobeam cavity in the mid-IR spectral range. A continuous-wave single-frequency Cr^{2+} : ZnS/Se laser with a tunable spectral range from 2150 nm to 2500 nm was used as the light source for the measurement. A single-mode ZrF_4 optical fiber was used to couple the light into the device through the focusing subwavelength grating coupler. Another ZrF_4 optical fiber was used to collect the out-coupled light from the focusing subwavelength grating coupler on the other end of the device. This output fiber was connected to a mid-IR optical spectral analyzer to measure the transmission spectrum of the device by continuously tuning the output wavelength of the laser. To account for the influence of the subwavelength grating coupler on the transmission spectrum of the nanobeam cavity, I first measured its coupling efficiency in the spectral range around the resonant wavelength of the nanobeam. Two focusing subwavelength grating couplers, connected by a 200 μm -long suspended-membrane waveguide, whose propagation loss is negligible, were measured. The measured coupling efficiency of the grating coupler in the spectral range of interest is about -12 dB, as shown in Figure 3-10(a). Then, I measured the total transmission spectrum of the mid-IR germanium integration platform, as shown in Figure 3-10(a). A transmission peak at a wavelength of 2492.1 nm was obtained, which corresponds to the resonant mode of the nanobeam cavity. The transmission peak exhibits some spectral asymmetry, which is a result of the photothermal effect induced by free carriers generated from two-photon absorption in germanium. Germanium has a relatively strong two-photon absorption effect at the resonant wavelength of the nanocavity. The two-photon absorption parameter β_{TPA} of germanium is $\sim 700 \text{ cm/GW}$ at the resonant wavelength, which is orders of magnitude

larger than that of silicon. To estimate the Q factor of the resonant mode, I plotted the measured resonant mode of the nanobeam cavity on a linear scale and fitted a Lorentzian lineshape to the data, as shown in Figure 3-10(b). The inset shows a theoretical simulation of the electric field magnitude distribution of the resonant mode, whose effective mode volume, defined as $\int \epsilon |E|^2 dV / (\epsilon |E|^2)_{\max}$, is $0.18 \mu\text{m}^3$. Here, ϵ and $|E|$ are the permittivity and electric-field magnitude at different positions of the nanobeam cavity, while V represents the whole volume of the nanobeam cavity. The Q factor was thus measured as $\sim 18,000$, which is the highest to date for mid-IR germanium nanocavities. The experimentally obtained Q factor was less than our theoretical design, which estimated a Q factor of $\sim 30,000$. Two possible explanations for this discrepancy are imperfections in fabrication and surface roughness from the polishing of the top germanium layer. In the future, the creation of mid-IR integrated germanium platform devices with higher Q factors can be expected, as further improvements are made in the quality of the GOI wafer and the device fabrication processes.

3.4.5 Summary

In summary, I demonstrated, for the first time, a mid-IR high-Q germanium photonic crystal nanobeam cavity on a monolithic chip. A record-setting Q factor of $\sim 18,000$ among mid-IR germanium-based nanocavities was achieved by the combination of the experimentally feasible theoretical design, Smart-Cut methods for GOI wafer development, and optimized device fabrication processes. The fabrication processes for this mid-IR germanium nanocavity are fully compatible with CMOS foundry processes, promising for low-cost and high-volume production. The suspended-membrane structure and the broad transparency window of germanium allow for applications of our device in the mid-IR spectral range. Taking advantages of its high Q factor and ultrasmall mode volume, the nanocavity opens new avenues towards applications in on-chip sensing, spectroscopy, nonlinear optics, optomechanics, and quantum information processing in the mid-IR spectral range.

3.5 High-Q microring resonator

3.5.1 Overview

To further increase the Q factor of the fabricated on-chip germanium resonator and make use of the broad infrared spectral range, I experimentally demonstrated a mid-IR suspended-membrane germanium microring resonator [15]. A loaded Q factor of $\sim 57,000$ and an extinction ratio (ER) of 22 dB were experimentally demonstrated, which corresponds to a propagation loss of 5.4 dB/cm. This Q factor is not only the highest of mid-IR germanium microring resonators, but also the highest of all previously reported air-cladding microring resonators, across all mid-IR integration platforms. Such a high Q factor was achieved by employing our Smart-Cut methods, for developing high-quality GOI wafers, and by implementing a suspended-membrane structure, to reduce radiation loss. The high-Q germanium microring resonator is expected to enable diverse on-chip applications in sensing, spectroscopy, and nonlinear optics over a wide mid-IR spectral range, which is expected to boost development of mid-IR germanium photonics.

3.5.2 Theoretical design

Our mid-IR germanium device is a microring resonator coupled with a suspended-membrane waveguide that connects two focusing grating couplers. The design of our device is schematically illustrated in Figure 3-11(a). All the components of the device were monolithically integrated on a single GOI chip. The radius (r) of the microring was designed to be 35 μm . The magnified coupling area of the microring and the waveguide is shown in Figure 3-11(b). The waveguide width (W_1) and the microring width (W_2) are both 900 nm to satisfy fundamental mode conditions. To approach the critical coupling, the minimum gap between the waveguide and the microring was designed to be 140 nm to 200 nm, which corresponds to a power cross-coupling efficiency between the waveguide and the microring ranging from 1% to 3%. Two rows of air holes were designed to allow hydrofluoric acid (HF) to access and etch out the part of the BOX layer under the device, in order to realize the suspended-membrane structure. A schematic of the cross-section of the suspended-membrane waveguide is shown in Figure 3-11(c). The waveguide is a rib waveguide with an etching depth (h_2) of 150 nm, fabricated in a top germanium layer with a thickness (h_1) of 300 nm, such that the waveguide can be well supported by two-side

cantilevers. The thickness (h_3) of the BOX layer between the top germanium layer and a silicon substrate was 2 μm . The part of the BOX layer under the waveguide was designed to be etched out by the HF to form a suspended-membrane structure, which increases refractive index contrast between the top germanium layer and the cladding layer, resulting in better mode confinement and a more compact device footprint. Moreover, the suspended-membrane structure creates a symmetric refractive index environment for propagation modes in the waveguide and the microring. This reduces the radiation loss

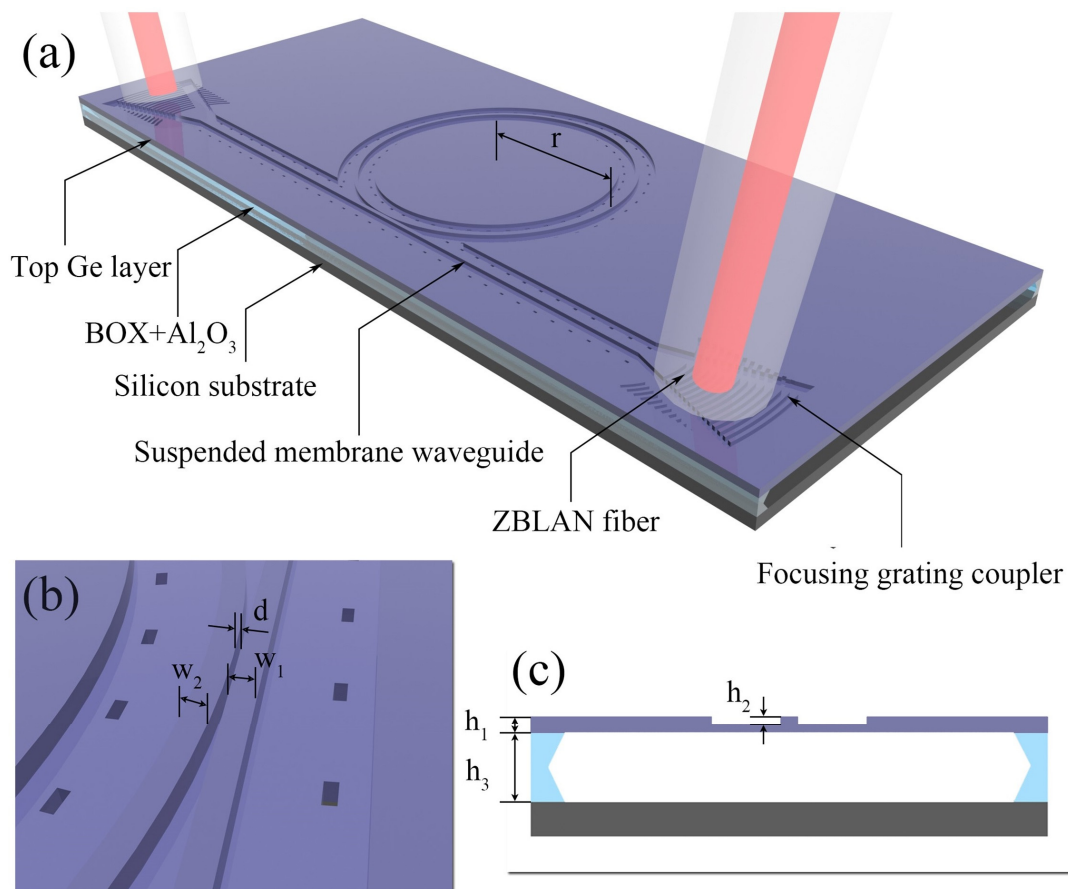


Figure 3-11. Schematic of the monolithically integrated on-chip mid-IR germanium device that contains a high-Q microring resonator, a suspended-membrane waveguide, and two focusing grating couplers. (a) Three-dimensional view of the device. (b) Coupling area between the microring resonator and waveguide. (c) Cross-sectional view of the suspended-membrane waveguide.

induced by asymmetric refractive index environments, such as those in the conventional integration platforms like germanium-on-silicon, germanium-on-SOI, or germanium-on-Si₃N₄.

3.5.3 Experimental fabrication

According to the design above, I experimentally fabricated our mid-IR high-Q germanium microring resonator. First, a high-quality GOI wafer was fabricated by using Smart-Cut methods [71], the work flow of which is as follows. An SiO₂ capping layer was first deposited on bulk monocrystalline germanium, as a protection layer for H⁺ ion implantation via plasma enhanced chemical vapor deposition (PECVD). After the H⁺ ion implantation, the SiO₂ capping layer was removed by wet etching, and two 5-nm-thick Al₂O₃ layers, as bonding interfaces, were deposited on the surfaces of the germanium and an SiO₂-covered silicon wafer by using atomic layer deposition (ALD). Then, the germanium and the SiO₂-covered silicon wafer were manually bonded. Annealing was

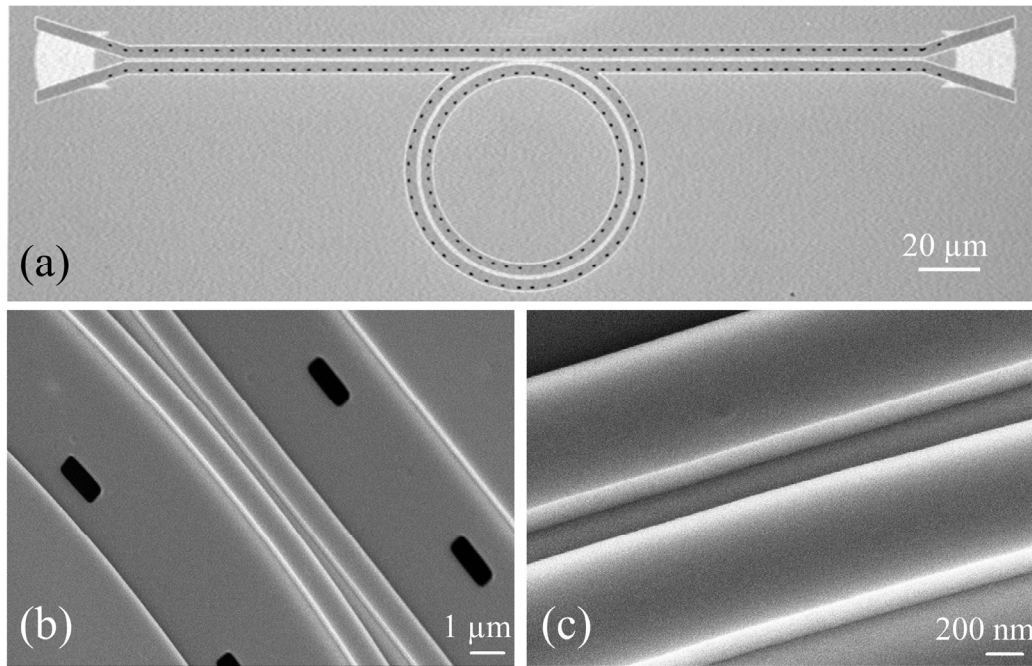


Figure 3-12. SEM images of the mid-IR germanium device, including the high-Q microring resonator. (a) Top view of the device. Scale bar: 20 μm. (b) Coupling area between the high-Q microring resonator and the waveguide. Scale bar: 1 μm. (c) Zoom-in view of the coupling area which indicates the sidewalls of the fabricated high-Q microring resonator and the waveguide are smooth. Scale bar: 200 nm.

done to split the top germanium layer, after the wafer bonding process. Next, chemical-mechanical planarization (CMP) was used to polish the split germanium surface. Finally, additional annealing was performed again to improve the quality of the top germanium layer. The Smart-Cut methods circumvent a common problem in germanium-on-silicon

and germanium-on-SOI wafer development: the lattice mismatch induced by epitaxial growth between the top germanium layer and the substrate layer. Thus, our fabrication technique ensures a high-quality germanium layer. After the wafer fabrication, I fabricated our device on the wafer in two cycles. In the first cycle, I defined the layout of the air holes along the waveguide and microring by using standard electron-beam lithography (EBL). Then, the layout was fully etched and transferred to the top germanium layer by using an inductively-coupled plasma (ICP) etcher, with a mix of CHF_3 and SF_6 gases. In the second cycle, the microring, suspended-membrane waveguide, and focusing grating couplers were defined by EBL and half-etched with the ICP etcher, using CF_4 gas. Finally, to form the

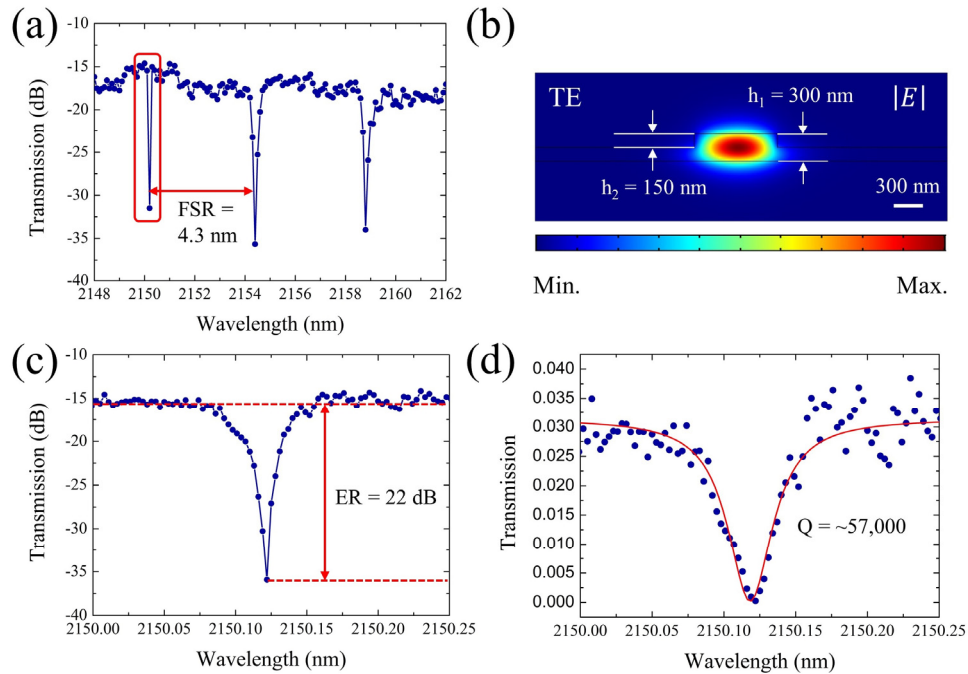


Figure 3-13. Characterization of the MIR germanium device, including the high-Q microring resonator. (a) Measured free spectral range of the microring resonator. (b) Distribution of the electric field magnitude $|E|$ of the microring resonator's quasi-TE mode. (c) ER of the microring resonator. (d) Q factor of the microring resonator.

suspended-membrane structure I eliminated the part of the BOX layer under the device by soaking the chip in a dilute solution of HF acid. The suspended-membrane structure not only creates a symmetric refractive index environment for reduction of radiation loss, but also is expected to expand the spectral bandwidth of the device to the entire transparency window of germanium (2 - 15 μm). The scanning electron microscope (SEM) image of the

entire device is shown in Figure 3-12(a) while two magnified SEM images of the coupling area between the microring and waveguide are shown in Figure 3-12(b) and Figure 3-12(c). It can be observed from the figures that the experimentally fabricated device matches our design well. The smooth and vertical side walls of the device indicate a high quality of fabrication.

3.5.4 Experimental characterization

After the fabrication, we characterized the performance of the microring resonator in the MIR spectral range. We used a continuous-wave $\text{Cr}^{2+}:\text{ZnS/Se}$ laser, with a tunable spectral range from 2150 nm to 2500 nm, as the light source for the measurement. Two single-mode ZrF_4 optical fibers were used to couple the light into and out of the device to measure its transmission spectra. The focusing grating coupler was designed for transverse electric (TE) mode coupling. The transmission spectra were measured by an optical spectral analyzer via continuously tuning the output wavelength of the laser. There is no measurable noise resulting from the vibration of the suspended membrane structure. The transmission spectrum of the device over the spectral range from 2148 nm to 2166 nm is shown in Figure 3-13(a). In this spectral range, three continuous transmission dips were obtained, which correspond to three adjacent resonant quasi-TE modes of the microring resonator. The distribution of the electric field magnitude $|E|$ of the microring resonator's quasi-TE mode at the wavelength around 2510 nm was simulated and illustrated in Figure 3-13(b). The confinement factors of the quasi-TE mode above, within, and beneath the waveguide are 7.0%, 85.9%, and 7.1%, respectively. The calculated effective index of the quasi-TE mode is 3.25. Based on the transmission spectrum, the FSR of the microring resonator was measured to be 4.3 nm. The ER of the resonant mode at the wavelength of 2150.12 nm was about 22 dB, as shown in Figure 3-13(c). Such a high ER value indicates that an almost perfect destructive interference is realized between the light coupled out from the microring and the light transmitted through the waveguide at the resonant wavelength, which is close to the critical coupling condition. To further evaluate the Q factor of this resonant mode, we plotted the measured resonant mode on a linear scale and fitted a Lorentzian lineshape to the data. The result is shown in Figure 3-13(d). From the fit, it is evident that a loaded Q factor as high as $\sim 57,000$ was experimentally achieved. Based on

the above experimental data and the formalism in [29], the group index of our microring resonator is calculated to be 4.89. As the resonant mode is close to the critical coupling condition, the amplitude self-coupling coefficient equals the single-pass amplitude transmission of the microring resonator, which are both experimentally extracted to be 98.6%. Thus, the power cross-coupling efficiency between the waveguide and the microring is 2.7%. The propagation loss of the microring resonator is also experimentally extracted to be 5.4 dB/cm. Moreover, since the resonant mode is close to the critical coupling condition, the intrinsic Q factor of the microring resonator is calculated to be $\sim 114,000$. In the future, with further improvement in device fabrication processes, realization of MIR germanium resonators with even higher Q factors can be expected by virtue of the Smart-Cut methods for wafer development and a suspended-membrane structure for reduction of radiation loss.

3.5.5 Summary

In summary, I experimentally demonstrated a suspended-membrane mid-IR germanium high-Q microring resonator coupled with a waveguide on a monolithic chip. A loaded Q factor of $\sim 57,000$, the highest to date of all reported mid-IR germanium microring resonators, was achieved experimentally with a high ER of 22 dB. The high-Q microring resonator was made possible by using the Smart-Cut methods for the development of high-quality wafers and by employing a suspended structure that reduces radiation loss. The suspended structure also expands the spectral bandwidth of the resonator to the whole fingerprint spectral range. The resonator is compatible with high-yield nanofabrication based on mature CMOS processing technologies, which can translate to low-cost mid-IR devices. The high-Q germanium microring resonator opens new doors for the production of other novel mid-IR devices and their applications in mid-IR on-chip sensing, spectroscopy, and nonlinear optics. The device is expected to boost the development of mid-IR germanium photonics.

3.6 Conclusion

In this Chapter, I present three types of high-Q resonators based on the suspended-membrane germanium integration platform. With the optimization of device designs and fabrication recipes, the Q factors of the fabricated devices were increased from ~ 200 to

~18,000, and finally to ~57,000. A comparison of recently reported germanium resonators in the community is shown in Figure 3-14 [14-16, 38, 67, 72, 73]. In my doctoral work, I demonstrated the mid-IR germanium resonator with the highest Q factor and the mid-IR germanium nanocavity with the highest Q factor. As the Q factor indicates the strength of on-chip light-matter interaction, highly-sensitive infrared spectroscopy that includes the fingerprint region can be expected by using the demonstrated high-Q germanium photonic devices. With further improvement of the wafer quality and fabrication techniques, infrared germanium photonic devices with Q factors comparable to those of silicon and silicon nitride counterparts can be expected in the future.

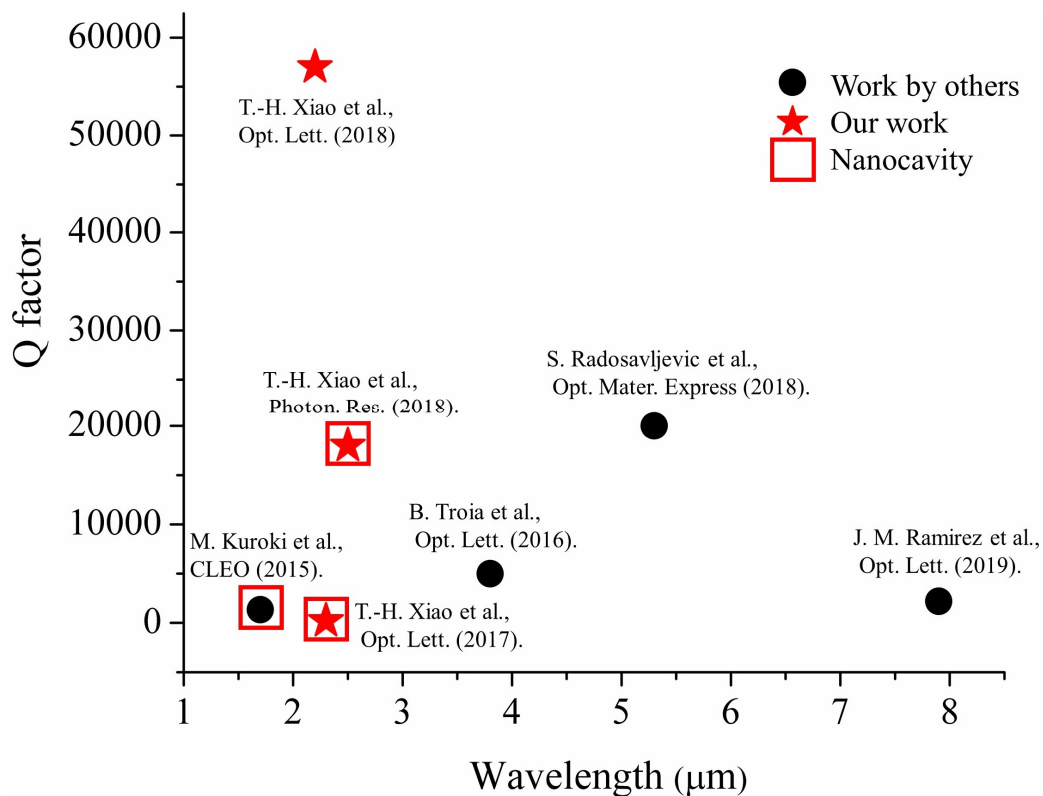


Figure 3-14. Comparison of recently reported germanium resonators. The mid-IR germanium resonator with the highest Q factor and the mid-IR germanium nanocavity with the highest Q factor were demonstrated in my doctoral work.

Chapter 4

Demonstration of on-chip silicon photonic devices for Raman spectroscopy

4.1 Introduction

Silicon is selected for developing on-chip photonic devices for Raman spectroscopy as it is not only cost-effective for high-volume production [74, 75], but also possesses a high refractive index for realizing strong light-matter interaction on a chip by structural resonance. Compared with conventional metallic integration platforms for surface enhanced Raman spectroscopy, silicon platforms take advantages of high energy efficiency and small photothermal heat generation, which prevents detected samples from being destroyed by the thermal effect [76].

To demonstrate the promising capability of on-chip silicon photonic devices for Raman spectroscopy, I theoretically designed and experimentally fabricated two types of on-chip silicon nanostructures for highly-sensitive Raman optical activity (ROA). One type is a chiral nanostructure while the other type is an achiral nanostructure. The chiral nanostructure is a spiral nanoflower with giant optical activity [64]. A largest-to-date circular intensity difference (CID) of 35% was experimentally realized by using the nanoflower. The achiral nanostructure is a silicon nanodisk array that enables an enhancement factor of $\sim 10^2$ for ROA in the near-field region. The details of theoretical design, experimental fabrication, and experimental characterization of these silicon photonic devices with controllable structural resonance will be introduced in this Chapter.

4.2 Spiral nanoflower with giant optical activity

4.2.1 Introduction

Chirality is a symmetric property of molecules that determines the physical, chemical, and biological characteristics of matter on a wide range of size scales, ranging from bulk crystals, to nanomaterials, and to biomolecules [77-79]. The chirality of molecules is

typically probed and quantified by their optical activity (also called the chiroptical effect), which is the ability of chiral molecules to selectively interact with left or right circularly polarized (LCP or RCP) light [80, 81]. However, the optical activity of natural molecules is intrinsically very weak [82]. Realization of large optical activity is, therefore, desirable not only for understanding the evolution of chiral molecules which is intrinsically linked to the origin of life in astrobiology [83], but also for enabling the development of diverse chiroptical devices and applications in stereochemistry [84], analytical chemistry [85], metamaterials [86], and spin photonics [87]. To this end, various efforts have been made toward the development of artificial structures with large optical activity in the last decade [88, 89].

The exploitation of metallic nanostructures as basic elements has been proposed and demonstrated to realize large optical activity by inducing surface plasmon resonance (SPR) on the nanostructures [90-95]. The excitation of SPR, which is the resonant oscillations of free electrons in metals coupled with the incident electromagnetic field, results in the strong concentration of the electric field in the near-field region of the nanostructures [96] and hence an increased interaction between the nanostructures and incident circularly polarized light [97]. Although a variety of plasmonic configurations have been developed to achieve large optical activity, such as helical propellers [93], spirals [98], scaffolds [91], supramolecular structures [99], multilayer coupling structures [88], and pseudo chiral structures [100], the intrinsic high ohmic loss of the metallic materials further amplified by the SPR results in low energy efficiency and large photothermal heat generation [60, 76], severely limiting the performance and practical utility of such nanostructures.

Dielectrics provide a promising solution to the above issue by taking advantage of their intrinsically low ohmic loss. Mie resonance in high-refractive-index dielectrics has recently been explored as a counterpart of SPR on metals to enhance the optical near-field on micrometer to nanometer scales [60]. In fact, several all-dielectric nanostructures have been investigated, such as nanospheres [101], nanodisks [102], dimers [103], and oligomers [104], while several applications of the nanostructures have also been demonstrated, such as electromagnetically induced transparency [105], harmonic generation [106], and surface enhanced spectroscopy [76]. However, the field enhancement on such all-dielectric nanostructures in similar geometric configurations to

the metal nanostructures is much weaker than that of metallic nanostructures. Therefore, realization of all-dielectric nanostructures with large optical activity remains challenging.

In this part, I present giant optical activity by inducing magnetic resonance in a silicon spiral nanoflower (spiral-flower-shaped nanostructure). Specifically, I theoretically analyzed the physical origin of the giant optical activity in the nanostructure by conducting numerical simulation and multipole expansion analysis and experimentally demonstrated the largest-to-date CID of $\sim 35\%$ (even compared with SPR-enhanced metallic nanostructures [89]) by optimizing the magnetic quadrupole contribution of the nanoflower to scattered light. The manipulation of magnetic quadrupole interference enabled the realization of giant optical activity by a quasi-two-dimensional planar nanostructure, which does not require complex three-dimensional fabrication techniques [91] and can be conveniently implemented for various applications. Moreover, all the fabrication steps of the nanoflower are CMOS-compatible and are hence applicable for integration with other on-chip devices as well as high-volume production. The nanoflower overcomes the bottleneck of the traditional metallic platforms and is expected to pave the way toward the development of diverse chiroptical devices and applications. One of them, for example, is an on-chip high-sensitivity chiral sensor with small photothermal heat generation applicable in the fields of chemical synthesis, catalysis, pharmaceuticals, and biomedicine that require highly stable temperature control.

4.2.2 Theoretical design

The concept of realizing giant optical activity by an all-dielectric spiral nanoflower is schematically illustrated in Figure 4-1. A beam of LCP or RCP light normally impinges on a nanoflower on a silica substrate. The scattered light, which reflects the interaction between the incident light and the nanoflower, is gleaned to quantify the optical activity. As I focus on the optical activity of individual nanoflowers, I assemble the nanoflowers into a square-lattice array with a large period of $5\ \mu\text{m}$ to increase the signal-to-noise ratio of the scattering spectrum measurement, but to avoid the coupling between the adjacent nanoflowers. The specific geometric parameters of the nanoflower are shown in the inset of Figure 4-1. The nanoflower consists of one circular nanocylinder at the center surrounded by six elliptic nanocylinders with continuously varying orientations. The radius

of the central nanocylinder, r , is 187 nm while the diameters of the major axis and minor axis of the surrounding elliptic nanocylinders, a and b , are 425 nm and 125 nm, respectively. All the nanocylinders share an equal height, h , of 340 nm. The distance, d , from the center of the circular nanocylinder to the vertex of each elliptic nanocylinder is 250 nm.

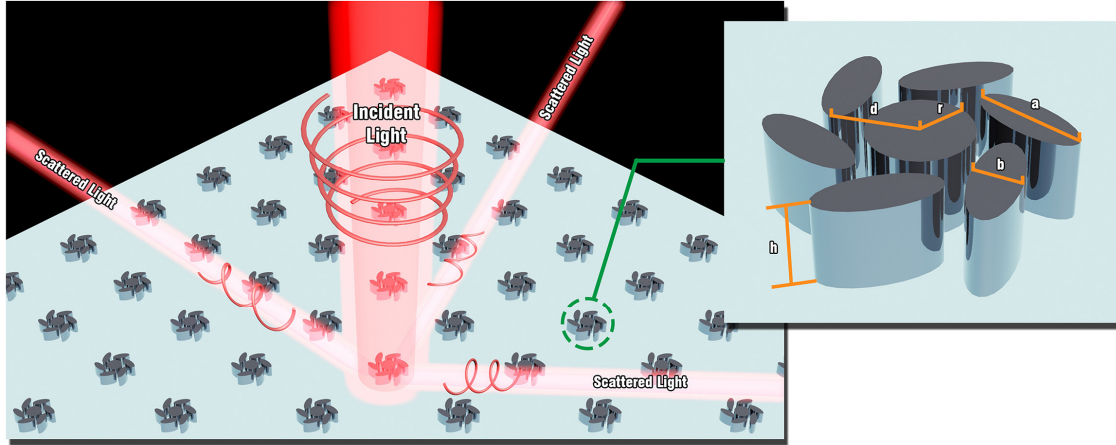


Figure 4-1. Concept of giant optical activity in an all-dielectric spiral nanoflower. A beam of left or right circularly polarized (LCP or RCP) light normally impinges on a nanoflower on a silica substrate. Scattered light, which reflects the interaction between the incident light and the nanoflower, is gleaned to quantify the optical activity of the nanoflower. The inset shows the geometric parameters of the nanoflower. $a = 425$ nm, $b = 125$ nm, $r = 187$ nm, $d = 250$ nm, and $h = 340$ nm.

Based on the above concept and design, I first investigated the optical activity of our designed spiral nanoflower by numerical simulation. The simulation was conducted by using a commercial finite-element-method (FEM) software kit (COMSOL Multiphysics) in two steps. First, I calculated a background field that includes the influence of the substrate for both incident RCP and LCP light in the spectral range from 740 nm to 800 nm. The incident RCP and LCP light were defined by introducing a 90° or -90° phase shift between the x-component and y-component of the electric field via port boundary conditions. Period boundary conditions were used to define an area as large as the unit cell of the silicon nanoflower array. A 1- μm -thick air layer was defined on a 2- μm -thick buried oxide layer on a silicon substrate. The refractive indices of the air layer and the buried oxide layer were set to be 1.0 and 1.45, respectively. The refractive index of the silicon used in the simulation came from a report by Aspnes and Studna [107]. Second, after the calculation of the background field, I added the nanoflower model to the model and

covered the calculation space by perfect matched layers. Then, the background field acquired in the last step was used to calculate the near-field distributions of the nanoflower and the scattered light to the far-field. By integrating the scattered light over a closed surface enclosing the nanoflower at different wavelengths, the scattering spectra were obtained.

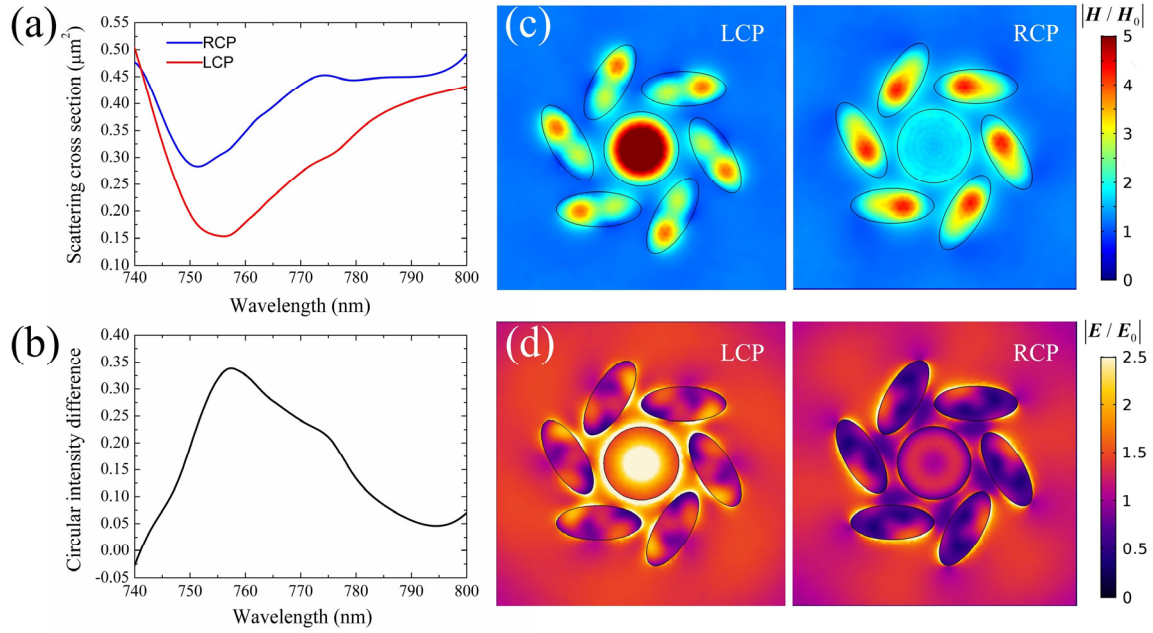


Figure 4-2. Theoretical analysis of the optical activity of the nanoflower. (a) Scattering cross-section of the nanoflower. (b) Circular intensity difference (CID) of the nanoflower. (c) Normalized magnetic near-field strength of the incident LCP and RCP light at the wavelength where the CID is peaked. (d) Normalized electric near-field strength of the incident LCP and RCP light at the wavelength where the CID is peaked.

The calculated scattering cross-sections of the nanoflower with the incident RCP and LCP light (blue and red curves) are shown in Figure 4-2(a). A distinct difference in the scattering cross-sections excited by the incident light with the opposite chirality is observed in the spectral range from 740 nm to 800 nm. Both the scattering spectra display valley lineshapes, but with different valley depths in the spectral range. This is due to the intrinsic chirality of the nanoflower that results in the different interaction with the incident light. In order to quantify such a difference, namely, optical activity, the CID was calculated via utilizing the scattering spectra in Figure 4-2(a) and shown in Figure 4-2(b). The CID is a commonly used parameter to characterize the optical rotation or optical

activity of chiral molecules in molecular spectroscopy. As a single nanoflower can be considered as a metamolecule, the CID is employed to characterize its optical activity. The CID is defined as $(I_{\text{RCP}} - I_{\text{LCP}}) / (I_{\text{RCP}} + I_{\text{LCP}})$, where I_{RCP} and I_{LCP} are the scattering intensities of the nanoflower excited by the incident RCP and LCP light, respectively. The peak of the CID spectrum is located at a wavelength of 757 nm with a CID value as high as ~35%, indicating the realization of giant optical activity.

To understand the underlying physics of the giant optical activity, I calculated the magnetic field and electric field distributions excited by the incident RCP and LCP light at the wavelength of the CID peak. The magnitude distributions of the magnetic field and electric field normalized to the incident light field on the surface of the nanoflower are illustrated in Figure 4-2(c) and Figure 4-2(d), respectively. An obvious difference in the magnetic field distributions excited by the incident light with the opposite chirality is observed in Figure 4-2(c). For the LCP excitation, the magnetic-field-enhanced regions induced by the magnetic resonance within the nanoflower mainly are localized in the central nanocylinder and the outer ends of the surrounding nanocylinders, while for the RCP excitation, the magnetic-field-enhanced regions are localized in the inner ends of the surrounding nanocylinders. The different magnetic resonance within the nanoflower leads to the different contributions to the scattering spectra. On the other hand, the electric field distributions of the nanoflower also strongly depend on the optical chirality of the incident light as shown in Figure 4-2(d). The hot spot regions of electric field are concentrated in the central part of the nanoflower for the LCP excitation while in the peripheral part for the RCP excitation. Higher-order modes are excited within the nanoflower, which can be judged from the field patterns. Moreover, it is worthwhile to note that the enhancement of the magnetic field is higher than that of the electric field on the surface of the nanoflower at the peak wavelength. This indicates the domination of magnetic resonance. However, since it is not easy to clarify the difference of scattering spectra induced by the complex interference of the excited modes directly from the field distributions, a multipole analysis of the far field that determines the scattering spectra of the nanoflower is essential.

The three-dimensional field distributions of the nanoflower at the wavelength where the CID is peaked are calculated and shown in Figure 4-3. It can be observed that the high-order modes are excited within the nanoflower. The distributions of both the normalized

magnetic near-field strength and normalized electric near-field strength demonstrate the same rotational symmetry as that of the geometric configuration. The major difference between the magnetic and electric field distributions of the nanoflower excited by the incident LCP and RCP light indicates the different excitation of magnetic and electric multipoles within the nanoflower.

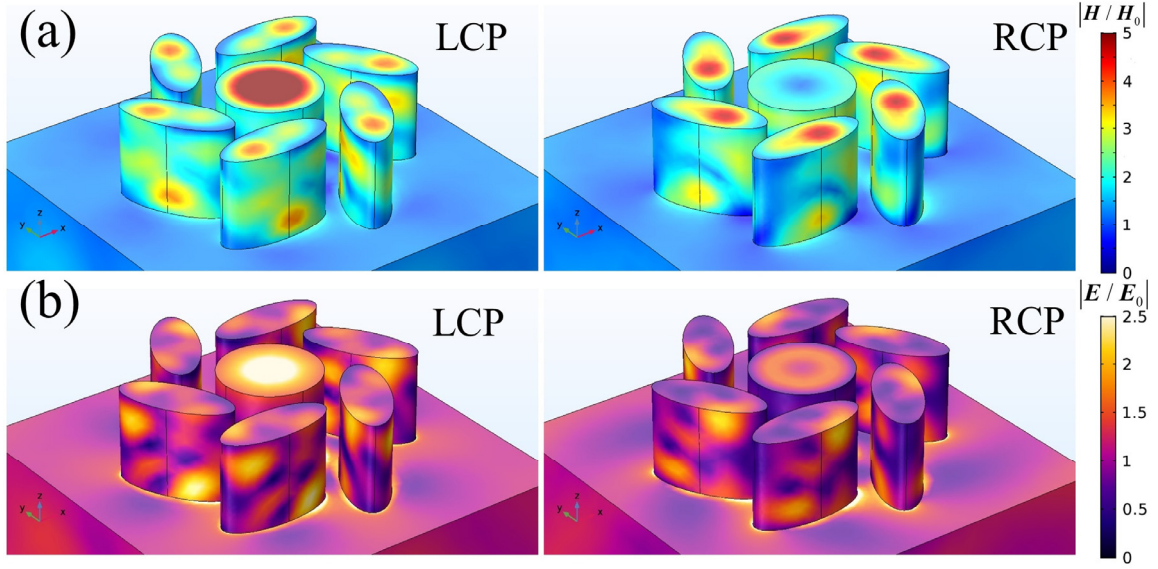


Figure 4-3. Three-dimensional field distributions of the nanoflower. (a) Normalized magnetic near-field strength. (b) Normalized electric near-field strength.

To further investigate the physical origin of the giant optical activity, I analyzed the scattering spectra of the nanoflower excited by the incident light with the opposite chirality by multipole expansion method. The multipole expansion analysis used in the main text is based on a numerical method. By utilizing the full field of the nanoflower calculated by the FEM method and introducing the concept of scattering current density, the expansion coefficients that quantify the different multipole contributions to the scattered light are solved numerically. The specific steps are as follows. According to the electromagnetic theory, the scattered electromagnetic field can be expressed in spherical coordinates as [ref]

$$\begin{aligned} \mathbf{E}_s(r, \theta, \phi) = E_0 \sum_{l=1}^{\infty} \sum_{m=-l}^l i^l [\pi(2l+1)]^{1/2} \left\{ \frac{1}{k} a_E(l, m) \nabla \times \left[h_l^{(1)}(kr) \mathbf{X}_{lm}(\theta, \phi) \right] + \right. \\ \left. a_M(l, m) h_l^{(1)}(kr) \mathbf{X}_{lm}(\theta, \phi) \right\}, \end{aligned} \quad (4-1)$$

$$\mathbf{H}_s(r, \theta, \phi) = \frac{E_0}{\eta} \sum_{l=1}^{\infty} \sum_{m=-l}^l i^{l-1} [\pi(2l+1)]^{1/2} \left\{ \frac{1}{k} a_M(l, m) \nabla \times [h_l^{(1)}(kr) \mathbf{X}_{lm}(\theta, \phi)] + a_E(l, m) h_l^{(1)}(kr) \mathbf{X}_{lm}(\theta, \phi) \right\}, \quad (4-2)$$

where \mathbf{X}_{lm} and $h_l^{(1)}$ are the normalized vector spherical harmonics and the spherical Hankel functions of the first kind while E_0 , k , and η are the electric field magnitude of incident light, the wave vector in the background medium, and the impedance of the background medium. $a_E(l, m)$ and $a_M(l, m)$ are the expansion coefficients of the electric multipole and magnetic multipole, in which the integer l determines the order of the multipole. For example, for the dipole and quadrupole, l equals 1 and 2, respectively. By making using the orthogonality of the vector spherical harmonics \mathbf{X}_{lm} and the scalar spherical harmonics Y_{lm} , the expansion coefficients can be written as

$$a_E(l, m) = \frac{(-i)^{l+1} kr}{h_l^{(1)}(kr) E_0 [\pi(2l+1)l(l+1)]^{1/2}} \int_0^{2\pi} \int_0^\pi Y_{lm}^*(\theta, \phi) \hat{\mathbf{r}} \cdot \mathbf{E}_s(\mathbf{r}) \sin\theta d\theta d\phi, \quad (4-3)$$

$$a_M(l, m) = \frac{(-i)^l kr}{h_l^{(1)}(kr) E_0 [\pi(2l+1)l(l+1)]^{1/2}} \int_0^{2\pi} \int_0^\pi Y_{lm}^*(\theta, \phi) \hat{\mathbf{r}} \cdot \mathbf{H}_s(\mathbf{r}) \sin\theta d\theta d\phi, \quad (4-4)$$

where \mathbf{r} is the position vector. Then, we introduce the concept of scattering current density [ref]

$$\mathbf{J}_s(\mathbf{r}) = -i\omega \varepsilon_0 (\varepsilon_r(\mathbf{r}) - \varepsilon_m) \mathbf{E}(\mathbf{r}), \quad (4-5)$$

where ω is the angular frequency, ε_0 is the permittivity of vacuum, $\varepsilon_r(\mathbf{r})$ is the relative permittivity at \mathbf{r} , ε_m is the relative permittivity of the background medium, and $\mathbf{E}(\mathbf{r})$ is the total electric field at \mathbf{r} . The total electric field $\mathbf{E}(\mathbf{r})$ in the whole space can be calculated by the FEM method in advance. By further utilizing the Maxwell equations, the expansion coefficients can be rewritten as

$$a_E(l, m) = \frac{(-i)^{l-1} k \eta}{E_0 [\pi(2l+1)l(l+1)]^{1/2}} \int Y_{lm}^*(\theta, \phi) j_1(kr) \times \left\{ k^2 \mathbf{r} \cdot \mathbf{J}_s(\mathbf{r}) + \left(2 + r \frac{d}{dr} \right) [\nabla \cdot \mathbf{J}_s(\mathbf{r})] \right\} d^3r, \quad (4-6)$$

$$a_M(l, m) = \frac{(-i)^{l-1} k^2 \eta}{E_0 [\pi(2l+1)l(l+1)]^{1/2}} \int Y_{lm}^*(\theta, \phi) j_1(kr) \mathbf{r} \cdot [\nabla \cdot \mathbf{J}_s(\mathbf{r})] d^3r, \quad (4-7)$$

where $j_1(kr)$ is the spherical Bessel function. Based on Eq. (6) and Eq. (7), the multipole contributions can be calculated numerically.

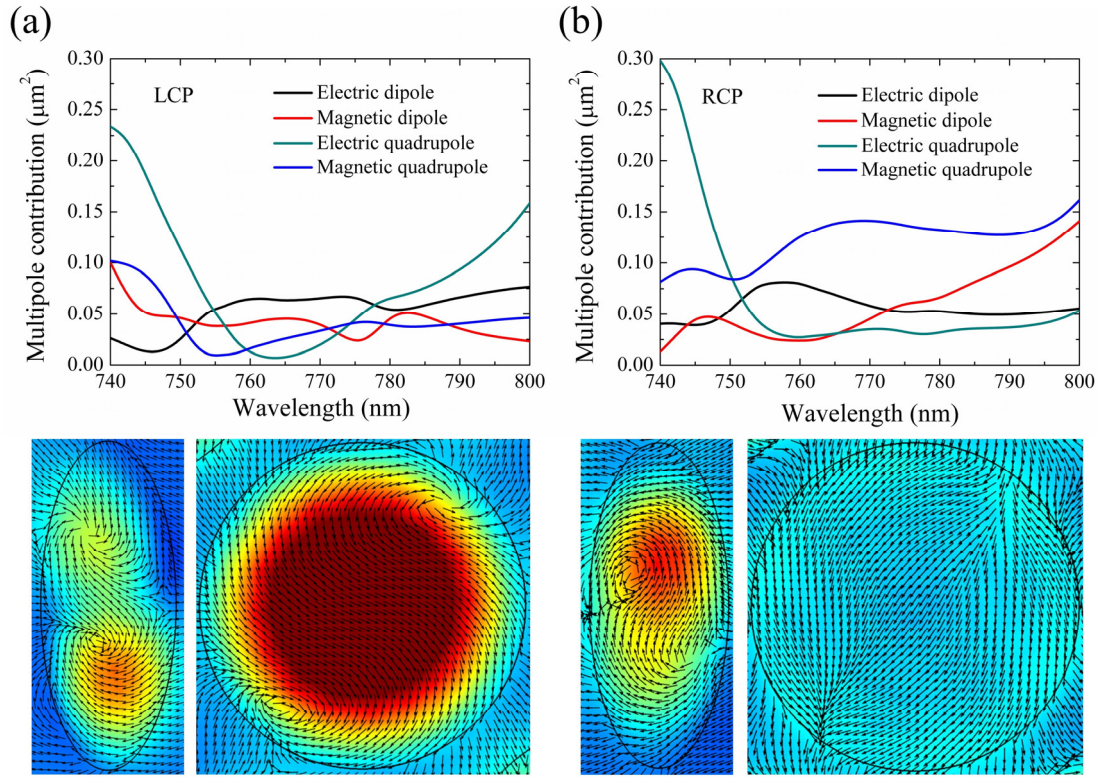


Figure 4-4. Theoretical analysis of the optical activity of the nanoflower. (a) Scattering cross-section of the nanoflower. (b) Circular intensity difference (CID) of the nanoflower. (c) Normalized magnetic near-field strength of the incident LCP and RCP light at the wavelength where the CID is peaked. (d) Normalized electric near-field strength of the incident LCP and RCP light at the wavelength where the CID is peaked.

The results of the multipole expansion that include the first four-order multipoles are illustrated in Figure 4-4(a) and Figure 4-4(b), respectively. At the wavelength of the giant optical activity, that is, the wavelength of the CID peak, the four multipole contributions to the scattering spectrum excited by the incident LCP light are compared with those excited by the incident RCP light accordingly. The magnetic quadrupole contribution difference of $0.11 \mu\text{m}^2$, which takes up about 70% of the total scattering cross-sectional difference, was identified. This illustrates that the giant optical activity mainly originates from the magnetic quadrupole contributions. To further verify this point, we calculated the normalized transverse electric field directions and plotted them as shown as black arrows in the insets of Figure 4-4(a) and Figure 4-4(b). As for the LCP incidence, two electric field vortices with opposite directions are observed on the top surface of both the central and

surrounding nanocylinders. This indicates the excitation of magnetic quadrupole resonance within both the central and surrounding nanocylinders. Due to the destructive interference of the magnetic quadrupole scattering between the central nanocylinder and the surrounding nanocylinders, the total contribution from the magnetic quadrupole is suppressed as shown in Figure 4-4(a). The suppression of the scattering increases the optical energy confined within the nanoflower, giving rise to a stronger near-field enhancement as shown in Figure 4-3. In comparison, two electric field vortices with opposite directions were only observed on the top surface of the surrounding nanocylinder for the RCP incidence, which means the excitation of magnetic quadrupole within the central nanocylinder is much weaker than that of the incident LCP light. Thus, the destructive interference is not as strong as that of the incident LCP light while the magnetic quadrupole has a large contribution to the scattering spectrum as illustrated in Figure 4-4 (b). In general, the magnetic quadrupole excitation manipulated by the interference effect within the nanoflower plays a key role in realizing the giant optical activity.

The distributions of magnetic field component H_z excited by the incident LCP and RCP light at the wavelength where the CID is peaked are also calculated and shown in Figure 4-5. The magnetic fields in the blue and red regions have the opposite directions along the z axis. The field distributions indicate the excitation and domination of the magnetic quadrupole within both the central nanocylinder and the surrounding nanocylinders. The magnetic quadrupole within the central nanocylinder excited by the incident LCP light is much stronger than that excited by the incident RCP light, which is consistent with the theoretical analysis above.

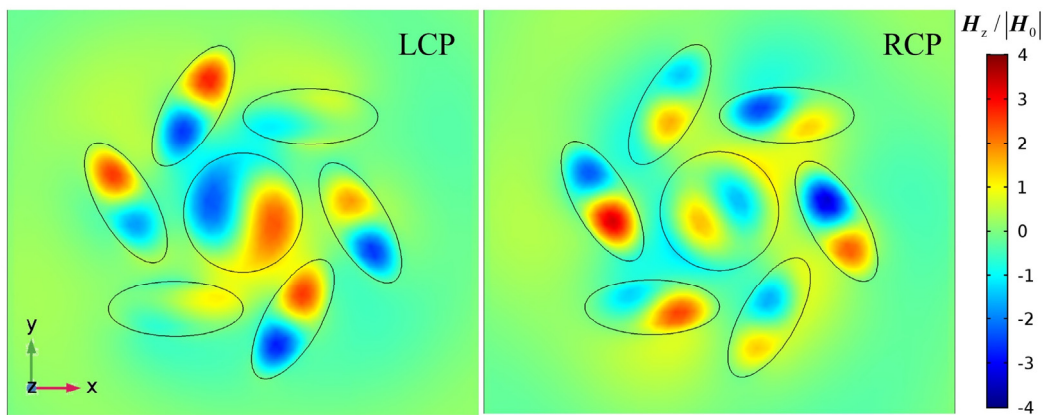


Figure 4-5. Distributions of the magnetic field component H_z excited by the incident LCP and RCP light.

In comparison with the scattering spectra and the CID of the nanoflower, the absorption spectra and the normalized circular dichroism of the nanoflower are also simulated and shown in Figure 4-6. The normalized circular dichroism is defined as $(A_{\text{RCP}} - A_{\text{LCP}}) / (A_{\text{RCP}} + A_{\text{LCP}})$, where A_{RCP} and A_{LCP} are the absorption intensities of the nanoflower excited by the incident RCP and LCP light, respectively.

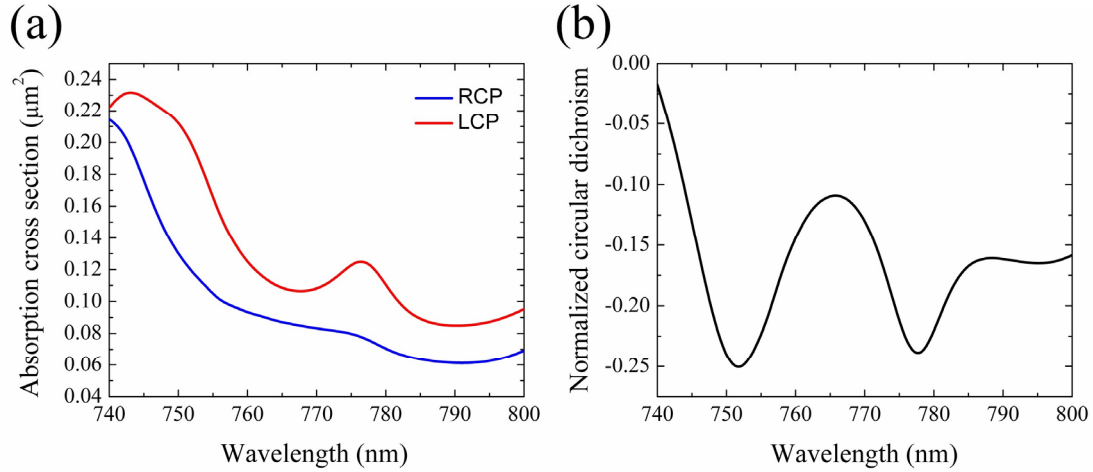


Figure 4-6. Theoretical analysis of the absorption of the nanoflower. (a) Absorption cross-section of the nanoflower. (b) Normalized circular dichroism of the nanoflower.

While optical activity can, in general, originate from both the optical anisotropy and chirality of nanostructures [108, 109], for our nanoflower, the giant optical activity comes from its chirality. The nanoflower can be expressed as a Jones matrix \mathbf{R} in Cartesian coordinates as

$$\mathbf{R} = \begin{pmatrix} r_{xx} & r_{xy} \\ r_{yx} & r_{yy} \end{pmatrix}. \quad (4-8)$$

The x axis and y axis are in the plane of the nanoflower while the z axis is normal to the nanoflower. The matrix can be rewritten in terms of symmetric and antisymmetric components as

$$\mathbf{R} = \begin{pmatrix} r_{xx} & r_{\text{sym}} + r_{\text{asym}} \\ r_{\text{sym}} - r_{\text{asym}} & r_{yy} \end{pmatrix}, \quad (4-9)$$

where $r_{\text{sym}} = \frac{1}{2}(r_{xy} + r_{yx})$ and $r_{\text{asym}} = \frac{1}{2}(r_{xy} - r_{yx})$. The optical anisotropy is determined by the symmetric component r_{sym} while the chirality is determined by the antisymmetric component r_{asym} . The input state \mathbf{I} and the output state \mathbf{O} of light can be

expressed in certain x,y bases as $\mathbf{I} = \begin{pmatrix} i_x \\ i_y \end{pmatrix}$ and $\mathbf{O} = \begin{pmatrix} o_x \\ o_y \end{pmatrix}$. Their relation is given by $\mathbf{O} = \mathbf{RI}$. Additionally, a C3 matrix with respect to the z axis can be expressed as

$$\mathbf{C} = \begin{pmatrix} \cos 2\pi/3 & \sin 2\pi/3 \\ -\sin 2\pi/3 & \cos 2\pi/3 \end{pmatrix}. \quad (4-10)$$

By applying \mathbf{C} to the input and output states of light, we can obtain the equations of $\mathbf{I}' = \mathbf{CI}$ and $\mathbf{O}' = \mathbf{CO}$. As our nanoflower satisfies the C3 symmetry, we can obtain the relation of $\mathbf{O}' = \mathbf{RI}'$. Then, the relation of $\mathbf{CO} = \mathbf{RCI}$ can be deduced from the above equations. Further taking the relation of $\mathbf{O} = \mathbf{RI}$ into consideration, we can obtain $\mathbf{C}^{-1}\mathbf{RC} = \mathbf{R}$. By solving this matrix equation, we obtain $r_{xx} = r_{yy}$ and $r_{xy} = -r_{yx}$. Finally, we obtain the symmetric component $r_{sym} = \frac{1}{2}(r_{xy} + r_{yx}) = 0$ and the antisymmetric component $r_{asym} \neq 0$. Based on the above results, we can conclude the optical activity of our nanoflower comes from the chirality contribution, not the optical anisotropy contribution.

In addition to the above analytic deduction, a numerical simulation is also performed to verify $r_{xy} = -r_{yx}$. Both the real parts and the imaginary parts of r_{xy} and r_{yx} are calculated and shown in Figure 4-7. It is evident from the figure that $r_{xy} = -r_{yx}$, which is consistent with our analytic deduction.

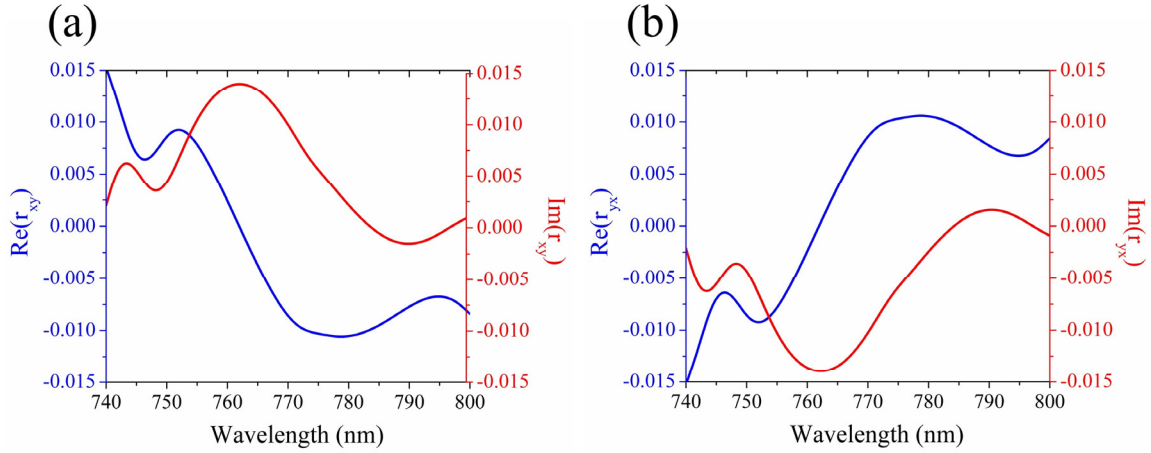


Figure 4-7. Theoretical analysis of the non-diagonal elements the nanoflower's Jones Matrix. (a) Real and imaginary parts of r_{xy} . (b) Real and imaginary parts of r_{yx} .

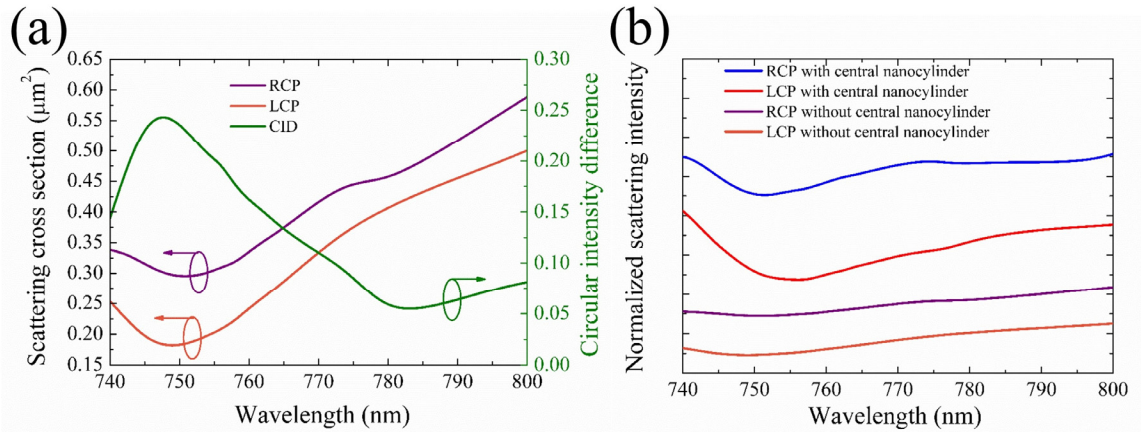


Figure 4-8. Theoretical analysis of the interference between the central nanocylinder and the surrounding nanocylinders. (a) Scattering spectra and CID of the nanoflower without the central nanocylinder. (b) Normalized scattering spectra of the nanoflowers with or without the central nanocylinder.

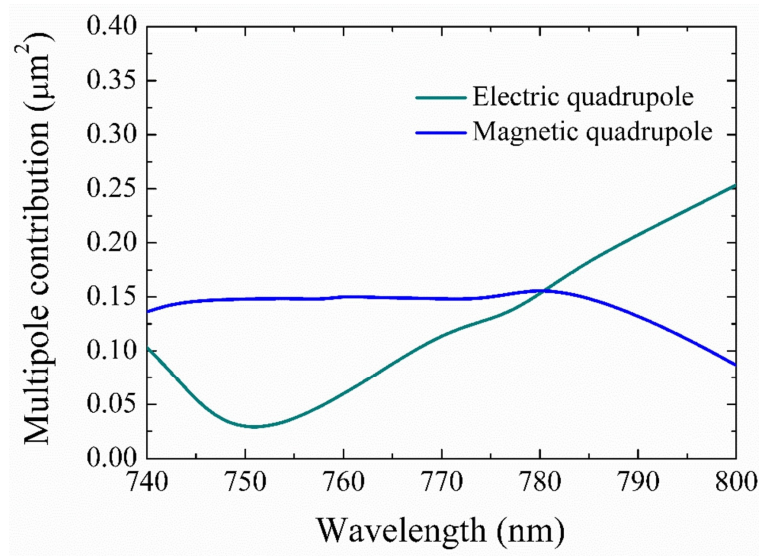


Figure 4-9. Electric and magnetic quadrupole contributions to the scattering cross section of the nanoflower without the central nanocylinder for the incident LCP light.

In order to elucidate the interference between the central nanocylinder and the surrounding nanocylinders, I calculated the scattering spectra of a nanoflower without the central nanocylinder excited by the incident LCP and RCP light as shown in Figure 4-8(a). Based on the scattering spectra of the central-nanocylinder-free nanoflower, the CID was also calculated as shown in the figure. The peak value of the CID in the figure is lower

than that of the nanoflower with the central nanocylinder shown in Figure 4-2(b), indicating the decreased optical activity. In addition, the CID peak also has a blue shift compared with the one in Figure 4-2(b), indicating that the central nanocylinder also affects the optical activity peak wavelength. A comparison of scattering valley depths between the nanoflowers with and without the central nanocylinder based on the theoretical calculation is shown in Figure 4-8(b). The y-axis scales of these four spectra are all normalized to the y-axis scale of the LCP scattering spectrum of the nanoflower with the central nanocylinder (red curve).

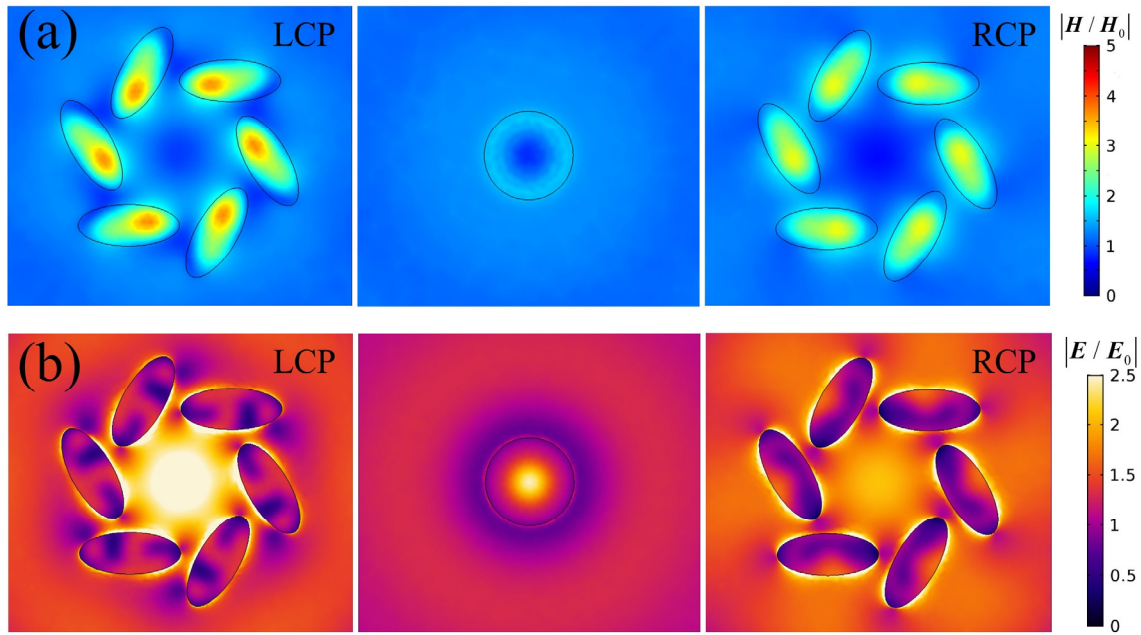


Figure 4-10. Field distributions of the central nanocylinder and the nanoflower without the central nanocylinder. (a) Normalized magnetic near-field strength. (b) Normalized electric near-field strength.

To further verify the destructive interference of the magnetic quadrupole contributions between the central nanocylinder and the surrounding elliptic nanocylinders, I calculated the magnetic quadrupole contribution of the nanoflower without the central nanocylinder for the incident LCP light as shown in Figure 4-9. In contrast to the valley lineshape of the nanoflower with the central nanocylinder in Figure 4-4(a), the magnetic quadrupole contribution lineshape of the nanoflower without the central nanocylinder is a broad peak lineshape. This verifies the generation of Fano destructive interference when the central nanocylinder exists. Moreover, as a comparison of Figure 4-2(c) and Figure 4-2(d), both

the field distributions of the central nanocylinder and the central-nanocylinder-free nanoflower at the wavelength of 757 nm are calculated and shown in Figure 4-10.

4.2.3 Experimental fabrication

In the light of the above theoretical design and analysis, we experimentally fabricated and evaluated the nanoflowers on a silicon-on-insulator wafer. Detailed steps for fabricating the nanoflower is schematically illustrated in Figure 4-11. Firstly, a 130-nm-thick HSQ negative resist film was spin-coated on a silicon-on-insulator chip whose top silicon layer thickness is 340 nm. Then, the nanoflower array pattern was defined on the resist film by electron beam lithography. The chip was developed in a NMD-3 solution for 10 minutes and rinsed in deionized water for 5 minutes. The nanoflower array pattern was transferred to the top silicon layer via inductively coupled plasma by using a mixed gas of CHF₃ and SF₆. Finally, the remaining HSQ resist was removed by using the diluted hydrofluoric acid.

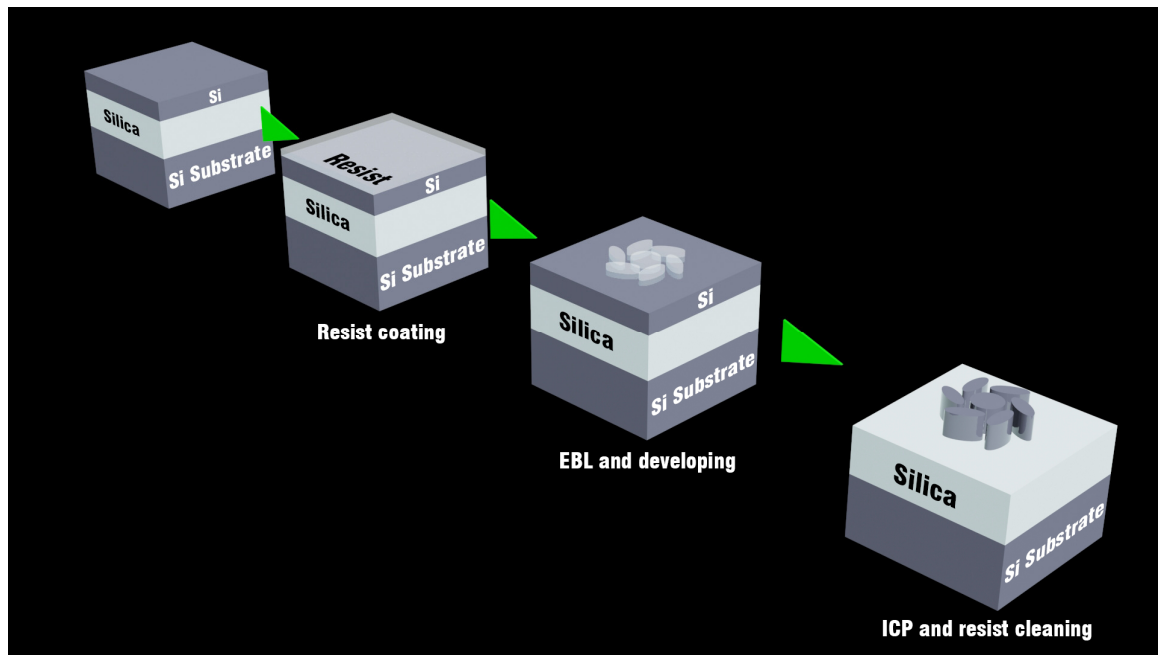


Figure 4-11. Fabrication steps of the nanoflower.

A scanning electron microscope (SEM) image of our fabricated square-lattice nanoflower array with a large period of 5 μm is shown in Figure 4-12(a). This large period avoids the near-field coupling between the adjacent nanoflowers. The SEM image of a single nanoflower which demonstrates high quality for the detailed fabrication is displayed in Figure 4-12(b). It shows that the geometric shape and size of the fabricated nanostructure

fit well with the theoretical design. As an experimental comparison for interference analysis, the nanoflowers without the central nanocylinders were also fabricated. The SEM images are shown in Figure 4-13.

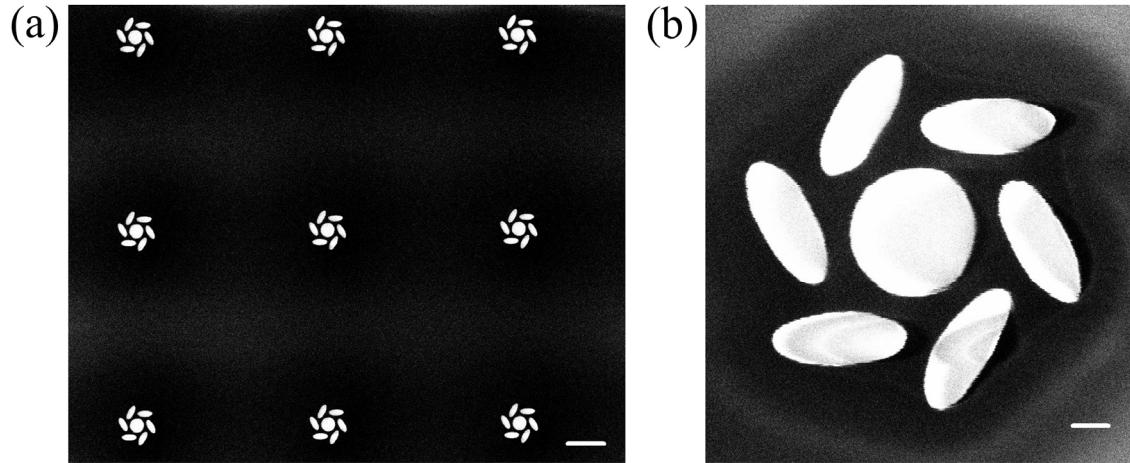


Figure 4-12. Scanning electron microscope images of the fabricated all-dielectric spiral nanoflowers. (a) Array of the nanoflowers. Scale bar = 1 μm . (b) One of the nanoflowers. Scale bar = 100 nm.

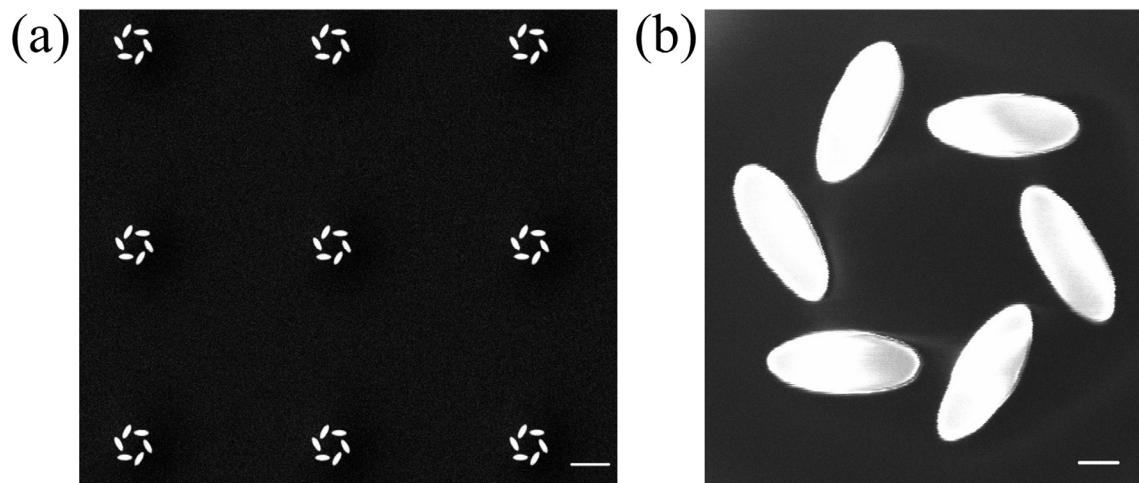


Figure 4-13. Scanning electron microscope images of the fabricated all-dielectric spiral nanoflowers. (a) Array of the nanoflowers. Scale bar = 1 μm . (b) One of the nanoflowers. Scale bar = 100 nm.

4.2.4 Experimental characterization

After fabricating the nanoflowers, I experimentally characterized their optical activity by using a near-normal incidence dark-field microscope. The scattering spectra of the nanoflower were measured by using a dark-field microscope with near-normal incidence

as shown in Figure 4-14. As the dielectric nanoflower has a giant intrinsic chirality, the small extrinsic chirality resulting from the imperfectly normal incidence has little influence on the measurement of optical activity. I used a broadband Tungsten-Halogen light source (Thorlabs SLS201L) to provide the incident light. The circular polarization state of the incident light was controlled by the combination of a linear polarizer (Thorlabs LPVIS050) and an achromatic quarter-wave plate (Thorlabs AQWP05M-980). To maintain the polarization state of the incident light, a low numerical aperture objective lens (Olympus UPLSAPO 10× 0.40 N.A.) was used to focus the incident light on the nanoflower array. The incident light was adjusted to direct it close to the aperture boundary of the objective lens such that the reflected beam was blocked to form the dark field by using a beam blocker. The scattered light was collected by the same objective lens and was then split into two beams by a beam splitter. One beam was used to image and locate the nanoflower array on a CCD camera via a lens. The other beam was coupled to a spectrometer (Thorlabs CCS175) via a lens to measure the scattering spectra of the nanoflower array.

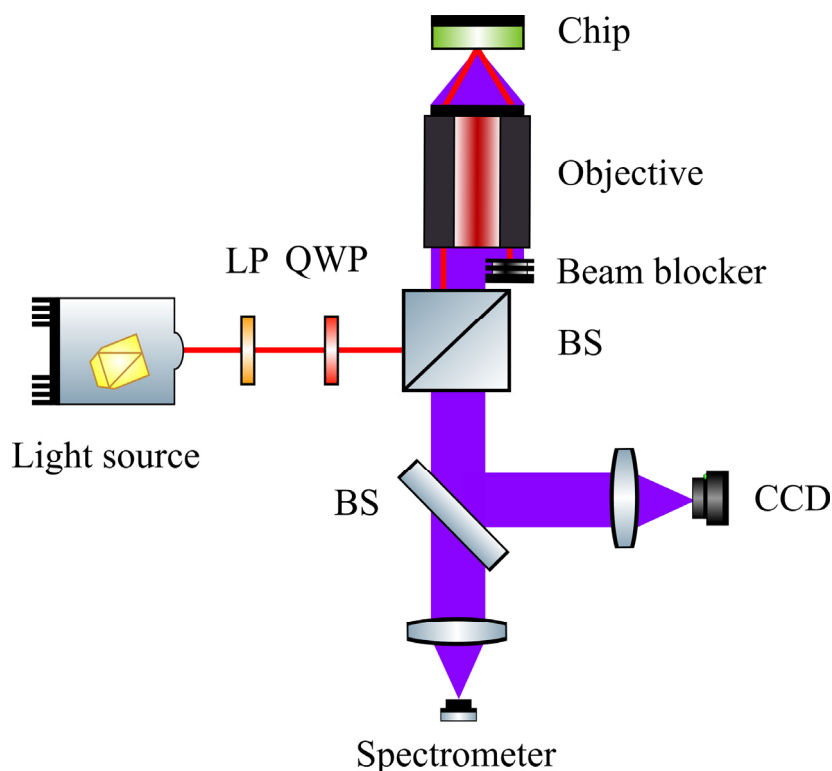


Figure 4-14. Schematic of the optical characterization setup. The red beam is the incident light while the purple beams are the scattered light. LP: linear polarizer. QWP: quarter-wave-plate. BS: beam splitter.

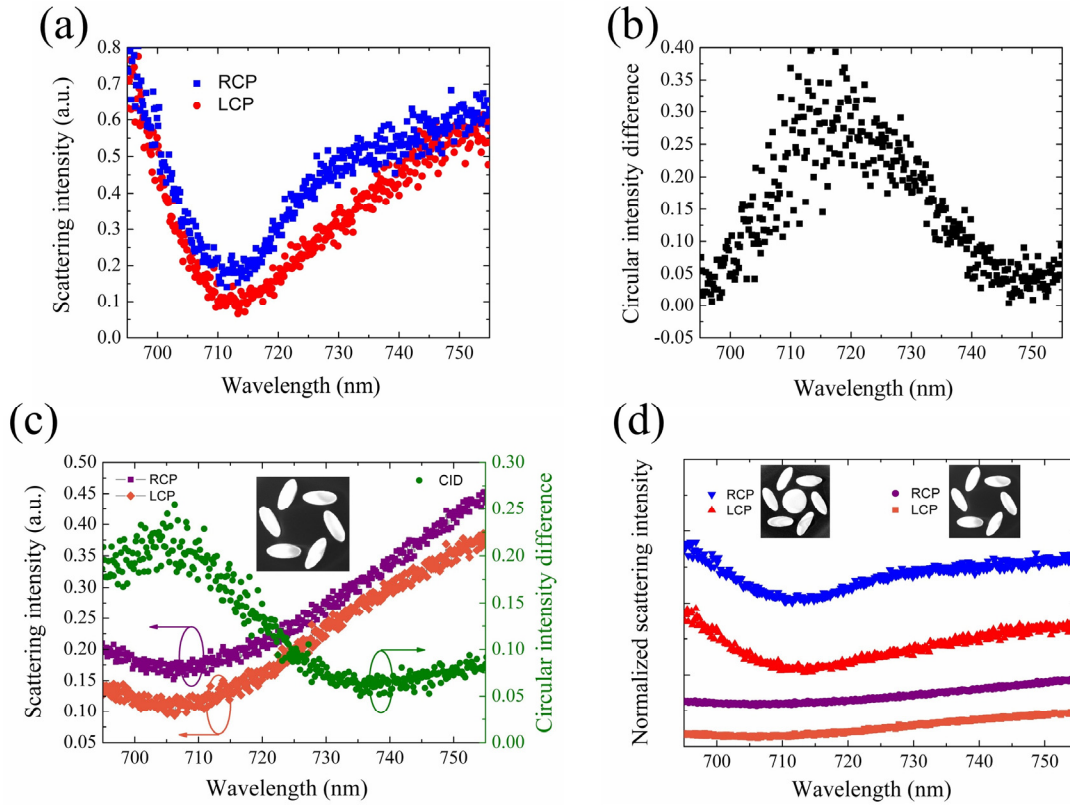


Figure 4-15. Experimental demonstration and validation of giant optical activity. (a) Scattering spectra of the nanoflower excited by LCP and RCP light. (b) CID between the LCP and RCP light. (c) Scattering spectra and CID of the nanoflower without the central nanocylinder. (d) Stack plot of the normalized scattering spectra of the nanoflowers with and without the central nanocylinder.

The scattering spectra of the nanoflowers excited by incident RCP and LCP light were measured and are shown in Figure 4-15(a). A distinct difference was obtained between the two spectra. Compared with the theoretical scattering spectra shown in the Figure 4-2(a), the experimental lineshapes of the scattering spectra fit well with the theoretical ones except for a blueshift of the entire scattering spectra. As the magnetic resonance wavelength in high-refractive-index dielectrics is extremely sensitive to the size of the nanostructure, this 45-nm blueshift corresponds to a size error of ~ 10 nm in the nanofabrication, which is within the limit of our nanofabrication technique. By utilizing the experimental data shown in Figure 4-15(a) and the definition of CID, the CID spectrum was obtained and is shown in Figure 4-15(b). The characteristics of the lineshape fit well with the theoretical lineshape as shown in Figure 4-2(b). The peak CID value of $35 \pm 5\%$ is

consistent with the above theoretical prediction acquired at the wavelength of 713 nm, indicating our experimental realization of giant optical activity.

In order to elucidate the interference between the central nanocylinder and the surrounding nanocylinders, I also characterized the nanoflower without the central nanocylinder and characterized its performance. The scattering spectra of an array of the central-nanocylinder-free nanoflower excited by incident LCP and RCP light as well as its CID spectrum are shown in Figure 4-15(c). The inset shows an SEM image of the fabricated central-nanocylinder-free nanoflower. Its maximum CID is $23\pm3\%$, which is lower than that of the nanoflower with the central nanocylinder as shown in Figure 4-15(b), indicating the decreased optical activity. The CID decrease originates from the decrease of the optical energy localized within the near-field region that reduces the interaction between the incident circularly polarized light and the nanoflower. This is verified by comparing scattering valley depths between the nanoflowers with and without the central nanocylinder as shown in Figure 4-15(d). The y-axis scales of these four spectra in the figure are all normalized with regard to the y-axis scale of the LCP scattering spectrum of the nanoflower with the central nanocylinder (red curve). With the removal of the central nanocylinder, the destructive interference between the central nanocylinder and the surrounding nanocylinders disappears, leading to the decreased scattering valley depths, which is an indicator of the scattering suppression. The decrease of the scattering suppression denotes the decrease of the optical energy localized in the near-field region, which is further verified by comparing the normalized magnetic field strengths in Figure 4-2(c) and Figure 4-10(a).

4.2.5 Summary

In summary, I theoretically predict and experimentally demonstrate a record large circular-intensity difference of $\sim 35\%$ by optimizing the magnetic quadrupole contribution of the nanoflower to scattered light. The giant optical activity is predicted by the numerical simulation and verified by the experimental characterization. By the exploitation of multipole expansion analysis, the physical origin of the giant optical activity that mainly comes from the difference of the magnetic quadrupole contributions to the scattering between the RCP and LCP incident light is identified. By virtue of the low optical

absorption of dielectric materials, the CMOS-compatible silicon spiral nanoflower overcomes the bottleneck of the traditional metallic platforms and is expected to pave the way toward the development of diverse chiroptical devices and applications. One of them is an on-chip chiral Raman sensor with small photothermal heat generation. The nanoflower may also be employed as a unit cell to be assembled into metamaterials for light manipulation, such as wavefront and polarization control.

Although the spiral nanoflower was originally designed for ROA enhancement, we found it is quite challenging to eliminate the optical artifacts induced by the nanoflowers due to their intrinsic chirality. Therefore, based on the above effort and understanding, I transferred to use an achiral structure to enhance ROA, which will be introduced in the next part.

4.3 Nanodisk array for enhanced Raman optical activity

This part is not published because it is scheduled to be published in journals or other publications within five years.

Chapter 5

Demonstration of on-chip carbon photonic devices for Raman spectroscopy

This chapter is not published because it is scheduled to be published in journals or other publications within five years.

Chapter 6

Summary and outlook

In this thesis, I proposed and experimentally demonstrated on-chip group IV photonic devices for vibrational spectroscopy. Specifically, on-chip high-Q germanium photonic devices for infrared spectroscopy, on-chip silicon photonic devices with strong structural resonance for Raman spectroscopy, and an on-chip carbon photonic device with strong chemical enhancement for Raman spectroscopy were developed. A summary of the demonstrated on-chip group IV photonic devices is shown in Table 6-1.

Material	Device	Figure of merit
Germanium	Hexagonal-lattice zero-cell photonic crystal cavity	Q factor: ~ 200
	High-Q photonic crystal nanobeam cavity	Q factor: $\sim 18,000$
	High-Q microring resonator	Q factor: $\sim 54,000$
Silicon	Spiral nanoflower	CID: $\sim 35\%$
	Nanodisk array	Near-field enhancement factor of ROA: $\sim 10^2$
Carbon	PCNA	Enhancement factor of Raman scattering: $\sim 10^6$

Table 6-1. Summary of the demonstrated on-chip group IV photonic devices.

In Chapter 3, I demonstrate three types of on-chip high-Q germanium photonic devices, including a hexagonal-lattice zero-cell photonic crystal cavity, a photonic crystal nanobeam cavity, and a microring resonator, for infrared spectroscopy. The high-Q devices were realized on a germanium suspended-membrane integration platform that I developed in my doctoral work. The theoretical design, experimental fabrication, and experimental characterization of the integration platform as well as the high-Q devices are described and analyzed in detail in this Chapter. With the optimization of device designs and fabrication

recipes, the Q factors of the fabricated devices were increased from ~ 200 to $\sim 18,000$, and finally to $\sim 57,000$. By virtue of high-Q germanium photonic devices, highly-sensitive infrared spectroscopic techniques that cover the fingerprint region can be expected. One of them is an on-chip infrared frequency comb as shown in Figure 6-1, which can be realized through dispersion engineering of the high-Q microring resonator demonstrated in this Chapter.

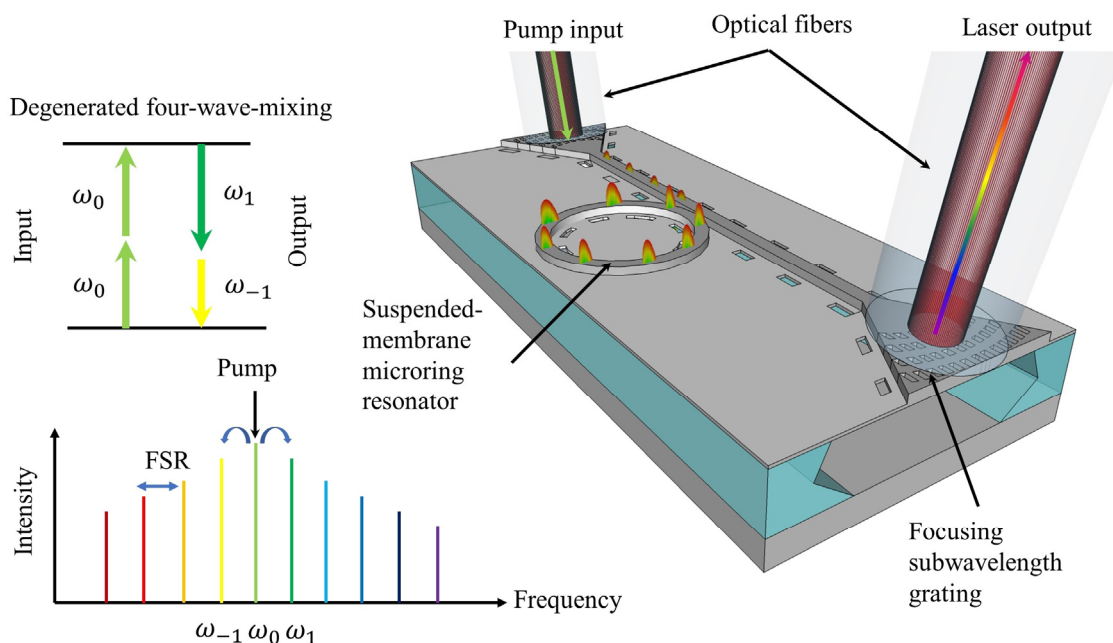


Figure 6-1. On-chip infrared frequency comb based on the high-Q microring resonator.

In Chapter 4, I demonstrate two types of on-chip silicon devices for Raman spectroscopy. The spiral nanoflower is a chiral structure with intrinsically giant optical activity. A largest-to-date circular intensity difference of 35% was experimentally realized by using the nanoflower. The nanodisk array is an achiral structure that achieves superchiral-field-enhanced ROA with negligible artifacts. An enhancement factor of $\sim 10^2$ in the near-field region is experimentally realized for the ROA enhancement. This is enabled by the optically isotropic design and the tailored excited mode of the silicon nanodisk array, which enables precise polarization control and efficient optical-chirality transfer from the far-field to the near-field. By virtue of the demonstrated silicon devices, highly-sensitive Raman optical activity that enables conformational analysis of trace-amount chiral molecules can be expected. One of the potential applications is to realize a

highly sensitive on-chip chiral biosensor as shown in Figure 6-2, by merits of the high enhancement factor and excellent biocompatibility of the silicon nanodisk array demonstrated in this Chapter.

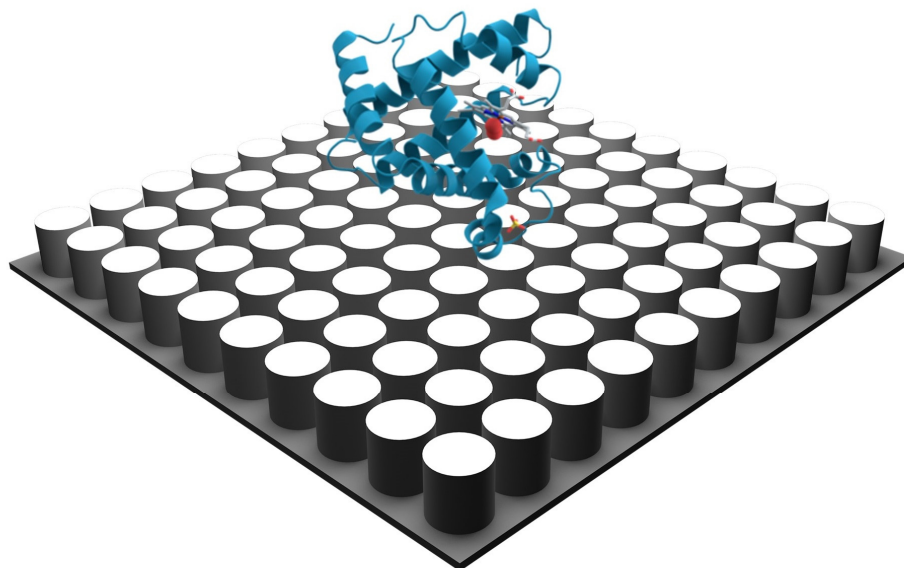


Figure 6-2. Highly sensitive on-chip chiral biosensor.

In Chapter 5, I demonstrate an on-chip carbon device, a PCNA substrate, for Raman spectroscopy. The PCNA substrate is a metal-free, topologically tailored device composed of porous carbon nanowires in a two-dimensional array as a SERS substrate. An extraordinarily high chemical enhancement factor of $\sim 10^6$ was experimentally realized with high reproducibility (i.e., substrate-to-substrate, spot-to-spot, sample-to-sample, and time-to-time) and high biocompatibility. SERS measurements of various molecules such as R6G, β -lactoglobulin, and glucose were conducted. By virtue of the demonstrated carbon devices, highly-reliable SERS can be expected. One of the potential applications is to realize precise quantitative SERS by virtue of its high reproducibility.

By virtue of the CMOS-compatibility, high compactness, and high reliability of these group IV photonic devices with the controllable strong light-matter interaction, low-cost and highly-sensitive vibrational spectroscopy with broad practical applications in

analytical chemistry, pharmaceutical science, environmental safety, and pathology can be expected in the future.

Table of Acronyms

Acronyms	Full Name
AAO	anodized aluminum oxide
ALD	atomic layer deposition
BOX	buried oxide
CCD	charge-coupled device
CID	circular intensity difference
CM	chemical mechanism
CMOS	complementary metal oxide semiconductor
CMP	chemical-mechanical planarization
CNA	carbon nanowire array
DMSO	dimethyl sulfoxide
EBL	electron-beam lithography
EM	electromagnetic mechanism
ER	extinction ratio
HF	finite element method
FSR	free spectral range
FTIR	Fourier transform infrared spectroscopy
GOI	germanium-on-insulator
HF	hydrogen fluoride
HOMO	highest occupied molecular orbital
HSQ	hydrogen silsesquioxane
ICP	Inductively coupled plasma

IR	infrared
LCP	left circularly polarized
LSPR	localized surface plasmon resonance
LUMO	lowest unoccupied molecular orbital
Mf	mass fraction
NMR	nuclear magnetic resonance
PCNA	porous carbon nanowire array
PECVD	plasma enhanced chemical vapor deposition
PML	perfectly matched layer
PNA	polypyrrole nanowire array
PPNA	porous polypyrrole nanowire array
PPy	polypyrrole
Q	quality
RCP	right circularly polarized
RIE	reactive-ion etching
ROA	Raman optical activity
SEM	scanning electron microscope
SERS	surface enhanced Raman scattering
SOI	silicon-on-insulator
SPR	surface plasmon resonance
SSA	specific surface area
TE	transverse electric

Publications

During my Ph.D., I conducted several different projects, including both experimental work and theoretical work. Listed below are my publications in peer-reviewed journals.

Publication related to this thesis

1. T. H. Xiao, Z. Zhao, W. Zhou, M. Takenaka, H. K. Tsang, Z. Cheng, and K. Goda, "Mid-infrared germanium photonic crystal cavity," *Optics Letters* **42**, 2882 (2017)
2. T. H. Xiao, Z. Zhao, W. Zhou, M. Takenaka, H. K. Tsang, Z. Cheng, and K. Goda, "High-Q germanium optical nanocavity," *Photonics Research* **6**, 925 (2018).
3. T. H. Xiao, Z. Zhao, W. Zhou, C. Y. Chang, S. Y. Set, M. Takenaka, H. K. Tsang, Z. Cheng, and K. Goda, "Mid-infrared high-Q germanium microring resonator," *Optics Letters* **43**, 2885 (2018).
4. T. H. Xiao, Z. Cheng, and K. Goda, "Giant optical activity in an all-dielectric spiral nanoflower," *Small* **14**, 1800485 (2018). (Inside Cover)
5. N. Chen, T. H. Xiao, Z. Luo, Y. Kitahama, K. Hiramatsu, T. Itoh, Z. Cheng, and K. Goda, "Porous carbon nanowire array for highly sensitive, biocompatible, reproducible surface-enhanced Raman spectroscopy," submitted to *Nature*, under review. (co-first author)

Publication not related to this thesis

1. T. H. Xiao, Z. Cheng, and K. Goda, " Graphene-on-silicon hybrid plasmonic-photonic integrated circuits," *Nanotechnology* **28**, 245201 (2017).
2. J. Kang, Z. Cheng, W. Zhou, T. H. Xiao, K.-L. Gopalakrisna, M. Takenaka, H. K. Tsang, and K. Goda, "Focusing subwavelength grating coupler for mid-infrared suspended membrane Ge waveguides," *Optics Letters* **42**, 2094 (2017).

Bibliography

1. F. Billes, and I. Mohammed-Ziegler, "Vibrational spectroscopy of phenols and phenolic polymers. Theory, experiment, and applications," *Applied Spectroscopy Reviews* **42**, 369 (2007).
2. R. J. Meier, "Vibrational spectroscopy: A 'vanishing' discipline?," *Chemical Society Reviews* **34**, 743 (2005).
3. B. Stuart, "Infrared spectroscopy," *Kirk-Othmer Encyclopedia of Chemical Technology*, 1 (2000).
4. T. Davies, "The history of near infrared spectroscopic analysis: past, present and future - "from sleeping technique to the morning star of spectroscopy"," *Analisis* **26**, M17 (1998).
5. M. Ferrari, and V. Quaresima, "A brief review on the history of human functional near-infrared spectroscopy (fnirs) development and fields of application," *Neuroimage* **63**, 921 (2012).
6. J. R. Ferraro, "History of fourier transform-infrared spectroscopy," *Spectroscopy* **14**, 28 (1999).
7. J. R. Ferraro, "A history of raman spectroscopy," *Spectroscopy* **11**, 18 (1996).
8. C. V. Raman, and K. S. Krishnan, "A new type of secondary radiation," *Nature* **121**, 501 (1928).
9. B. Chase, "Fourier-transform Raman-spectroscopy," *Analytical Chemistry* **59**, A881 (1987).
10. P. M. Felker, and G. V. Hartland, "Fourier-transform coherent Raman-spectroscopy," *Chemical Physics Letters* **134**, 503 (1987).
11. M. Sieger, and B. Mizaikoff, "Toward on-chip mid-infrared sensors," *Analytical Chemistry* **88**, 5562 (2016).
12. T. L. Koch, and U. Koren, "Semiconductor photonic integrated-circuits," *IEEE Journal of Quantum Electronics* **27**, 641 (1991).
13. R. Nagarajan, C. H. Joyner, R. P. Schneider, J. S. Bostak, T. Butrie, A. G. Dentai, V. G. Dominic, P. W. Evans, M. Kato, M. Kauffman, D. J. H. Lambert, S. K. Mathis, A. Mathur, R. H. Miles, M. L. Mitchell, M. J. Missey, S. Murthy, A. C. Nilsson, F. H. Peters, S. C. Pennypacker, J. L. Pleumeekers, R. A. Salvatore, R. K. Schlenker, R. B. Taylor, H. S. Tsai, M. F. Van Leeuwen, J. Webjorn, M. Ziari, D. Perkins, J. Singh, S. G. Grubb, M. S. Reffle, D. G. Mehuys, F. A. Kish, and D. F. Welch, "Large-scale photonic integrated circuits," *IEEE Journal of Selected Topics in Quantum Electronics* **11**, 50 (2005).
14. T. H. Xiao, Z. Zhao, W. Zhou, M. Takenaka, H. K. Tsang, Z. Cheng, and K. Goda, "High-Q germanium optical nanocavity," *Photonics Research* **6**, 925 (2018).
15. T. H. Xiao, Z. Zhao, W. Zhou, C. Y. Chang, S. Y. Set, M. Takenaka, H. K. Tsang, Z. Cheng, and K. Goda, "Mid-infrared high-Q germanium microring resonator," *Optics Letters* **43**, 2885 (2018).
16. T. H. Xiao, Z. Zhao, W. Zhou, M. Takenaka, H. K. Tsang, Z. Cheng, and K. Goda, "Mid-infrared germanium photonic crystal cavity," *Optics Letters* **42**, 2882 (2017).

17. L. Zhang, A. M. Agarwal, L. C. Kimerling, and J. Michel, "Nonlinear group IV photonics based on silicon and germanium: from near-infrared to mid-infrared," *Nanophotonics* **3**, 247 (2014).
18. K. Yamada, J. Michel, M. Romagnoli, and H. K. Tsang, "Introduction for the group-IV photonics feature," *Photonics Research* **2**, Gp1 (2014).
19. R. Soref, "Group IV photonics enabling 2 μ m communications," *Nature Photonics* **9**, 358 (2015).
20. M. Oehme, R. Koerner, K. Kostecky, S. Bechler, M. Gollhofer, and J. Schulze, "Light sources for group IV photonics," 2016 IEEE Photonics Society Summer Topical Meeting Series (Sum), 3 (2016).
21. G. Z. Mashanovich, M. Nedeljkovic, J. Soler-Penades, Z. Qu, W. Cao, A. Osman, Y. Wu, C. J. Stirling, Y. Qi, Y. Xu-Cheng, L. Reid, C. G. Littlejohns, J. Kang, Z. Zhao, M. Takenaka, T. Li, Z. Zhou, F. Y. Gardes, D. J. Thomson, and G. T. Reed, "Group IV mid-infrared photonics [invited]," *Optical Materials Express* **8**, 2276 (2018).
22. J. S. Levy, A. Gondarenko, M. A. Foster, A. C. Turner-Foster, A. L. Gaeta, and M. Lipson, "CMOS-compatible multiple-wavelength oscillator for on-chip optical interconnects," *Nature Photonics* **4**, 37 (2010).
23. B. U. Sohn, C. Monmeyran, L. C. Kimerling, A. M. Agarwal, and D. T. H. Tan, "Kerr nonlinearity and multi-photon absorption in germanium at mid-infrared wavelengths," *Applied Physics Letters* **111**, 091902 (2017).
24. F. X. Li, S. D. Jackson, C. Grillet, E. Magi, D. Hudson, S. J. Madden, Y. Moghe, C. O'Brien, A. Read, S. G. Duvall, P. Atanackovic, B. J. Eggleton, and D. J. Moss, "Low propagation loss silicon-on-sapphire waveguides for the mid-infrared," *Optics Express* **19**, 15212 (2011).
25. C. J. Smith, R. Shankar, M. Laderer, M. B. Frish, M. Loncar, and M. G. Allen, "Sensing nitrous oxide with QCL-coupled silicon-on-sapphire ring resonators," *Optics Express* **23**, 5491 (2015).
26. J. D. Witmer, J. T. Hill, and A. H. Safavi-Naeini, "Design of nanobeam photonic crystal resonators for a silicon-on-lithium-niobate platform," *Optics Express* **24**, 5876 (2016).
27. J. Chiles, and S. Fathpour, "Mid-infrared integrated waveguide modulators based on silicon-on-lithium-niobate photonics," *Optica* **1**, 350 (2014).
28. K. Luke, Y. Okawachi, M. R. E. Lamont, A. L. Gaeta, and M. Lipson, "Broadband mid-infrared frequency comb generation in a Si_3N_4 microresonator," *Optics Letters* **40**, 4823 (2015).
29. W. Bogaerts, P. De Heyn, T. Van Vaerenbergh, K. De Vos, S. K. Selvaraja, T. Claes, P. Dumon, P. Bienstman, D. Van Thourhout, and R. Baets, "Silicon microring resonators," *Laser & Photonics Reviews* **6**, 47 (2012).
30. A. Vasiliev, A. Malik, M. Muneeb, B. Kuyken, R. Baets, and G. Roelkens, "On-chip mid-infrared photothermal spectroscopy using suspended silicon-on-insulator microring resonators," *ACS Sensors* **1**, 1301 (2016).
31. X. Z. Zhang, T. G. Liu, J. F. Jiang, M. Feng, and K. Liu, "Mid-infrared frequency comb generation in coupled silicon microring resonators," *Optics Communications* **332**, 125 (2014).
32. T. Hansson, D. Modotto, and S. Wabnitz, "Mid-infrared soliton and raman frequency comb generation in silicon microrings," *Optics Letters* **39**, 6747 (2014).

-
33. R. Shankar, I. Bulu, R. Leijssen, and M. Loncar, "Study of thermally-induced optical bistability and the role of surface treatments in si-based mid-infrared photonic crystal cavities," *Optics Express* **19**, 24828 (2011).
 34. A. Majumdar, J. Kim, J. Vuckovic, and F. Wang, "Electrical control of silicon photonic crystal cavity by graphene," *Nano Letters* **13**, 515 (2013).
 35. R. Shankar, R. Leijssen, I. Bulu, and M. Loncar, "Mid-infrared photonic crystal cavities in silicon," *Optics Express* **19**, 5579 (2011).
 36. N. K. Hon, R. Soref, and B. Jalali, "The third-order nonlinear optical coefficients of Si, Ge, and $\text{Si}_{1-x}\text{Ge}_x$ in the midwave and longwave infrared," *Journal of Applied Physics* **110**, 011301 (2011).
 37. A. Malik, S. Dwivedi, L. Van Landschoot, M. Munceb, Y. Shimura, G. Lepage, J. Van Campenhout, W. Vanherle, T. Van Opstal, R. Loo, and G. Roelkens, "Ge-on-Si and Ge-on-SOI thermo-optic phase shifters for the mid-infrared," *Optics Express* **22**, 28479 (2014).
 38. S. Radosavljevic, N. T. Beneitez, A. Katumba, M. Muneeb, M. Vanslembrouck, B. Kuyken, and G. Roelkens, "Mid-infrared vernier racetrack resonator tunable filter implemented on a germanium on SOI waveguide platform [invited]," *Optical Materials Express* **8**, 824 (2018).
 39. W. Li, P. Anantha, S. Y. Bao, K. H. Lee, X. Guo, T. Hu, L. Zhang, H. Wang, R. Soref, and C. S. Tan, "Germanium-on-silicon nitride waveguides for mid-infrared integrated photonics," *Applied Physics Letters* **109**, 241102 (2016).
 40. J. Kang, X. Yu, M. Takenaka, and S. Takagi, "Impact of thermal annealing on Ge-on-insulator substrate fabricated by wafer bonding," *Materials Science in Semiconductor Processing* **42**, 259 (2016).
 41. K. H. Lee, S. Y. Bao, G. Y. Chong, Y. H. Tan, E. A. Fitzgerald, and C. S. Tan, "Fabrication and characterization of germanium-on-insulator through epitaxy, bonding, and layer transfer," *Journal of Applied Physics* **116**, 103506 (2014).
 42. J. Kang, Z. Z. Cheng, W. Zhou, T. H. Xiao, K. L. Gopalakrishna, M. Takenaka, H. K. Tsang, and K. Goda, "Focusing subwavelength grating coupler for mid-infrared suspended membrane germanium waveguides," *Optics Letters* **42**, 2094 (2017).
 43. M. Sinobad, C. Monat, B. Luther-Davies, P. Ma, S. Madden, D. J. Moss, A. Mitchell, D. Allieux, R. Orobtchouk, S. Boutami, J. M. Hartmann, J. M. Fedeli, and C. Grillet, "Mid-infrared octave spanning supercontinuum generation to 8.5 μm in silicon-germanium waveguides," *Optica* **5**, 360 (2018).
 44. V. I. Konov, "Carbon photonics," *Quantum Electronics* **45**, 1043 (2015).
 45. E. Lidorikis, and A. C. Ferrari, "Photonics with multiwall carbon nanotube arrays," *ACS Nano* **3**, 1238 (2009).
 46. P. Avouris, M. Freitag, and V. Perebeinos, "Carbon-nanotube photonics and optoelectronics," *Nature Photonics* **2**, 341 (2008).
 47. G. Agnus, A. Filoramo, S. Lenfant, D. Vuillaume, J. P. Bourgoin, and V. Derycke, "High-speed programming of nanowire-gated carbon-nanotube memory devices," *Small* **6**, 2659 (2010).
 48. C. Xie, B. Nie, L. H. Zeng, F. X. Liang, M. Z. Wang, L. B. Luo, M. Feng, Y. Q. Yu, C. Y. Wu, Y. C. Wu, and S. H. Yu, "Core-shell heterojunction of silicon nanowire arrays and carbon quantum dots for photovoltaic devices and self-driven photodetectors," *ACS Nano* **8**, 4015 (2014).

-
49. F. Bonaccorso, Z. Sun, T. Hasan, and A. C. Ferrari, "Graphene photonics and optoelectronics," *Nature Photonics* **4**, 611 (2010).
 50. Q. L. Bao, and K. P. Loh, "Graphene photonics, plasmonics, and broadband optoelectronic devices," *ACS Nano* **6**, 3677 (2012).
 51. M. Romagnoli, V. Sorianello, M. Midrio, F. H. L. Koppens, C. Huyghebaert, D. Neumaier, P. Galli, W. Templ, A. D'Errico, and A. C. Ferrari, "Graphene-based integrated photonics for next-generation datacom and telecom," *Nature Reviews Materials* **3**, 392 (2018).
 52. N. Zhang, L. M. Tong, and J. Zhang, "Graphene-based enhanced Raman scattering toward analytical applications," *Chemistry of Materials* **28**, 6426 (2016).
 53. T. Itoh, Y. S. Yamamoto, and Y. Ozaki, "Plasmon-enhanced spectroscopy of absorption and spontaneous emissions explained using cavity quantum optics," *Chemical Society Reviews* **46**, 3904 (2017).
 54. D. Meschede, "Photons: An introduction to quantum optics," *Optics, Light, and Lasers: The Practical Approach to Modern Aspects of Photonics and Laser Physics*, 417 (2017).
 55. T. Coudreau, C. Fabre, and S. Reynaud, "An introduction to quantum optics," *Optics in Astrophysics* **198**, 351 (2005).
 56. M. Fox, *Quantum optics: an introduction* OUP, Oxford (2006).
 57. E. C. Le Ru, and P. G. Etchegoin, *Principles of surface-enhanced Raman spectroscopy: and related plasmonic effects* Elsevier, Boston (2009).
 58. M. Osawa, "Dynamic processes in electrochemical reactions studied by surface-enhanced infrared absorption spectroscopy (SEIRAS)," *Bulletin of the Chemical Society of Japan* **70**, 2861 (1997).
 59. G. Sun, and J. B. Khurgin, "Origin of giant difference between fluorescence, resonance, and nonresonance Raman scattering enhancement by surface plasmons," *Physical Review A* **85**, 063410 (2012).
 60. A. I. Kuznetsov, A. E. Miroshnichenko, M. L. Brongersma, Y. S. Kivshar, and B. Luk'yanchuk, "Optically resonant dielectric nanostructures," *Science* **354**, aag2472 (2016).
 61. J.-M. Jin, *The finite element method in electromagnetics* John Wiley & Sons, New Jersey (2015).
 62. C. Vieu, F. Carcenac, A. Pepin, Y. Chen, M. Mejias, A. Lebib, L. Manin-Ferlazzo, L. Couraud, and H. Launois, "Electron beam lithography: resolution limits and applications," *Applied Surface Science* **164**, 111 (2000).
 63. J. Hopwood, "Review of inductively coupled plasmas for plasma processing," *Plasma Sources Science & Technology* **1**, 109 (1992).
 64. T. H. Xiao, Z. Cheng, and K. Goda, "Giant optical activity in an all-dielectric spiral nanoflower," *Small* **14**, 1800485 (2018).
 65. R. Soref, "Mid-infrared photonics in silicon and germanium," *Nature Photonics* **4**, 495 (2010).
 66. M. Nedeljkovic, J. S. Penades, V. Mittal, G. S. Murugan, A. Z. Khokhar, C. Littlejohns, L. G. Carpenter, C. B. E. Gawith, J. S. Wilkinson, and G. Z. Mashanovich, "Germanium-on-silicon waveguides operating at mid-infrared wavelengths up to 8.5 μm ," *Optics Express* **25**, 27431 (2017).

-
67. B. Troia, J. S. Penades, A. Z. Khokhar, M. Nedeljkovic, C. Alonso-Ramos, V. M. N. Passaro, and G. Z. Mashanovich, "Germanium-on-silicon Vernier-effect photonic microcavities for the mid-infrared," *Optics Letters* **41**, 610 (2016).
 68. C. Alonso-Ramos, M. Nedeljkovic, D. Benedikovic, J. S. Penades, C. G. Littlejohns, A. Z. Khokhar, D. Perez-Galacho, L. Vivien, P. Cheben, and G. Z. Mashanovich, "Germanium-on-silicon mid-infrared grating couplers with low-reflectivity inverse taper excitation," *Optics Letters* **41**, 4324 (2016).
 69. J. D. Joannopoulos, P. R. Villeneuve, and S. Fan, "Photonic crystals," *Solid State Communications* **102**, 165 (1997).
 70. S. John, "Strong localization of photons in certain disordered dielectric superlattices," *Physical Review Letters* **58**, 2486 (1987).
 71. K. Sumita, K. Kato, M. Takenaka, and S. Takagi, "Fabrication of thin body InAs-on-insulator structures by Smart Cut method with H⁺ implantation at room temperature," *Japanese Journal of Applied Physics* **58**, SBA03 (2019).
 72. J. M. Ramirez, Q. K. Liu, V. Vakarín, X. Le Roux, J. Frigerio, A. Ballabio, C. Alonso-Ramos, E. T. Simola, L. Vivien, G. Isella, and D. Marris-Morini, "Broadband integrated racetrack ring resonators for long-wave infrared photonics," *Optics Letters* **44**, 407 (2019).
 73. M. Kuroki, S. Kako, S. Ishida, K. Oda, T. Ido, S. Iwamoto, and Y. Arakawa, "Germanium photonic crystal nanobeam cavity with $Q > 1,300$," 2015 Conference on Lasers and Electro-Optics (CLEO) (2015).
 74. B. Jalali, M. Paniccia, and G. Reed, "Silicon photonics," *IEEE Microwave Magazine* **7**, 58 (2006).
 75. R. Soref, "The past, present, and future of silicon photonics," *IEEE Journal of Selected Topics in Quantum Electronics* **12**, 1678 (2006).
 76. M. Caldarola, P. Albella, E. Cortes, M. Rahmani, T. Roschuk, G. Grinblat, R. F. Oulton, A. V. Bragas, and S. A. Maier, "Non-plasmonic nanoantennas for surface enhanced spectroscopies with ultra-low heat conversion," *Nature Communications* **6**, 7915 (2015).
 77. R. M. Hazen, and D. S. Sholl, "Chiral selection on inorganic crystalline surfaces," *Nature Materials* **2**, 367 (2003).
 78. C. J. Kim, A. Sanchez-Castillo, Z. Ziegler, Y. Ogawa, C. Noguez, and J. Park, "Chiral atomically thin films," *Nature Nanotechnology* **11**, 520 (2016).
 79. W. Ma, L. Xu, A. F. de Moura, X. Wu, H. Kuang, C. Xu, and N. A. Kotov, "Chiral inorganic nanostructures," *Chemical Reviews* **117**, 8041 (2017).
 80. H. J. Rhee, Y. G. June, J. S. Lee, K. K. Lee, J. H. Ha, Z. H. Kim, S. J. Jeon, and M. H. Cho, "Femtosecond characterization of vibrational optical activity of chiral molecules," *Nature* **458**, 310 (2009).
 81. T. H. Zhang, M. R. C. Mahdy, Y. M. Liu, J. H. Teng, C. T. Lim, Z. Wang, and C. W. Qiu, "All-optical chirality-sensitive sorting via reversible lateral forces in interference fields," *ACS Nano* **11**, 4292 (2017).
 82. Y. Tang, and A. E. Cohen, "Enhanced enantioselectivity in excitation of chiral molecules by superchiral light," *Science* **332**, 333 (2011).
 83. B. A. McGuire, P. B. Carroll, R. A. Loomis, I. A. Finneran, P. R. Jewell, A. J. Remijan, and G. A. Blake, "Discovery of the interstellar chiral molecule propylene oxide (CH₃CHCH₂O)," *Science* **352**, 1449 (2016).

84. R. E. Morris, and X. H. Bu, "Induction of chiral porous solids containing only achiral building blocks," *Nature Chemistry* **2**, 353 (2010).
85. E. Hendry, T. Carpy, J. Johnston, M. Popland, R. V. Mikhaylovskiy, A. J. Lapthorn, S. M. Kelly, L. D. Barron, N. Gadegaard, and M. Kadodwala, "Ultrasensitive detection and characterization of biomolecules using superchiral fields," *Nature Nanotechnology* **5**, 783 (2010).
86. J. B. Pendry, "A chiral route to negative refraction," *Science* **306**, 1353 (2004).
87. K. Y. Bliokh, F. J. Rodríguez-Fortuño, F. Nori, and A. V. Zayats, "Spin-orbit interactions of light," *Nature Photonics* **9**, 796 (2015).
88. Y. Cui, L. Kang, S. Lan, S. Rodrigues, and W. Cai, "Giant chiral optical response from a twisted-arc metamaterial," *Nano Letters* **14**, 1021 (2014).
89. J. Lv, K. Hou, D. Ding, D. Wang, B. Han, X. Gao, M. Zhao, L. Shi, J. Guo, Y. Zheng, X. Zhang, C. Lu, L. Huang, W. Huang, and Z. Tang, "Gold nanowire chiral ultrathin films with ultrastrong and broadband optical activity," *Angewandte Chemie International Edition* **56**, 5055 (2017).
90. M. Hentschel, M. Schaferling, X. Y. Duan, H. Giessen, and N. Liu, "Chiral plasmonics," *Science Advances* **3**, e1602735 (2017).
91. A. Kuzyk, R. Schreiber, Z. Y. Fan, G. Pardatscher, E. M. Roller, A. Hoge, F. C. Simmel, A. O. Govorov, and T. Liedl, "DNA-based self-assembly of chiral plasmonic nanostructures with tailored optical response," *Nature* **483**, 311 (2012).
92. E. Hendry, R. V. Mikhaylovskiy, L. D. Barron, M. Kadodwala, and T. J. Davis, "Chiral electromagnetic fields generated by arrays of nanoslits," *Nano Letters* **12**, 3640 (2012).
93. S. Zu, Y. Bao, and Z. Fang, "Planar plasmonic chiral nanostructures," *Nanoscale* **8**, 3900 (2016).
94. Y. Hwang, B. Hopkins, D. P. Wang, A. Mitchell, T. J. Davis, J. Lin, and X. C. Yuan, "Optical chirality from dark-field illumination of planar plasmonic nanostructures," *Laser & Photonics Reviews* **11**, 1700216 (2017).
95. B. Hopkins, A. N. Poddubny, A. E. Miroshnichenko, and Y. S. Kivshar, "Circular dichroism induced by Fano resonances in planar chiral oligomers," *Laser & Photonics Reviews* **10**, 137 (2016).
96. E. Prodan, C. Radloff, N. J. Halas, and P. Nordlander, "A hybridization model for the plasmon response of complex nanostructures," *Science* **302**, 419 (2003).
97. A. M. Gilbertson, Y. Francescato, T. Roschuk, V. Shautsova, Y. Chen, T. P. Sidiropoulos, M. Hong, V. Giannini, S. A. Maier, L. F. Cohen, and R. F. Oulton, "Plasmon-induced optical anisotropy in hybrid graphene-metal nanoparticle systems," *Nano Letters* **15**, 3458 (2015).
98. J. K. Gansel, M. Thiel, M. S. Rill, M. Decker, K. Bade, V. Saile, G. von Freymann, S. Linden, and M. Wegener, "Gold helix photonic metamaterial as broadband circular polarizer," *Science* **325**, 1513 (2009).
99. V. K. Valev, N. Smisdom, A. V. Silhanek, B. De Clercq, W. Gillijns, M. Ameloot, V. V. Moshchalkov, and T. Verbiest, "Plasmonic ratchet wheels: switching circular dichroism by arranging chiral nanostructures," *Nano Letters* **9**, 3945 (2009).
100. E. Plum, X. X. Liu, V. A. Fedotov, Y. Chen, D. P. Tsai, and N. I. Zheludev, "Metamaterials: Optical activity without chirality," *Physical Review Letters* **102**, 113902 (2009).

-
101. A. B. Evlyukhin, S. M. Novikov, U. Zywiets, R. L. Eriksen, C. Reinhardt, S. I. Bozhevolnyi, and B. N. Chichkov, "Demonstration of magnetic dipole resonances of dielectric nanospheres in the visible region," *Nano Letters* **12**, 3749 (2012).
 102. T. G. Habteyes, I. Staude, K. E. Chong, J. Dominguez, M. Decker, A. Miroshnichenko, Y. Kivshar, and I. Brener, "Near-field mapping of optical modes on all-dielectric silicon nanodisks," *ACS Photonics* **1**, 794 (2014).
 103. R. M. Bakker, D. Permyakov, Y. F. Yu, D. Markovich, R. Paniagua-Dominguez, L. Gonzaga, A. Samusev, Y. Kivshar, B. Luk'yanchuk, and A. I. Kuznetsov, "Magnetic and electric hotspots with silicon nanodimers," *Nano Letters* **15**, 2137 (2015).
 104. K. E. Chong, B. Hopkins, I. Staude, A. E. Miroshnichenko, J. Dominguez, M. Decker, D. N. Neshev, I. Brener, and Y. S. Kivshar, "Observation of Fano resonances in all-dielectric nanoparticle oligomers," *Small* **10**, 1985 (2014).
 105. Y. Yang, Kravchenko, II, D. P. Briggs, and J. Valentine, "All-dielectric metasurface analogue of electromagnetically induced transparency," *Nature Communications* **5**, 5753 (2014).
 106. A. S. Shorokhov, E. V. Melik-Gaykazyan, D. A. Smirnova, B. Hopkins, K. E. Chong, D. Y. Choi, M. R. Shcherbakov, A. E. Miroshnichenko, D. N. Neshev, A. A. Fedyanin, and Y. S. Kivshar, "Multifold enhancement of third-harmonic generation in dielectric nanoparticles driven by magnetic Fano resonances," *Nano Letters* **16**, 4857 (2016).
 107. D. E. Aspnes, and A. A. Studna, "Dielectric functions and optical-parameters of Si, Ge, GaP, GaAs, GaSb, InP, InAs, and InSb from 1.5 to 6.0 eV," *Physical Review B* **27**, 985 (1983).
 108. G. Armelles, A. Cebollada, H. Y. Feng, A. Garcia-Martin, D. Meneses-Rodriguez, J. Zhao, and H. Giessen, "Interaction effects between magnetic and chiral building blocks: a new route for tunable magneto-chiral plasmonic structures," *ACS Photonics* **2**, 1272 (2015).
 109. G. Armelles, B. Caballero, P. Prieto, F. Garcia, A. Cebollada, M. U. Gonzalez, and A. Garcia-Martin, "Magnetic field modulation of chiroptical effects in magnetoplasmonic structures," *Nanoscale* **6**, 3737 (2014).
 110. L. D. Barron, and A. D. Buckingham, "Rayleigh and Raman scattering from optically active molecules," *Molecular Physics* **20**, 1111 (1971).
 111. G. Wilson, L. Hecht, and L. D. Barron, "Residual structure in unfolded proteins revealed by Raman optical activity," *Biochemistry* **35**, 12518 (1996).
 112. L. D. Barron, "Magnetic vibrational optical-activity in resonance Raman-spectrum of ferrocytochrome-c," *Nature* **257**, 372 (1975).
 113. S. O. Pour, L. Rocks, K. Faulds, D. Graham, V. Parchansky, P. Bour, and E. W. Blanch, "Through-space transfer of chiral information mediated by a plasmonic nanomaterial," *Nature Chemistry* **7**, 591 (2015).
 114. I. H. McColl, E. W. Blanch, L. Hecht, N. R. Kallenbach, and L. D. Barron, "Vibrational raman optical activity characterization of poly(L-proline) II helix in alanine oligopeptides," *Journal of the American Chemical Society* **126**, 5076 (2004).
 115. E. W. Blanch, L. Hecht, C. D. Syme, V. Volpetti, G. P. Lomonossoff, K. Nielsen, and L. D. Barron, "Molecular structures of viruses from Raman optical activity," *Journal of General Virology* **83**, 2593 (2002).
 116. B. Nieto-Ortega, J. Casado, E. W. Blanch, J. T. L. Navarrete, A. R. Quesada, and F. J. Ramirez, "Raman optical activity spectra and conformational elucidation of chiral

- drugs. The case of the antiangiogenic aeroplysinin-1," *Journal of Physical Chemistry A* **115**, 2752 (2011).
117. S. Abdali, and E. W. Blanch, "Surface enhanced Raman optical activity (SEROA)," *Chemical Society Reviews* **37**, 980 (2008).
 118. W. L. Bragg, "The specular reflection of x rays," *Nature* **90**, 410 (1913).
 119. F. Castellani, B. van Rossum, A. Diehl, M. Schubert, K. Rehbein, and H. Oschkinat, "Structure of a protein determined by solid-state magic-angle-spinning NMR spectroscopy," *Nature* **420**, 98 (2002).
 120. F. J. Zhu, N. W. Isaacs, L. Hecht, and L. D. Barron, "Raman optical activity: a tool for protein structure analysis," *Structure* **13**, 1409 (2005).
 121. T. Wu, X. H. Zhang, R. Y. Wang, and X. D. Zhang, "Strongly enhanced Raman optical activity in molecules by magnetic response of nanoparticles," *Journal of Physical Chemistry C* **120**, 14795 (2016).
 122. H. Kneipp, J. Kneipp, and K. Kneipp, "Surface-enhanced Raman optical activity on adenine in silver colloidal solution," *Analytical Chemistry* **78**, 1363 (2006).
 123. S. O. Pour, S. E. J. Bell, and E. W. Blanch, "Use of a hydrogel polymer for reproducible surface enhanced Raman optical activity (SEROA)," *Chemical Communications* **47**, 4754 (2011).
 124. L. D. Barron, "The development of biomolecular raman optical activity spectroscopy," *Biomedical Spectroscopy and Imaging* **4**, 223 (2015).
 125. Z. P. Zhou, J. T. Li, R. B. Su, B. M. Yao, H. L. Fang, K. Z. Li, L. D. Zhou, J. Liu, D. Stellinga, C. P. Reardon, T. F. Krauss, and X. H. Wang, "Efficient silicon metasurfaces for visible light," *ACS Photonics* **4**, 544 (2017).
 126. G. Vuye, S. Fisson, V. N. Van, Y. Wang, J. Rivory, and F. Abeles, "Temperature-dependence of the dielectric function of silicon using in-situ spectroscopic ellipsometry," *Thin Solid Films* **233**, 166 (1993).
 127. A. E. Miroshnichenko, A. B. Evlyukhin, Y. F. Yu, R. M. Bakker, A. Chipouline, A. I. Kuznetsov, B. Luk'yanchuk, B. N. Chichkov, and Y. S. Kivshar, "Nonradiating anapole modes in dielectric nanoparticles," *Nature Communications* **6**, 8069 (2015).
 128. L. A. Nafie, *Vibrational optical activity: Principles and applications* John Wiley & Sons, West Sussex (2011).
 129. S. Yamamoto, and H. Watarai, "Incident circularly polarized Raman optical activity spectrometer based on circularity conversion method," *Journal of Raman Spectroscopy* **41**, 1664 (2010).
 130. W. Hug, "Virtual enantiomers as the solution of optical activity's deterministic offset problem," *Applied Spectroscopy* **57**, 1 (2003).
 131. S. Qiu, G. N. Li, P. Liu, C. H. Wang, Z. C. Feng, and C. Li, "Chirality transition in the epoxidation of (-)-alpha-pinene and successive hydrolysis studied by Raman optical activity and DFT," *Physical Chemistry Chemical Physics* **12**, 3005 (2010).
 132. S. Laing, L. E. Jamieson, K. Faulds, and D. Graham, "Surface-enhanced Raman spectroscopy for in vivo biosensing," *Nature Reviews Chemistry* **1**, 0060 (2017).
 133. J. F. Li, Y. F. Huang, Y. Ding, Z. L. Yang, S. B. Li, X. S. Zhou, F. R. Fan, W. Zhang, Z. Y. Zhou, D. Y. Wu, B. Ren, Z. L. Wang, and Z. Q. Tian, "Shell-isolated nanoparticle-enhanced Raman spectroscopy," *Nature* **464**, 392 (2010).
 134. C. M. Aikens, L. R. Madison, and G. C. Schatz, "The effect of field gradient on SERS," *Nature Photonics* **7**, 508 (2013).

-
135. J. R. Lombardi, and R. L. Birke, "A unified view of surface-enhanced Raman scattering," *Accounts of Chemical Research* **42**, 734 (2009).
136. D. Y. Wu, J. F. Li, B. Ren, and Z. Q. Tian, "Electrochemical surface-enhanced Raman spectroscopy of nanostructures," *Chemical Society Reviews* **37**, 1025 (2008).
137. S. Cong, Y. Y. Yuan, Z. G. Chen, J. Y. Hou, M. Yang, Y. L. Su, Y. Y. Zhang, L. Li, Q. W. Li, F. X. Geng, and Z. G. Zhao, "Noble metal-comparable SERS enhancement from semiconducting metal oxides by making oxygen vacancies," *Nature Communications* **6**, 7800 (2015).
138. Y. S. Yamamoto, and T. Itoh, "Why and how do the shapes of surface-enhanced Raman scattering spectra change? Recent progress from mechanistic studies," *Journal of Raman Spectroscopy* **47**, 78 (2016).
139. X. Shi, K. Ueno, T. Oshikiri, Q. Sun, K. Sasaki, and H. Misawa, "Enhanced water splitting under modal strong coupling conditions," *Nature Nanotechnology* **13**, 953 (2018).
140. A. G. Brolo, "Plasmonics for future biosensors," *Nature Photonics* **6**, 709 (2012).
141. S. M. Feng, M. C. dos Santos, B. R. Carvalho, R. T. Lv, Q. Li, K. Fujisawa, A. L. Elias, Y. Lei, N. Perea-Lopez, M. Endo, M. H. Pan, M. A. Pimenta, and M. Terrones, "Ultrasensitive molecular sensor using n-doped graphene through enhanced Raman scattering," *Science Advances* **2**, e1600322 (2016).
142. S. Y. Ding, J. Yi, J. F. Li, B. Ren, D. Y. Wu, R. Panneerselvam, and Z. Q. Tian, "Nanostructure-based plasmon-enhanced Raman spectroscopy for surface analysis of materials," *Nature Reviews Materials* **1**, 16021 (2016).
143. W. H. Park, and M. Jung, "Out-of-plane directional charge transfer-assisted chemical enhancement in the surface-enhanced Raman spectroscopy of a graphene monolayer," *Journal of Physical Chemistry C* **120**, 24354 (2016).
144. Y. He, S. Su, T. T. Xu, Y. L. Zhong, J. A. Zapien, J. Li, C. H. Fan, and S. T. Lee, "Silicon nanowires-based highly-efficient SERS-active platform for ultrasensitive DNA detection," *Nano Today* **6**, 122 (2011).
145. S. M. Wells, I. A. Merkulov, I. I. Kravchenko, N. V. Lavrik, and M. J. Sepaniak, "Silicon nanopillars for field-enhanced surface spectroscopy," *ACS Nano* **6**, 2948 (2012).
146. P. A. Dmitriev, D. G. Baranov, V. A. Milichko, S. V. Makarov, I. S. Mukhin, A. K. Samusev, A. E. Krasnok, P. A. Belov, and Y. S. Kivshar, "Resonant raman scattering from silicon nanoparticles enhanced by magnetic response," *Nanoscale* **8**, 9721 (2016).
147. X. Ling, L. M. Xie, Y. Fang, H. Xu, H. L. Zhang, J. Kong, M. S. Dresselhaus, J. Zhang, and Z. F. Liu, "Can graphene be used as a substrate for Raman enhancement?," *Nano Letters* **10**, 553 (2010).
148. X. Ling, W. J. Fang, Y. H. Lee, P. T. Araujo, X. Zhang, J. F. Rodriguez-Nieva, Y. X. Lin, J. Zhang, J. Kong, and M. S. Dresselhaus, "Raman enhancement effect on two-dimensional layered materials: graphene, h-BN and MoS₂," *Nano Letters* **14**, 3033 (2014).
149. Z. H. Zheng, S. Cong, W. B. Gong, J. N. Xuan, G. H. Li, W. B. Lu, F. X. Geng, and Z. G. Zhao, "Semiconductor SERS enhancement enabled by oxygen incorporation," *Nature Communications* **8**, 1993 (2017).

-
150. A. Musumeci, D. Gosztola, T. Schiller, N. M. Dimitrijevic, V. Mujica, D. Martin, and T. Rajh, "SERS of semiconducting nanoparticles (TiO₂ hybrid composites)," *Journal of the American Chemical Society* **131**, 6040 (2009).
151. M. J. Limo, A. Sola-Rabada, E. Boix, V. Thota, Z. C. Westcott, V. Puddu, and C. C. Perry, "Interactions between metal oxides and biomolecules: from fundamental understanding to applications," *Chemical Reviews* **118**, 11118 (2018).
152. A. B. Djuricic, Y. H. Leung, A. M. C. Ng, X. Y. Xu, P. K. H. Lee, N. Degger, and R. S. S. Wu, "Toxicity of metal oxide nanoparticles: mechanisms, characterization, and avoiding experimental artefacts," *Small* **11**, 26 (2015).
153. L. Da Via, C. Recchi, E. O. Gonzalez-Yanez, T. E. Davies, and J. A. Lopez-Sanchez, "Visible light selective photocatalytic conversion of glucose by TiO₂," *Applied Catalysis B-Environmental* **202**, 281 (2017).
154. N. Chen, S. H. Chen, C. B. Ouyang, Y. W. Yu, T. F. Liu, Y. J. Li, H. B. Liu, and Y. L. Li, "Electronic logic gates from three-segment nanowires featuring two p-n heterojunctions," *NPG Asia Materials* **5**, e59 (2013).
155. K. E. Shafer-Peltier, C. L. Haynes, M. R. Glucksberg, and R. P. Van Duyne, "Toward a glucose biosensor based on surface-enhanced Raman scattering," *Journal of the American Chemical Society* **125**, 588 (2003).
156. J. Wang, "Electrochemical glucose biosensors," *Chemical Reviews* **108**, 814 (2008).
157. P. Hildebrandt, and M. Stockburger, "Surface-enhanced resonance Raman-spectroscopy of rhodamine-6g adsorbed on colloidal silver," *Journal of Physical Chemistry* **88**, 5935 (1984).
158. J. L. Koenig, and B. G. Frushour, "Raman-scattering of chymotrypsinogen-a, ribonuclease, and ovalbumin in aqueous-solution and solid-state," *Biopolymers* **11**, 2505 (1972).
159. Y. M. Jung, B. Czarnik-Matusewicz, and Y. Ozaki, "Two-dimensional infrared, two-dimensional raman, and two-dimensional infrared and Raman heterospectral correlation studies of secondary structure of beta-lactoglobulin in buffer solutions," *Journal of Physical Chemistry B* **104**, 7812 (2000).
160. M. Mathlouthi, and D. V. Luu, "Laser-Raman spectra of d-glucose and sucrose in aqueous-solution," *Carbohydrate Research* **81**, 203 (1980).
161. T. Shikata, and N. Sugimoto, "Dimeric molecular association of dimethyl sulfoxide in solutions of nonpolar liquids," *Journal of Physical Chemistry A* **116**, 990 (2012).
162. M. I. Gorobets, M. B. Ataev, M. M. Gafurov, and S. A. Kirillov, "Raman study of solvation in solutions of lithium salts in dimethyl sulfoxide, propylene carbonate and dimethyl carbonate," *Journal of Molecular Liquids* **205**, 98 (2015).
163. A. Selvarajan, "Raman spectrum of dimethyl sulfoxide (DMSO) and the influence of solvents," *Proceedings of the Indian Academy of Sciences-Section A* **64**, 44 (1966).